COPPE
UFRJ

**Instituto Alberto Luiz Coimbra de
Pós-Graduação e Pesquisa de Engenharia**

ESTUDOS DE ANISOTROPIA SÍSMICA CAUSADA POR FRATURAS VERTICAIS ATRAVÉS DO USO DE DADOS MULTICOMPONENTE

Eliene Bezerra Simão da Silva

Tese de Doutorado apresentada ao Programa de Pós-graduação em Engenharia Civil, COPPE, da Universidade Federal do Rio de Janeiro, como parte dos requisitos necessários à obtenção do título de Doutor em Engenharia Civil.

Orientadores: Luiz Landau
Robert Ronald Stewart

Rio de Janeiro

Outubro de 2017

ESTUDOS DE ANISOTROPIA SÍSMICA CAUSADA POR FRATURAS VERTICAIS ATRAVÉS DO USO DE DADOS MULTICOMPONENTE

Eliene Bezerra Simão da Silva

TESE SUBMETIDA AO CORPO DOCENTE DO INSTITUTO ALBERTO LUIZ COIMBRA DE PÓS-GRADUAÇÃO E PESQUISA DE ENGENHARIA (COPPE) DA UNIVERSIDADE FEDERAL DO RIO DE JANEIRO COMO PARTE DOS REQUISITOS NECESSÁRIOS PARA A OBTENÇÃO DO GRAU DE DOUTOR EM CIÊNCIAS EM ENGENHARIA CIVIL.

Examinada por:

_____
Prof. José Luis Drummond Alves, D.Sc.

_____
Prof. Robert Ronald Stewart, Ph.D.

_____
Prof. Nikolay Dyaur, Ph.D.

_____
Prof. Marco Antonio Cetale Santos, D.Sc.

_____
Prof. Alvaro Luiz Gayoso de Azeredo Coutinho, D.Sc.

_____
Prof. José Abdalla Helayël Neto, D.Sc.

RIO DE JANEIRO, RJ – BRASIL

OUTUBRO DE 2017

I dedicate this thesis to my parents Manoel Simão and Maria de Lourdes, for the education that they gave me, for their efforts to raise a noble citizen in the diversity of obstacles that were present in our way, for their support to my studies and for their love.

Thanks

The completion of this thesis has been a great challenge for me and would not have come to this stage without the support of a number of people who have encouraged me to keep moving forward. I want to thank my committee for kindly accepting to help to improve this work by evaluating me and for the great advice that I know you will give me.

My gratitude goes to Dr. Robert Stewart for giving me the opportunity to participate in remarkable research at the Allied Geophysical Laboratories. Also for all the support since I am back from Houston. Thank you to the AGLers and their director for showing me a real team work. Thank you to my EVOLVE team at the University of Houston. We have learned many things together. A special thank you to Dr. Nikolay Dyaur, for the time spent in experiments, so many discussions and advice. I have learned a lot from him. Thanks to Dr. Paul Garossino for helping me with FreeUSP to make it to work and for his advice in te computational modeling.

To my advisor at the Federal Universiy of Rio de Janeiro, Luiz Landau, thank you for believing in my capacity and for giving me the oportunity to take the Ph.D. course at a recognized institution as COPPE. Dr. Marcos Gallotti for his advising from the begining of the course, support and discussions. He opened my eyes to the big issues in Geophysics and have encouraged me to overcome road blocks. He had inspired me to strive for the best. My gratitude also includes my ex-bosses in Schlumberger, for their support.

Sometimes we come to know people with who we can really count on and those become our friends. That is why I should thank friends like Dr. Leonardo Koblitz and Dr. Yingcai Zheng. A big thanks to my friends Dr. José Afonso Sanches, who had great contributions in the begining of my Ph.D. Thank you to EAGE with their e-mentoring program and to my mentor, Daniela Donno. You have kindly taught me many things and shown me the way to achieve my goals. Thank you MSc. Liliane Franco, Dr. Alcides Aggio from Petrobrás, Pedro de Melo from Schlumberger and Jane Nobre from UFRJ for listening to me, providing me discussions and many

ESTUDOS DE ANISOTROPIA SÍSMICA CAUSADA POR FRATURAS VERTICAIS ATRAVÉS DO USO DE DADOS MULTICOMPONENTE

Eliene Bezerra Simão da Silva

Outubro/2017

Orientadores: Luiz Landau
                    Robert Ronald Stewart

Programa: Engenharia Civil

A anisotropia causada por fraturas é uma grande fonte de incertezas em projetos de perfuração porque as fraturas podem ser caminhos preferenciais de escoamento ou até mesmo ser barreiras durante a produção. Pode-se contornar esse tipo de problema por meio da investigação sísmica anisotrópica no mapeamento da orientação e densidade das fraturas na subsuperfície, impactando-se a localização e a direção dos poços em campo. O presente estudo desenvolve um programa (*analize*) para esse tipo de análise sísmica anisotrópica multicomponente. Valida-se o programa por meio de investigação anisotrópica em dado simulado numericamente e os principais produtos da análise são os azimutes das fraturas e o grau de anisotropia. Os resultados são qualitativamente e quantitativamente coerentes com o modelo, mostrando o potencial da ferramente para a investigação anisotrópica. Um experimento ultrasônico 4C em modelo físico é realizado simulando o método *Ocean Bottom Nodes* (OBN) para investigar a existência de anisotropia de ondas convertidas PS. Foram medidas as propriedades da rocha carbonática do modelo e estudados os coeficientes de transmissão para as interfaces. A porosidade conectada média para o carbonato do modelo foi estimada por saturação. Ondas P e PS demonstraram bom imageamento da formação escavada no modelo. A onda PS apresentou variação azimutal de Δt, sugering uma possível anisotropia azimutal. Esses indicadores foram investigados subsequentemente pelo *analize* com dado azimutal completo (2C x 2C) e confirmou-se existência de eixos de simetria.

MULTICOMPONENT SEISMIC STUDIES OF ANISOTROPY CAUSED BY VERTICAL FRACTURES

Eliene Bezerra Simão da Silva

October/2017

Advisors: Luiz Landau
           Robert Ronald Stewart

Department: Civil Engineering

Anisotropy caused by fractures is a major cause of uncertainties in projects for borehole perforation, since fractures may become pathway for fluid flow or even create barriers during oil production. This issue can be dealt with via seismic anisotropy investigation to map fracture set orientation and density in subsurface, impacting on borehole placement and direction for the field development. This study aims to develop a software (*analize*) for this type of seismic anisotropy analysis of multicomponent data. *Analize* is validated through anisotropy investigation in modeled synthetics. The main products of its analysis are the fracture azimuths and the degree of anisotropy. Qualitative and quantitative results are coherent with the model, showing that the computational code is a powerful tool for anisotropy investigation. 4C ultrasonic physical modeling seismic surveys are performed to simulate the Ocean Bottom Nodes (OBN) method and to investigate the existence of converted-waves PS anisotropy from the water-bottom. Carbonate rock properties were measured and their reflection and transmission coefficients for the model interfaces were studied. The median connected porosity for the carbonate in the model was estimated by the fluid saturation. P-wave and the converted PS-wave have shown great imaging of the cave formation and PS-wave has presented azimuthal variation of Δt, suggesting possible azimuthal anisotropy. Those indicators were later investigated by *analize* with full-azimuth data (2C x 2C) and confirmed axis of symmetry shown previously.

Contents

List of Figures

List of Tables

Chapter 1

Introduction

1.1 Overview

Pre-salt hydrocarbon reservoir characterization is one of the Brazilian petroleum industry's major challenges nowadays. Most of the last discoveries are placed in fractured rocks or in deep and ultra deep water ocean, increasing the complexity of the exploration. In order to deal with this type of challenge, researchers are striving to achieve the state-of-the-art in tools for acquiring great quality, complete data, and outstanding analysis, such as anisotropy, to reliably characterize this type of reservoir.

Marine conventional narrow-azimuth seismic surveys performed with streamers are not able to record multicomponent data. Only compressional-wave (P-wave) is recorded and a great amount of energy is lost due to the alignment of source and receiver in the survey (GUIMARÃES & SIMPLÍCIO, 2003[7]; GUIMARÃES, 1998[8]). Additionally, streamers face sea surface coverage limitations related to physical obstacles like platforms and other offshore structures. Drawbacks of that nature have motivated a quest for new alternative technologies such as Ocean Bottom Nodes (OBN).

The ocean bottom nodes (OBN) technique is a relatively new technology for acquiring marine seismic surveys (BERG *et al.*, 2010[9]). It consists of the deployment of four-component (4C) sensors which are planted onto the seafloor (OVERKIL & FREDRIK NAES, 2005[10]). Although some economic and logistic setbacks are the main factors that still keep this technology from becoming the mainstream survey choice widespread, the OBN technique features superior capabilities like the true full-azimuth, repeatability, vectorial fidelity, multicomponent data, and flexibility

to work amidst physical obstacles on the top and bottom of the ocean.

The allowance for multicomponent data acquisition, one of OBN's main advantages, enables higher quality analysis in comparison to monomode P-wave data. That is because shear-waves (S-waves) own two to three times more information about fractures than P-waves (LIU & MARTINEZ, 2012[3]). They are helpful in estimating lithology; producing better complex structural imaging; surface fluid description; and anisotropy analysis.

However, the only source of S-waves offshore is the recording of mode converted PS-waves (C-waves). They are used in partnership with P-waves because they respond to different properties. Hence their complementary geological information enables a more complete understanding of reservoir's properties and geometrical arrangement (STEWART *et al*. 2003[11]; GAISER, 1999[12]). Nevertheless, C-wave standard investigations for anisotropy are not fully explored yet in Brazil. The focus on high amplitude waves and the lack of expertise on the matter contribute together to the absence of funding initiatives that could change this picture.

S-waves tend to split into two in azimuthally anisotropic media and these two new waves are polarized perpendicular to each other. Since C-waves are a type of shear-waves, they also travel in pairs from their conversion to S-waves, due to velocity changes with azimuthal direction. This splitting phenomenon might also degrade the quality of shear-wave data and cause mis-ties (Alford, 1986[13]).

Understanding how these new components and their associated acquisition and processing coordinate systems are related to the vector wavefields enables the obtention of attribute information of anisotropy, such as natural polarization directions and degree of anisotropy, by analyzing S-wave splitting (LIU & MARTINEZ, 2012[3]; GAISER, 2002[14]; ALFORD, 1986[13]).

Rotation of horizontal components of shear-wave data is one of the key processing procedures in anisotropy analysis (GAISER, 2002[14]). Through rotation, the effect of anisotropy can be compensated for and the fast and slow shear waves can be separated. In the case of azimuthal anisotropy caused by vertically aligned fractures or cracks, the strike of the fractures or cracks and the time lag between the fast and slow waves can be determined by shear-wave rotation, which can be of great interest to exploration geophysicists (ALFORD, 1986[13]).

Many works have been published using hodogram analysis methods to study S-wave splitting (e.g., SCHULTE & EDELMANN, 1988[15]), but these methods require both very high signal-to-noise ratio and the presence of a single wavelet within the analysis window in order to be effective (WINTERSTEIN & Meadows, 1989[16]).

Consequently they are not enough for a full analysis.

Gaiser (1999)[12] presents applications of the method Vector Coordinate Systems of C-waves obtained by multicomponent 3-D data from the ocean bottom cable (OBC) technique. However, converted-wave anisotropy analysis of the OBN data have been less studied. The in-depth exploration of the subject would certainly help to reliably characterize anisotropy intensity and symmetry axes, which in turn provides confident data to improve drilling wells, even in cases when anisotropy is not caused by fractures in the overburden.

1.2   Motivation

Brazil seats among the fifteen countries with major hydrocarbon reserves in the world. In fact, its later discoveries are mainly in the pre-salt plays. According to the national petroleum agency in the country (Agência Nacional do Petróleo – ANP), Petrobrás discovered 5 to 8 billion barrels in a single oil field in 2007, following that up with even larger discoveries in 2010. *"Ambitions soared–Petrobrás predicted it would double its output by 2020 to nearly 5 mbd[1] Consequently, Brazil will has a new position among the top oil reserves in the world"* (The Fuse, 2017[17])(SEFAZ-RJ NT, 2010[18]).

New flexible local content rules for the pre-salt are under discussion by the government since the country has faced a tough intern and external crisis in the petroleum industry which have almost broken their economy. Besides, according to Folha de São Paulo, existent pre-salt hydrocarbon fields under development in Brazil have shown productivity over the expectations (Folha de São Paulo, 2017[19]). That raises the bids for the incoming Brazilian oil auctions reaching billions of reais (The Fuse, 2017[17]).

To be in the cutting-edge technology and explore this type of reserves, powerful and advanced techniques and expertise are continuously demanded. The existence of the robust OBN technique, which records the multicomponent seismic data on the sea bottom, enables for the search for anisotropy via S-waves from the conversion of P-waves. It requires the development of workflows and algorithms for their analysis together with the P-wave for complete results. However, the study of the anisotropy caused by vertical fractures are still not well explored in Brazil.

Unconventional reservoirs are know by their geological complexity. In the case of carbonate reservoirs, Brazilian pre-salt's type of reservoir, dissolution can generate

---

[1]mbd is a unity that stands for million barrels per day in the oil industry.

unconnected or connected porosity, the last one increasing rock permeability. Among the connected porosities one of the most important is the porosity generated along fractures caused by tectonics or stress following deposition. All the former can be translated into seismic anisotropy.

Although Brazil is leading most pre-salt technologies, it still has not done the important work of generating expertise in the field of anisotropy caused by vertical fractures with C-waves. Such deficit induces an unstable state of affairs related to the contractors' human resources departments, which are obliged to direct heavy amounts of money for international contracts. As a result, the country ends up investing heavily without obtaining technological exchange, which is so vital to the sovereignty of the nation.

1.3   Objectives

The main objective of this research is to model multicomponent seismic surveys to study the seismic response of anisotropic medium where the anisotropy is caused by fractures. The author wants to provide information that can enhance conventional analysis of multicomponent seismic data, mainly the C-waves from the OBN data.

This thesis is an attempt at integrating the subjects of C-waves, the OBN technique and anisotropy, via computational modeling and laboratory measurements. To accomplish with the goals, the author aims to cover the topics below:

- Performing computational modeling of isotropic medium.

- Performing computational modeling of anisotropic medium for comparison and analysis.

- Analysis of anisotropy caused by fractures in the compressional waves.

- Writing an algorithm for analysis of anisotropy caused by fractures in shear waves. The algorithm performs geophone rotation of 2C modeled data in the presence of vertical fractures and analysis of C-wave in the presence of vertical fractures.

- Performing the OBN experiment in scale 1:10,000 and simple analysis to understand the design of this type of survey and how to work with such type of data.

- To model and apply the algorithm to ultrasonic physical modeled full azimuth 2Cx2C data and C-wave data over carbonate rock.

The author wishes her work can contribute in the direction of helping to pave the way for the widening of the use of azimuthal anisotropy analysis in current Brazilian geophysical practice. Alternative tools and algorithms like the ones presented in this work for studying anisotropy present a very attractive approach to geophysical problems.

1.4 Thesis Layout

The first chapter introduces the thesis with an overview, the motivations for the work and its layout. The second chapter presents a brief review of the theory employed as well as the major issues surrounding topics presented in the following chapters; it also presents literature that makes significant contributions to the understanding of this thesis, and points the way on further research on the topic.

The third chapter shows computation of anisotropic coefficients for the modeling of anisotropic layers with vertical fractures, perform modeling of vertically fractured geologic model generated based on real layers Mesaverde Sandstone and Mesaverde Shale with vertical fractures. Thus, for the most part, the author restricts the discussion to anisotropy due to shear waves of any nature.

The fourth chapter shows a water-bottom ultrasonic modeling experiment undertaken by the author at the Allied Geophysical Laboratory (AGL) in the University of Houston. It reports the acquisition, processing of compressional and converted-waves and the analysis of multi-offset seismic data. 4C ultrasonic physical scaled modeling seismic surveys were conducted to simulate the Ocean Bottom Nodes (OBN) method and to study converted waves from the water-bottom.

The fifth chapter presents the algorithm for the geophone rotation of shear-waves, its validation by using the modeled data and some applications with full-azimuth physical modeled data. At last, the sixth chapter presents the main conclusions of this work.

Chapter 2

Literature Review

2.1 Introduction

Brazil's later discoveries are mainly in the pre-salt plays, where fractured rock type in deep and ultra deep waters are in evidence. New flexible local content rules for the pre-salt have attracted new investors and international companies to invest a great amount of money in the country due to perspectives of large profits (FOLHA DE SÃO PAULO, 2017[19]; THE FUSE, 2017[17]; SEFAZ-RJ NT, 2010[18]). In order to correspond to such perspectives, the Brazilian oil industry needs to offer the latest and more advanced resources in terms of Geophysical tools, analysis, and expertise.

Several oil fields are located in deep and ultra deep waters in Brazil. Their great depths and distance from shore add to well costs that represent approximately 50 % of the overall cost of a typical pre-salt development project. Researchers believe that there is room for improvement in the efficiency of exploration (ESTRELLA, 2011)[20].

The worldwide exploration industry has been using the available Geophysical technology to examine the subsurface and reduce the exploration risks (EARTH EXPLORER, 2008[21]). Current efforts have been concentrating on maximizing oil and gas production from existing fields as the task of finding new reservoirs becomes more expensive and difficult. Hence, the multicomponent seismic azimuthal anisotropy[1] analysis and the development of tools and expertise in this area are a good way of overcoming the brick walls for this challenge of seeking for new reservoirs, usually unconventional, and monitoring the fields during production, reducing

---

[1]Anisotropy caused by vertical fractures, which will be better explained further in this chapter.

uncertainties, loss of time in unsuccessful drilling and consequently reducing drilling costs. (SILVA *et al.*, 2016[22]).

Back in the 1960s, 70s, and 80s all the textbooks' discussions concerning to shear waves anisotropy largely revolved around the idea of polar anisotropy[2]. Nevertheless, in the mid-1970s, researchers studying earthquakes began to realize that rocks of the sedimentary crust did not necessarily have the polar symmetry assumed by that theory (THOMSEN, 2002[23]).

Firstly Gupta (1973[24] and 1974[25]), and secondly Crampin and King (1977[26] and 1984[27]) in multiple scientific publications pointed out that unequal horizontal stresses in the crust would have the effect of breaking the polar symmetry, and causing new sorts of seismic effects, one of them called S-wave splitting, or birefringence. Crampin and King realized the implications of this phenomenon for Exploration Geophysics. The S-wave components energy presents discontinuities, as well as mismatch in time between them, since one arrives earlier than the other. Consequently, azimuthal seismic attributes can be obtained, such as symmetry axes and anisotropy degree.

The works of Crampin (1981[28], 1985[29]), Lynn and Thomsen (1986)[30], Willis *et al.* (1986)[31], Martin and Davis (1987)[32], and others convincingly demonstrated that azimuthal anisotropy has a first-order influence on shear and mode-converted PS-waves, which split into the fast and slow modes with orthogonal polarizations (TSVANKIN *et al.*, 2010[33]).

Versfelt (2009)[34] discusses the anisotropy in rocks from the South Atlantic margin rift basin, its asymmetry, maximum principal stress state, and implications for presalt exploration. He uses examples from West and East Africa to describe the geological settings in the African pre-salt, which in turn holds pretty much similar features with Brazil's pre-salt geology (Petter, 2010[35]).

Besides, mapping fractures in the overburden is not just all about petroleum. The location and dating of geological events are strongly dependent on the fracture azimuths. Likewise, the mineral industry benefits from minerals that are found filling open fractures. In addition, hundreds of dikes of tensional fractures cut through the south-eastern coastline of Brazil, and their orientations are used to map relevant geological events (BEASLEY *et al.*, 2010[36]). Those are examples of fields where one could apply the analysis treated in this work.

This chapter presents a brief review of the theory used in this work as well as the

---

[2]Anisotropy caused by vertical axes of symmetry, like in fine horizontal layering. It will be better explained further in this chapter.

major issues surrounding the topics presented, the literature that makes significant contributions to the understanding the subject and points the way on further research on the topic. There are chapters which needed particular theories to be explained in detail. Those will be presented inside its own chapter. The reader is encouraged to follow the references presented in this work for a deeper review.

Though this work has not focused only in carbonate rocks, there is a special section to introduce them. The reasons for this are two: the focus on fractured media and recent discoveries of petroleum in carbonate rocks; and the lower spread knowledge of geophysicists concerning to the formation of this type of rock and how it can become a fractured medium.

Nonetheless, this work will present chapters on shale and sandstone rock computational modeling; and ultrasonic physical water-bottom experiment and full azimuth measurements on a carbonate rock from an outcrop. Besides, other materials than rocks are also used to emulate a vertically fractured medium for P-wave ultrasonic physical model experiments.

2.2   The Ocean Bottom Nodes Technique

Marine conventional narrow-azimuth seismic surveys performed with streamers are not able to record multicomponent data. The three-dimensional (3D) conventional survey acquire several 2D lines over the target at the same time. The vessel carrying the source is responsible for towing the streamers which contain hydrophones in the same line where the source is shot. Therefore, the azimuths source-receiver follow the same direction of the original 2D lines. That means all energy not directly pointed to the receiver line is lost (GUIMARÃES & SIMPLÍCIO, 2003[7]; GUIMARÃES, 1998[8]).

The mentioned loss of energy also means a loss of data causing a deficiency in illumination of complex structural geology and lack of good quality data for further analysis. Besides that, the streamers method provides high quality seismic data when the subsurface complexity is lower, but it has limitations when facing physical obstacles such as petroleum platforms and offshore structures (GUIMARÃES, 1998[8]).

New techniques had then been developed to face those challenges, among them vertical seismic profile (VSP) and ocean bottom sensors (OBS). In the VSP, receivers inside a cable are placed vertically providing the real 3D wavefield, where all azimuths are recorded (GUIMARÃES & SIMPLÍCIO, 2003[7]). On the other hand,

the OBS uses sensors which are placed on the ocean floor by cables, in the case of the ocean bottom cable (OBC) technique, or autonomously planted, in the case of the ocean bottom nodes. The concepts of OBC and OBN constitute the development and evolution of the OBS technique.

Nonetheless, physical obstacles were not the only motivation for the seismic acquisition over the ocean floor. Another great motivation is that the OBS method provides geometries of large azimuth that enable the true 3D without the spacial limitation of the VSP. That is a worthwhile key for the imaging of structures in the pre-salt geological setting (RIGSBY, 1997[37]).

In the OBC survey presented in Figure 2.1 (a), cables are deployed over the ocean floor and a vessel carries the source, moving at directions that provide full-azimuth data (RIGSBY, 1997[37]). However, this technique presents limitations related to working in deep to ultra deep waters and the lack of vectorial fidelity as shown in the scheme presented at Figure 2.1 (b). Moreover, when in deep water (depth > 1,000 m), the cables might break due to their own weight (GUIMARÃES, 1998[8]).

Additionally, there is no confidence that the offline horizontal and vertical components will really be positioned the way the geophysicist expects it to be, since cables might fall at any position and even roll and twist (TEODORO, 2017, personal talk). In Figure 2.1 (c) notice that rather than falling at the planned position (black dashed lines), cables might fall anywhere around (red lines).
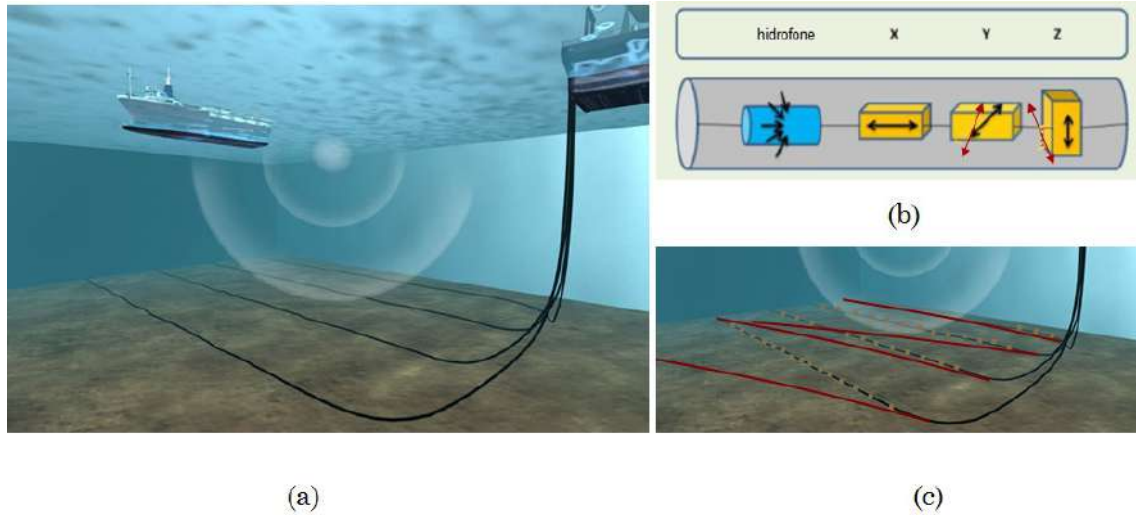
Figure 2.1: Ocean bottom cable technique in (a). Zoom in the cable (b) presents uncertainties in the vectorial positioning due to rolling and bending. Black arrows show the expected positioning of sensors after deployment. Red arrows show what really happens during deployment. Cable might be ill-positioned in (c), red lines (modified from Peak Seismic Solutions[1]).

In Figure 2.1 (b) notice black arrows pointing to the expected direction in the

positioning of sensors. Unfortunately, chances are high that they do not fall as expected end even bend or roll. Then, what really happens is that y and z sensors are not pointing to the expected directions (see red arrows). That causes uncertainties in vectorial fidelity.

In the OBN technique, instead of being towed by a vessel like in conventional marine acquisition or dropped on the ocean floor like in OBC, nodes are positioned accurately. In fact, four-component (4C) sensors are planted on the seabed by a remote operating vehicle (ROV) (MORTON *et al.*, 2003[38]; OVERKIL & FREDRIK NAES, 2005[10]). The sensor is composed of a hydrophone, which is able to detect pressure changes, and a geophone, which is able to detect the particle displacement of P- and two S-waves (OVERKIL & FREDRIK NAES, 2005[10]; BERG *et al.*, 2010[9]).

Therefore, OBN can often provide improved quality compared to the ocean bottom cable type designs, especially for the converted-waves in the horizontal components (BERG *et al.*, 2010[9]) due to their vectorial fidelity, which enables a search for anisotropy. The amount of anisotropy and the main axes of symmetry in the medium are valuable information that can be provided with anisotropy analysis of shear wave data. In the case of the OBN technology, the only shear wave recorded is the converted-wave.

Data quality and completude acquired through an OBN survey can also present enhanced features over conventional marine surveys. Pressure data is also improved because on the ocean bottom the noise is lower. Besides, nodes are especially designed to accomplish with a feature that enables to solve challenges that companies such as Petrobrás are now interested: sparse data analysis. Via this technology, a dense shot mesh is performed, with a diversity of offsets and full azimuth, in the way that sparse sensors are planted. Consequently, less nodes are required in the survey, reducing costs and time of deployment (MORTON *et al.*, 2003[38]).

Figure 2.2 emphasizes the features of full-azimuth survey type. The way they are carefully planted on the floor implies, among several privileges, vectorial fidelity, full-azimuth multicomponent 4C data and sparse sensors with dense shot mesh.

Besides, among the cited advantages of this type of acquisition, flexibility is the keyword for the new requests concerning reservoir monitoring (4D surveys) and complexity on the ocean top and ocean bottom. Though this technique still has its own challenges in ultra deep water (MORTON *et al.*, 2003[38]), the OBN is able to operate under a diversity of types of environments in the subsurface, amid a variety of obstructions, among them, the petroleum platforms and other production
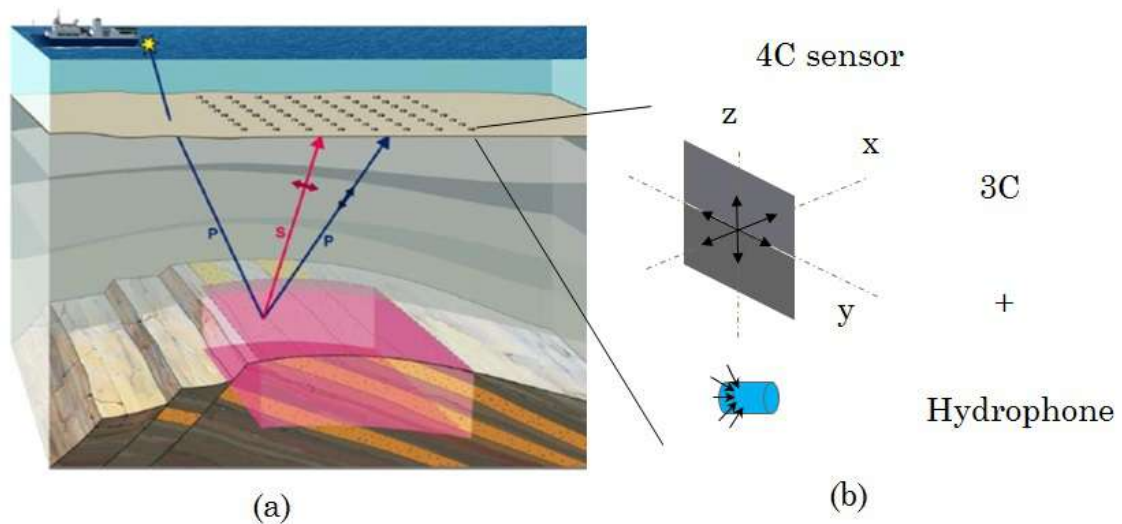
Figure 2.2: Ocean bottom nodes technique in (a). Zoom in a sensor presented in (b) emphasizes its vectorial fidelity, real full azimuth and flexibility to operate under obstructions (modified from Seabed Exploration).

equipment, coral reefs, etc. This type of flexibility allows for the combination of OBN with other survey techniques such as VSP with grid, far and near offset and coil geometries (MORTON *et al.*, 2003[38]); OVERKIL & FREDRIK NAES, 2005[10]).

By benefiting from these OBN qualities one can come to know the pathways of flow and arrangements of storage in the reservoir, which in turn, leads to lowering costs and reducing exploration time, reservoir monitoring and also the search for new prospects. Procedures that explore the completude of the OBN data for analysis of fracture content, in qualitative and quantitative ways, are cutting edge technologies.

2.3   Carbonate Rocks

Carbonate sediments and rocks consist of chemically active calcium and/or calcium/magnesium carbonate. Calcium carbonates are limestones composed mostly of calcite (low magnesium calcite-LMC or high magnesium calcite-HMC), but also of aragonite. Dolostones are composed of dolomite $CaMg(CO_3)_2$.

Unlike terrigenous clastic made up primarily by the disintegration of parent rock and transport to the depositional environment, carbonate sediments are "born" as precipitates or skeletons within the depositional environment (JAMES & KENDALL, 1992[39]). Today the importance of carbonate formation induced by microbial activity is also recognized (RIDING & AWRAMICK, 2000[40]). These attributes of carbonate rock have profound consequences in characterizing the depositional en-

11

vironment and the temporal and spatial style of accumulation depends upon the nature of the sediments themselves.

Carbonate grains are named allochems, and the main types are bioclasts, very important in the Phanerozoic time, encapsulated grains as ooids and oncoids, peloids, intraclasts and/or extraclasts, and aggregates. Precipitated carbonates mainly consist of matrix and are argillaceous to silt-sized. Carbonate can also build large structures like platforms entirely by sediments formed in place. Important buildups of different sizes mainly reefal ones and mud mounds may be part of the carbonate platform.

Carbonates are also highly affected by post-depositional chemical events that can slightly modify the original record until the original texture is completely unrecognizable. This field of study is called Diagenesis. Among diagenetic events the most important are cementation, dissolution, dolomitization, physical and chemical compaction, neomorphism and silicification.

Structures resulting from chemical compaction are stylolites and dissolution seams, which developed during burial at depths higher than 870 m (LINDT, 1993[41]). Stylolites are irregular surfaces resulting from pressure solution of large amounts of carbonate and present a saw tooth appearance. Some studies suggest that stylolites may represent a large amount of rock dissolved and carried away by dissolution. Dissolution seams are fitted features made up of insoluble residues or organic material. All those structures are likely to cause anisotropy.

Features tectonically related such as faults and fractures are important conduits for diagenetic fluids. Dissolution is one of the most important processes for creating open spaces and enhancing porosity and, in most cases, permeability (LUCIA, 2007[42]). These complex porosity systems are mostly related to dissolution and the porosity classified by Choquette and Pray (1970)[2] as *"fabric-selective, non-fabric-selective or fabric-selective or not."*[3] Figure 2.3 shows their classification in details.

Dissolution can generate unconnected or connected porosity, the last one increasing rock permeability. Among the connected porosity, one of the most important is porosity generated along fractures caused by tectonics or stress following deposition (LUCIA, 2007[42]). During burial, bacinal fluids highly saturated with many substances percolate through the rocks and if there is rock-fluid interaction dissolution will generate new porosity and even regional, large-scale brecciation which can be filled by different carbonate cement or other chemical elements in the open spaces

---

[3]As fabric-selective or not is understandable that it is not known if the dissolution is fabric-selective, it might be or not be.

Figure 2.3: Classification of porosity in carbonate sediments according to Choquette and Pray (1970)[2]. Porosity is dark blue.

as oil, or minerals, etc.

If a rock is anisotropic or heterogeneous concerning to a seismic survey, it depends on the wavelength that reaches the rock target. The earth is a high-frequency filter, therefore, at shallow formations the bandwidth is large, there is high-frequency content and low wavelength. On the other hand, at deeper formations, high-frequency is attenuated and most of the bandwidth is made of low frequency and, therefore, long wavelength.

As presented in this section, azimuthal anisotropy in the carbonate might be a result of horizontal stresses in the overburden, cracks or porosity like aligned vugs from diagenesis process (LUCIA, 2007[42]). Though carbonates are considered heterogeneous rocks, features that repeat spatially as fractures, fenestral, caves etc. can cause anisotropy in certain scale for a specific wavelength. According to Vetri et al. (2003)[43], carbonates are frequently fractured.

2.4 Fractures

Fractures are the most abundant visible structural feature in the Earth's crust and they are probably more common than we think. They are evident in most outcrops and core samples and it is likely that most reservoirs contain some natural fractures, particularly in carbonate and unconventional resource (tight gas and shale gas) reservoirs (ENGELDER *et al.*, 2009[44]; ENGELDER, 2011[45]). According to Narr et al. (2006)[46], *"all reservoirs should be considered as fractured unless proven otherwise"*.

Fractures can be open, permeable pathways, or they can be sealed, acting as permeability baffles resulting from the presence of secondary mineralization or other fine-grained materials filling their apertures (e.g., quartz-formed bridges)(LUCIA, 2007[42]). Besides, they can assist in the production of hydrocarbons or prevent their uneconomic extraction (LIN *et al.*, 2015[47]). In addition, long fractures can quickly transport fluid across long distances.

Fluids moving through fractures can react with the rock, corroding fracture walls and thereby enlarging their apertures. Carbonate rocks, particularly limestone, are especially susceptible to solution enlargement due to the solubility of calcite and other carbonate minerals in acid (LUCIA, 2007[42]). This process results in cavern features in carbonate reservoirs. Solution enlargement of fractures is common in carbonate reservoirs and can lead to bit drops and massive lost circulation during drilling (PAŠIĆ *et al.*, 2007[48]).

The main controlling factors of fracture patterns are structures and tectonic stress (NARR *et al.*, 2006[46]; NELSON, 2001[49]). Figure 2.4 shows the distribution of three-dimensional patterns of fractures as a function of vertical stress σ_1, the two horizontal stress fields σ_2 and σ_3 and tensile strength of the rock T: (a) when σ_1 - $\sigma_3 < 4T$ and the two horizontal principal stresses are unequal; (b) when σ_1 - $\sigma_3 >$ 4T and the two horizontal principal stresses are unequal; (c) when σ_1 - $\sigma_3 < 4T$ and when $\sigma_2 = \sigma_3$; and (d) when σ_1 - $\sigma_3 > 4T$ and $\sigma_2 = \sigma_3$.

Fine layering due to deposition produces the so called polar anisotropy, where there is a vertical axis of symmetry (vertical transverse isotropy - VTI). Azimuthal anisotropy is properly represented by the Figure 2.4 (a), where there is a horizontal axis of symmetry (horizontal transverse isotropy - HTI). Those are the simplest anisotropic models that one can think of. Other types of models are either a combination of them, like the orthorhombic, or more complex models (SCHOENBERG & HELBIG, 1997[50]; SCHOENBERG & DOUMA, 1988[51]).

$\sigma_1 > \sigma_2 > \sigma_3$

σ_1

σ_3

σ_1

σ_3

$(\sigma_1 - \sigma_3) < 4T$

(a)

$(\sigma_1 - \sigma_3) > 4T$

(b)

σ_1

σ_1

$\sigma_1 > \sigma_2 = \sigma_3$

σ_1

σ_3

σ_1

σ_3

$(\sigma_1 - \sigma_3) < 4T$

(c)

$(\sigma_1 - \sigma_3) > 4T$

(d)

σ_1

σ_1
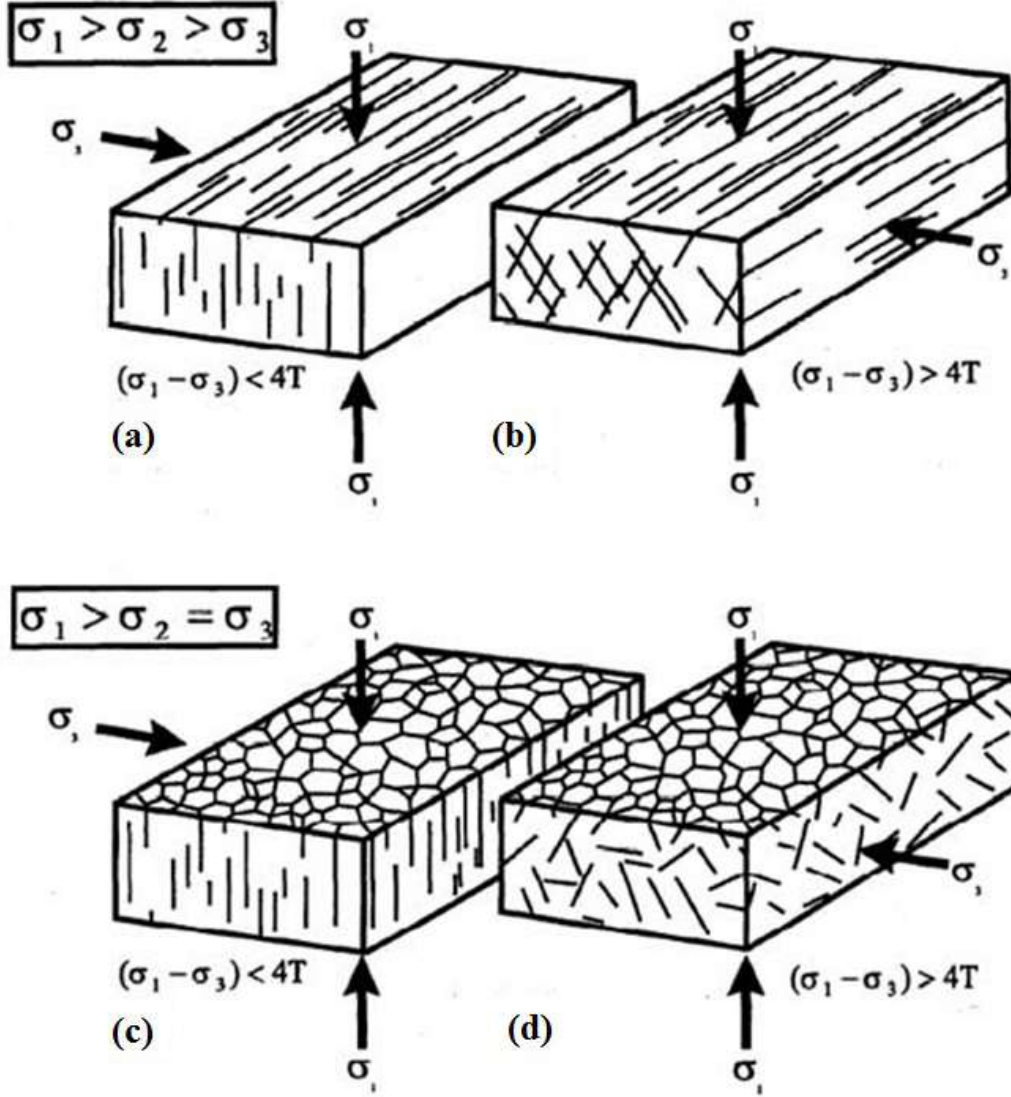
Figure 2.4: Fracture distribution is controlled by stress. Three-dimensional patterns of fractures: (a) when $\sigma_1 - \sigma_3 < 4T$ and the two horizontal principal stresses are unequal; (b) when $\sigma_1 - \sigma_3 > 4T$ and the two horizontal principal stresses are unequal; (c) when $\sigma_1 - \sigma_3 < 4T$ and when $\sigma_2 = \sigma_3$; and (d) when $\sigma_1 - \sigma_3 > 4T$ and $\sigma_2 = \sigma_3$. T is the tensile strength of the rock. (LIU & MARTINEZ[3])

According to Liu and Martinez (2012)[3], stress field present in the rock plays a major role in the development of fractures. Earlier time and stress condition are present in most fractured reservoirs. Hence, the fractures may have been developed under very different stress conditions than the ones present in the reservoirs today. Therefore, it is possible that the reservoir fractures may have almost no relationship with the current stress field.

On the other hand, Zhang and Sanderson (1996)[52] have stated that knowledge of the contemporary stress field can be of practical importance for the management of fractured reservoirs, as permeability anisotropy often correlates with the imposed

stress field.

Fractures have a significant role in the majority of unconventional reservoirs [4], which are: shale gas, coal bed methane, methane hydrates, heavy oil, tight gas and most of the carbonate ones. Stress field also controls the orientation of induced hydraulic fractures such as in tight gas sand and shale reservoir types. Knowing their propagation direction relative to the natural fracture system can lead to improved well-completion planning.

There are cases in which fractures may control the fluid flow and storage in the reservoir. On other occasions they may even create barriers (GAISER & VAN DOK, 2002[14]). The use of technologies that depend on the fracture characterization, such as directional wells or hydraulic fracturing may increase the reservoir production (RATNER & TIEMANN, 2014[54]). To optimize production it is important to know better the reservoir characteristics.

Additionally, the works of Hefferr *et al.* (1995)[55] ' 'New techniques show links between reservoir flow directionality, Earth stress, fault structure, and geometrical changes in mature water floods" and many others (*e. g.* HEFFER & KOUTSABELOULIS (1996)[56]) point to injected-fluid flow preferable path oriented in the direction of the maximum horizontal principal stress in both conventional and unconventional reservoirs. Fractures can also have a strong influence on the porosity and permeability of a reservoir (LIU & MARTINEZ, 2012[3]).

As the amount of information about fractures increases in a reservoir, the occurrence of dry wells decrease, resulting in lower cost to Exploration and Production (E&P). Therefore, fractures can have a profound impact on reservoir management and economic assessment; impacting areas from drilling, well completion, data collection, well placement, enhanced oil recovery (EOR) strategy to estimation of ultimately recoverable reserves; the earlier the presence of fractures can be determined, the better the field development plan can be altered accordingly. Furthermore, the ability to identify fracture clusters and corridors and their prevalent direction within a fractured reservoir can have a significant impact on the profit of the undertaking.

Bates *et al.* (1999)[57] have studied naturally fractured gas reservoirs using seismic methods. In their work they present fractured sandstone and carbonate, and studies with surface seismic producing rose diagrams to show outcrop fracture orientations, maximum horizontal stress directions and compare with data from existent wells. In their conclusions, the natural fractures show a preferential azimuth in field exposure. Furthermore, they show that multicomponent seismic surface data are able to map

---

[4]Non-conventional source rocks are the ones which do not have rock physics behavior that permits the hydrocarbon to be extracted by simple recovery processes (BAHADORI, 2016[53]).

azimuths of sets of fractures.

2.5   Multicomponent Seismic Anisotropy

A great variety of waves propagate in the overburden during the seismic acquisition. Recording all types of waves in a multicomponent survey have provided with exceptional imaging to confidently describe the reservoir (YILMAZ, 2001[58]). Figure 2.5 presents the convention for a multicomponent seismic survey. The x direction is usually defined as the inline direction (pointing from the source to receiver), with the crossline y (transverse to the inline direction) preserving the right handed coordinate system. The z axis is directed upwards with the source motion and receiver components in this acquisition system. When vectorial fidelity is ensured, a consistent anisotropy analysis can be made providing reliable information (LIU & MARTINEZ, 2012[3]).

Figure 2.5: Convention for a multicomponent seismic survey. Isotropic medium (a) and azimuthal anisotropic medium (b).

Data from three-component sources and three-component receivers are called 9C data. For vertically propagating waves in isotropic and VTI media, only the diagonal components in the data matrix should be recorded i.e., xx, yy and zz components, consisting in the P- and S-waves generated directly by the corresponding source. For non-vertically propagating waves in isotropic and VTI media, only the xz and zx components should be recorded, in addition to the diagonal components; i.e., the P to S_V converted waves and S_V to P converted waves, in addition to the P-P, S_V-S_V and S_H-S_H waves (LIU & MARTINEZ, 2012[3]).

In general anisotropic media, the XY and YX components are also non-zero due to shear-wave splitting. They are linked to each other and to the principal directions by tensor analysis. However, it should be noted that misunderstood source motion, heterogeneity, near-surface anisotropy, or inaccurate source-receiver alignment will

result in a departure from this picture and create non-zero off-diagonal components. Symmetry helps as a first step towards assessing these acquisition problems but this is not sufficient for anisotropy analysis (LIU & MARTINEZ, 2012[3]).

Mode-converted PS-wave method is defined by the P energy propagating downward, converting upon reflection to an upcoming S-wave (STEWART *et al.*, 2002[59]; STEWART *et al.*, 1999[60]). Stewart *et al.* (2003)[11] showed in their work that converted-waves are helpful in estimating lithology; producing better complex structural imaging; surface fluid description; reservoir monitoring; and anisotropy analysis. Liu and Martinez (2012)[3] have published a book in multicomponent seismic fracture characterization which shows theory and case studies. According to theirs and many others works, multicomponent seismic data find significant applications, especially in the areas below:

- "Improved seismic imaging in complex areas: gas chimneys, faults, and salt structures, where sometimes P-wave data fail to give clear images.

- Lithology, fluid identification and DHI in general (e.g., the use of joint inversion of PP- and PS-data for VP/VS, which is a lithological indicator). Sometimes, lithology favors one wave mode over others.

- Time-lapse seismic monitoring of CO_2 injections.

- Fracture characterization using shear- and converted-wave splitting."

In this work we focus on the last topic, which is seismic anisotropy mainly caused by vertical fractures. Figure 2.6 presents isotropic and anisotropic wave propagation. In an isotropic medium the polarizations are determined by the survey's geometry, as presented in Figure 2.6 (a)[5]. On the other hand, in an azimuthally anisotropic medium, S-wave propagation may be strongly influenced by fractures and stresses in the subsurface (Figure 2.6 (b)).

The idea is that when an S-wave enters an azimuthal anisotropic medium, it splits into two: a fast S-wave (S_f) and a slow S-wave (S_s), with orthogonal particle motion polarization directions. There will be no S-wave propagation polarized in other direction than those.

As an example, notice in Figure 2.6 (b) the incident P wave converts to an S_V wave at the bottom reflector. However, as it passes through the anisotropic layer above, it becomes polarized according to the anisotropy (stress or fracture) orientation. Approximating the S_V ray paths as near vertical, there will be a fast (S_f) polarization

---

[5]It is usual in Geophysics to consider as S_V the S-wave polarized in the inline direction and S_H the offline when there is.
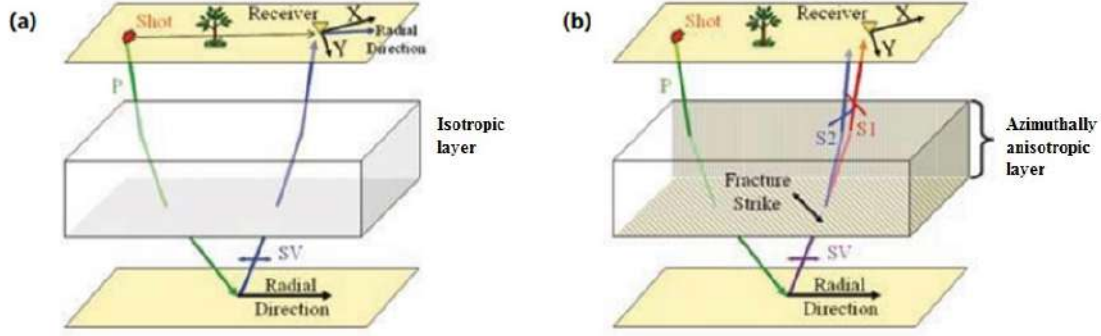
Figure 2.6: Shear wave polarizations. For the isotropic case (a), the polarization is determined by the source-receiver geometry. For the azimuthally anisotropic case (b), it is determined by the fracture orientation (adapted from FIRST BREAK, September (2009)[4]).

which is parallel to the fractures and a slow (S_s) polarization which is orthogonal to them.

When they exit the anisotropic medium, S_f preserves its polarization in the symmetry plane of the anisotropic medium, while the time delay between S_f and S_s is a measure of the anisotropy of the medium. In the case of vertically fractured medium, fast S-wave polarization can be used to infer the fracture orientation and the time delay between S_f and S_s is proportional to the fracture intensity or density (TSVANKIN & GRECHKA, 2011[61]; GAISER *et al.*, 2002[14]; GAISER, 2016[62]). This phenomenon is known as shear-wave splitting or birefringence.

According to Liu and Martinez (2012[3]), shear-waves bring up two to three times more information about fractures than compressional waves (P-waves). Converted PS-waves observed in ocean-bottom sensors data and from land multicomponent data are essentially S-waves and therefore most techniques developed to extract fracture information from pure S-wave data can also be applied to PS-converted or C-wave data.

Consider the synthetic appearance of the shear wave arrivals which result from the splitting in Figure 2.7. From the scheme on the left of Figure 2.7 (a) one can examine the radial component alone. The projection of the split shear waves on the radial component (red or blue) is shown in details (BALE *et al.*, 2009[4]).

The original split shear waves in the natural coordinate system[6] are shown in light gray, and it is their projection on the radial component (the red or blue) that is of interest, because that is what is recorded. Note that their polarity is constant at all azimuths. The red and blue shading now shows the amplitudes of fast and slow

---

[6]Natural coordinate system refers to the axes of symmetry in the medium.
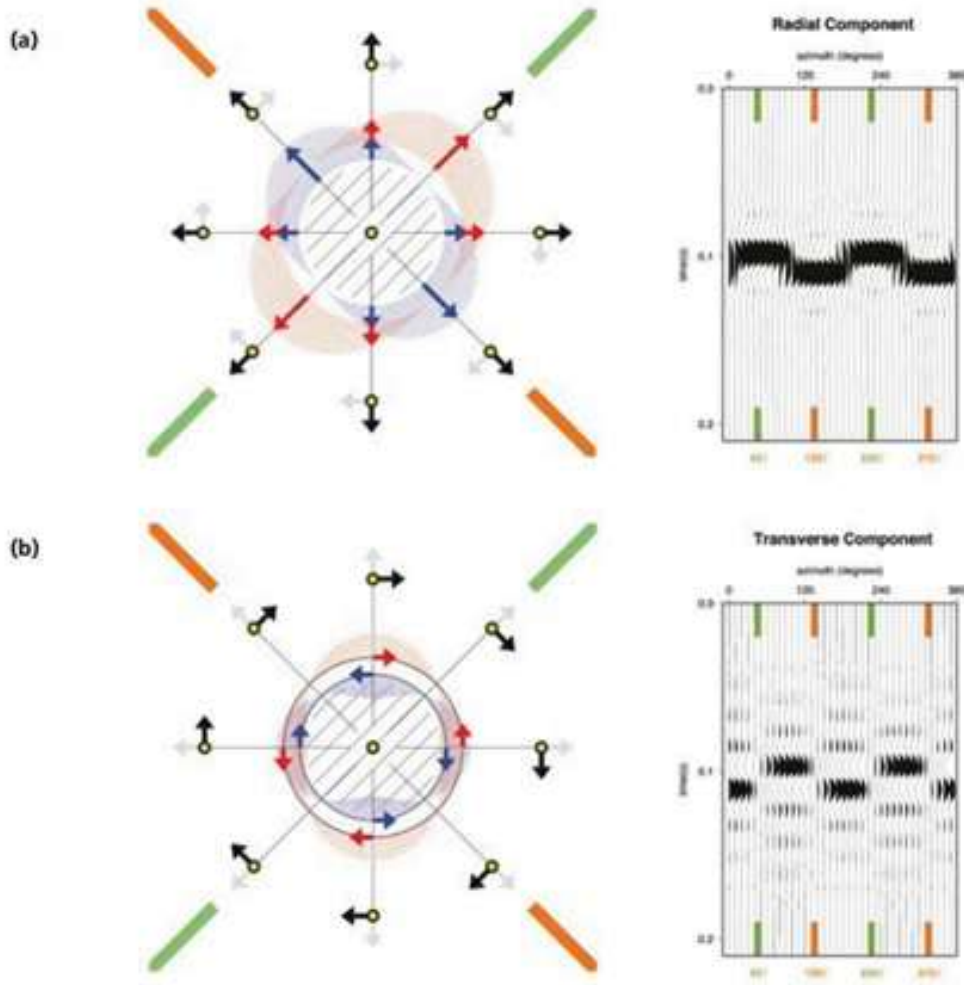
Figure 2.7: Radial (a) and transverse (b) synthetic data illustrating the effect of azimuthal variation. In (a) the signal amplitude varies with azimuth; in (b) the polarity of both the fast and slow shear waves reverses across the symmetry planes (adapted from Bale *et al.* (2009)).

respectively – as measured on the radial. On the right, there is the corresponding synthetic seismogram illustrating the S_f and S_s modes measured for all azimuths on radial as a function of azimuth.

The transverse component has a different character. On the left of Figure 2.7 (b), the amplitude drops to zero on the transverse component for directions in the symmetry planes since there is no splitting. For intermediate azimuths, fast and slow shear waves are opposite in polarity. Across the symmetry planes the polarity of both shear waves reverses.

The synthetic seismogram, on the right, shows visible polarity reversals about the symmetry planes. This characteristic polarity reversal is exploited in several different methods used to determine fracture orientation from shear wave splitting. The characteristic polarity reversal is a key element for recognizing a horizontally

20

transverse isotropic system (90° polarity reversal across fracture strikes).

Many works have been published using hodogram analysis methods to study S-wave splitting (e.g., SCHULTE & EDELMANN, 1988[15]; GUEVARA & STEWART, 2000[63]), but this type of analysis requires both very high signal-to-noise ratio and the presence of a single wavelet within the analysis window in order to be effective (WINTERSTEIN, 1989[16]). Consequently, they cannot stand alone for a complete anisotropy analysis.

Gaiser (1999[12]) presents a extensive contribution in the topic with applications of the method Vector Coordinate Systems of C-waves obtained by multicomponent 3-D data from the ocean bottom cable (OBC) technique. However, converted-wave anisotropy analysis of the water-bottom data have been less studied. The in-depth exploration of the subject would certainly help to reliably characterize anisotropy intensity and symmetry axes, which in turn provides confident data to improve drilling wells, even in cases when anisotropy is not caused by fractures in the overburden.

Inks *et al.* (2014[64]) have performed an excellent analysis of Marcellus, which possess a fractured geology. 3D surveys and azimuthal seismic attributes were used in the analysis which presents rose diagrams. Wide-azimuth S-wave analysis was performed by comparing difference in velocities of S_f and S_s to the isotropic velocity with azimuth.

Even though OBN is still not largely employed due to its higher costs (DUEY, 2007[65]), its versatility and benefits such as good quality data and converted-waves with vectorial fidelity bring up good prospect for the widening of its use in the near future. Furthermore, converted-wave anisotropy analysis of the water-bottom data is less explored, maybe due to their lower amplitudes and specific features. On the other hand, the use of converted-waves can help to reliably characterize anisotropy intensity and symmetry axes.

Difficulties to deal with C-wave arise from their lower amplitude, asymmetric ray path and the lack of original 2C source coordinate system. To accomplish high standard analysis, a reunion of the methods can also be employed to look for anisotropy and to confidently characterize it. This combined approach should prove very useful when analyzing PS-wave attributes such as PS-wave splitting method, radial component amplitudes, transverse over radial component amplitude ratio, PS radial component deviation from the field acquisition source-receiver direction and phase reversal in transverse components.

The geological characteristics of the Pre-Salt raise some difficulties like the quality of seismic data. Those difficulties might be due to the uneven surface of the top

of salt, as well as the internal variations within the salt layers which cause heterogeneous scattering of the seismic energy, and the limited vertical resolution of the reservoir due to the high velocity of the seismic waves. They should be addressed in improvements of nowadays' techniques and technologies for seismic surveys and further illumination studies.

Chapter 3

Seismic Modeling of Vertically Fractured Media

3.1 Summary

Anisotropy caused by fractures is one of the main causes of uncertainties in projects for borehole perforation, since fractures may become pathways for fluid flow or even create barriers during oil production. Knowing in advance if the subsurface has anisotropy helps to reliably characterize anisotropy intensity and symmetry axes, which in turn provides confident data to improve drilling wells, even in cases when anisotropy is not caused by fractures in the overburden. The main goal of this study is to perform computational modeling of azimuthally anisotropic media to understand multicomponent features and anisotropic character in monomode and converted P- to S-waves and S_V- to S_H-waves. In order to do that, seismic surveys are modeled via the Reflectivity method by using a free software. The anisotropic vertically fractured model is built through the creation of an orthorhombic hybrid by imposing vertical fractures on a Vertical Transverse Isotropic (VTI) layer forming a Vertical Fracture Transverse Isotropy (VFTI) layer. Using the method, C_{ij} coefficients are computed by combining some real world lithological parameters from the literature to a specific methodology to model with vertical fractures which is closer to reality. Synthetic data tests showed that the algorithm is successful and robust. S-waves show birefringence for survey not aligned with the main axes of symmetry in the medium. Converted-waves show standard features such as the absence of energy at zero offset, polarity asymmetry around the source, and changes in polarity and phase after P-waves critical angle. S_V- to S_H-wave energy appears in the survey as the angle increases with the direction of the vertical sets of fractures (from 0° to

$90°$). At $0°$ and $90°$ there is no convertion from S_V- to S_H, while conversion happens for angles between $0°$ and $90°$. Both S-wave and PS C-wave proved to be powerful in detecting anisotropy in the rock.

3.2 Introduction

This chapter started to be worked on in February 2015, with great assistance of Mr. Paul Garossino[1] who helped me to install the Free Unix Seismic Processing (FreeUSP) [2] platform in my computer and to put the code to run. The goal was to model seismic surveys over isotropic and anisotropic media with vertical fractures via the reflectivity method to look at features produced by those fractures.

According to him, "the innocent of the request (my request of help to install FreeUSP platform in my notebook) needed to have the Math Advantage library on board for use in compiling ARCO's old acoustic modeling code [D.Corrigan *et al.*, (2006)[66]], released through FreeUSP by Ken Matson back in 2004" (GAROSSINO, personal communication, april 2015). With some work FreeUSP/DDS[3] was installed and the acoustic program could be compiled.

One of the main causes of uncertainties in petroleum projects for borehole perforation is the lack of knowledge concerning to anisotropy caused by fractures. The reason for that is that fractures may become pathways for fluid flow or even create barriers during oil production. Then the direction of perforation is one of the keys of successfully developing the hydrocarbon field (LIU, 2012)[3]. Knowing in advance the overburden anisotropy arrangement helps to reliably characterize the reservoir by computing anisotropy intensity and symmetry axes (THOMSEN, 2002[23]; TS-VANKIN, 1997[67]).

S-wave propagation may be strongly influenced by fractures and stresses in the subsurface. In the presence of azimuthal anisotropy, S-waves split into two, fast-(S_f) and slow-shear (S_s), with orthogonal particle motion polarization directions. In fractured or horizontally stressed rocks the fast S-wave is polarized either along the fracture direction or along the direction of maximum horizontal stress. The slow S-wave is polarized perpendicularly to it. The amount of anisotropy is the arrival time difference between S_f and S_s (THOMSEN, 2001[68]) and (GAISER *et al.*,

---

[1]Mr. Paul Garossino worked with others to build FreeUSP platform years ago.

[2]FreeUSP is a free software-plataform offered in open source by BP America Inc. in the hopes that it may foster education, understanding and collaboration amongst the world wide signal analysis community.

[3]Data Distribution Service.

2002[14]; GAISER & VAN DOK, 1997[69]; GAISER, 2016[62]).

In this chapter, isotropic and anisotropic orthorhombic models are proposed based on Schoenberg's VTIF model to compute stiffness tensor coefficients C_{ij} in Mesaverde and Shale layer from Leon Thomsen (1986)[5]. Models are performed via computational code by using the reflectivity method which is introduced as well as some modifications made by Mr. Garossino. Then, the methodology to compute C_{ij} is shown. We show some features of nine-component (9C) multicomponent seismic response for pure mode P-waves, S-waves and converted P-to S-waves and S_v- to S_h-waves for isotropic and anisotropic modeled media.

3.3   Methodology

This section presents the three most important topics on the methodology to perform the modeling. Firstly, equations that govern weak anisotropy are presented (THOMSEN, 1986[5]; TSVANKIN 1997[67]) and they are used with Mah and Schmitt (2016)[6] and Schoenberg and Helbig (1997)[50] to compute elastic constants for the modeling. Secondly, the reflectivity method is quickly introduced. For details in the reflectivity method the reader is referred to the complete work of Müller (1985)[70] or to Kennett's (1975)[71] work. Then, the computational code is described with its functionalities and main features (CORRIGAN *et al.*, 2006[66]; ALISON *et al.*, 2015[72]).

3.3.1   Elastic Constants for Weak Anisotropy

In most applications of elasticity theory to problems in petroleum geophysics, the elastic medium is assumed to be isotropic. On the other hand, most crustal rocks are found experimentally to be anisotropic. Besides, it is known that if a layered sequence of different media (isotropic or not) is crossed by an elastic wave of wavelength much longer than the typical layer thickness (i.e., the usual seismic exploration), the wave propagates as though it were in a homogeneous, but anisotropic, medium (BACKUS, 1962[73]).

Hence, there is some inconsistency between practice and reality. Most elastic media should then be considered weakly anisotropic. Equations governing weak anisotropy are simpler and more intuitive than those governing strong anisotropy (THOMSEN, 1986[5]). These equations indicate that a certain anisotropic parameter (denoted γ) controls most anisotropic phenomena of importance in exploration geophysics, some

of which are not easily neglectable even when the anisotropy is weak.

The critical parameter γ is a complex combination of elastic parameters. It is totally independent of horizontal velocity and may be either positive or negative in natural contexts. In this work we use some of the equations found in Thomsen (1986)[5] for weak anisotropy. Some of the conclusions that he stated in his work are rewritten below:

1. The most common measure of anisotropy (contrasting vertical and horizontal velocities) is not very relevant to problems of near-vertical P-wave propagation.

2. The most critical measure of anisotropy (denoted γ) does not involve the horizontal velocity at all in its definition and is often undetermined by experimental programs intended to measure anisotropy of rock samples.

3. A common approximation used to simplify the anisotropic wave-velocity equations (elliptical anisotropy) is usually inappropriate and misleading for P and S_V-waves.

4. Use of Poisson's ratio, as determined from vertical P and S velocities, to estimate horizontal stress usually leads to significant error.(THOMSEN, 1986[5], p.1954).

These conclusions apply independently of the physical cause of the anisotropy, since anisotropy in sedimentary rock sequences may be caused by preferred orientation of anisotropic mineral grains (such as in a massive shale formation), preferred orientation of the shapes of isotropic minerals (such as flat-lying platelets), preferred orientation of cracks and fractures (such as parallel cracks, or vertical cracks with no preferred azimuth), or thin bedding of isotropic or anisotropic layers. The conclusions stated here may be applied to rocks with any or all of these physical attributes, with the sole restriction that the resulting anisotropy is weak.

An excellent review of elastic anisotropy is presented by Thomsen (1986)[5]. There he mentions:

A linearly elastic material is defined as one in which each component of stress σ_{ij} is linearly dependent upon every component of strain ϵ_{lk} (NYE, 1957). Since each directional index may assume values of 1, 2, 3 (representing directions x, y, z), there are nine such relations, each involving one component of stress and nine components of strain. These nine equations may be written compactly as

$$\sigma_{ij} = \sum_{k=1}^{3} \sum_{l=1}^{3} C_{ijkl} \epsilon_{kl}, i, j = 1, 2, 3, \qquad (3.1)$$

where the 3 x 3 x 3 x 3 elastic modulus tensor C_{ijkl} completely characterizes

26

the elasticity of the medium. Because of the symmetry of strain ($\epsilon_{kl} = \epsilon_{lk}$), only six of the terms on the right side of each set of equations (1) are independent. The same happens for stress ($\sigma_{ij} = \sigma_{ji}$), only six of these equations are independent. Hence, without loss of generality, the elasticity may be represented more compactly with change of indices:

$$
\begin{aligned}
\text{ij} &\rightarrow \alpha \text{ or kl } \rightarrow \beta : \\
11 &\rightarrow 1 \\
22 &\rightarrow 2 \\
33 &\rightarrow 3 \\
32 = 23 &\rightarrow 4 \\
31 = 13 &\rightarrow 5 \\
12 = 21 &\rightarrow 6
\end{aligned}
\tag{3.2}
$$

so that the 3 x 3 x 3 x 3 tensor C_{ijkl} may be represented by the 6 x 6 matrix Cα β. Each symmetry class has its own pattern of nonzero, independent components Cα β. For example, for isotropic media the matrix assumes the simple form as in Equation 3.3:

$$
C_{ij} = \begin{bmatrix}
C_{33} & (C_{33} - 2C_{44}) & & & & \\
& C_{33} & (C_{33} - 2C_{44}) & & & \\
& & C_{33} & & & \\
& & & C_{44} & & \\
& & & & C_{44} & \\
& & & & & C_{44}
\end{bmatrix} \quad \text{isotropy.}
\tag{3.3}
$$

Only nonzero components in the upper triangle are shown; the lower triangle is symmetrical. These components are related to the *Lame* parameters λ and μ and to the bulk modulus k by

$$
C_{33} = \lambda + 2\mu = K + \frac{4}{3}\mu; \text{ and } C_{44} = \mu
\tag{3.4}
$$

The simplest anisotropic case of broad geophysical applicability has one distinct direction (usually, but not always, vertical), while the other two directions are equivalent to each other. This case is called transverse isotropy, or hexagonal symmetry. The elastic modulus matrix has five independent components among twelve nonzero components, giving the elastic modulus matrix the form

$$
C_{ij} =
\begin{bmatrix}
C_{11} & (C_{11} - 2C_{66}) & & & & \\
& C_{11} & C_{13} & & & \\
& & C_{33} & & & \\
& & & C_{44} & & \\
& & & & C_{44} & \\
& & & & & C_{66}
\end{bmatrix}
\quad \text{transverse isotropy.}
$$

$$(3.5)$$

where the three-direction (z) is taken as the unique axis. (THOMSEN, 1986[5] p.1954-1955)

These expressions for the elastic modulus matrices associated with Isotropic and Transversely Isotropic layers are useful for this methodology as they define the C_{ij} elastic constants required as input to the code for Isotropic and VTI layering. The symmetry of interest has vertical fractures, technically, the symmetry is composed by HTI layers or it is Orthorhombic (SCHOENBERG & HELBIG, 1997)[50] which allows for the type of anisotropy with vertical fractures, without loss of VTI anisotropy.

According to Thomsen (1986)[5] the correlation between phase velocity and elastic moduli for P, S_H and S_V waves is as in Equations 3.6:

$$
\rho V_P^2(\theta) = \frac{1}{2} \left[C_{33} + C_{44} + (C_{11} - C_{33}) \sin^2(\theta) + D(\theta) \right],
$$
$$
\rho V_{Sv}^2(\theta) = \frac{1}{2} \left[C_{33} + C_{44} + (C_{11} - C_{33}) \sin^2(\theta) - D(\theta) \right],
$$

$$(3.6)$$

and

$$
\rho V_{Sh}^2(\theta) = C_{66} \sin^2(\theta) + C_{44} \cos^2(\theta).
$$

where ρ is density and θ is phase angle, as opposed to group angle (Figure 3.1). $D(\theta)$ is compact notation for the quadratic combination showed in Equation 3.7

$$
D(\theta) \equiv \left\{ (C_{33} - C_{44})^2 \right.
$$
$$
+ 2 \left[2(C_{13} + C_{44})^2 - (C_{33} - C_{44})(C_{11} + C_{33} - 2C_{44}) \right] sin^2(\theta)
$$
$$
\left. + \left[(C_{11} + C_{33} - 2C_{44})^2 - 4(C_{13} - C_{44})^2 \right] sin^4(\theta) \right\}^{\frac{1}{2}}.
$$

$$(3.7)$$

In terms of elastic moduli, Equations 3.6 become Equations 3.8, where ϵ, γ and δ are anisotropy parameters.
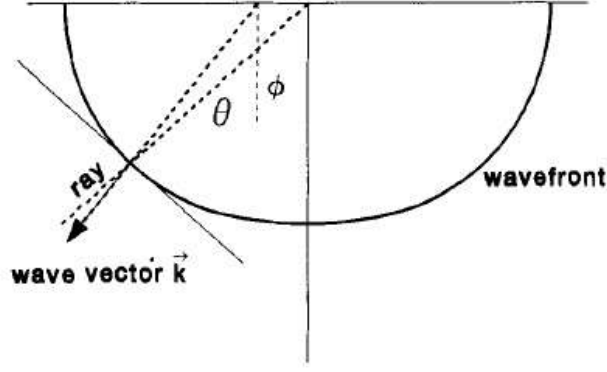
Figure 3.1: Phase (wavefront) angle θ and group (ray) angle ϕ. Modified from Thomsen (1986)[5].

$$
\begin{aligned}
\epsilon &\equiv \frac{C_{11} - C_{33}}{2C_{33}}, \\
\gamma &\equiv \frac{C_{66} - C_{44}}{2C_{44}} \text{ and} \\
\delta^* &\equiv \frac{1}{2C_{33}^2} 2\left(C_{13} - C_{44}\right),
\end{aligned}
\tag{3.8}
$$

ϵ is half fractional change in the P-wave velocity; γ is half fractional change in the S-wave velocity. Note that ϵ, γ and δ are dimensionless and have values smaller than 0.5, frequently much smaller.

The relationship between velocity and elastic coefficients is given by Equations 3.13:

$$
\begin{aligned}
\alpha_0 &= \sqrt{\frac{C_{33}}{\rho}}, \\
\beta_0 &= \sqrt{\frac{C_{44}}{\rho}},
\end{aligned}
\tag{3.9}
$$

where α_0 is the vertical P wave velocity, β_0 is the vertical S-wave velocity (Equations 3.13). The relationship between δ and δ^* in the last of the Equations 3.8 is shown in Equation 3.10

$$
\begin{aligned}
\delta &\equiv \frac{1}{2}\left[\epsilon + \frac{\delta^*}{1 - \beta_0^2/\alpha_0^2}\right] \\
&= \frac{(C_{13} + C_{44})^2 - (C_{33} - C_{44})^2}{2C_{33}(C_{33} - C_{44})}.
\end{aligned}
\tag{3.10}
$$

From Equations 3.6, 3.7 and 3.13

$$V_P^2(\theta) = \alpha_0^2 \left[1 + \epsilon sin^2(\theta) + D^*(\theta) \right],$$

$$V_{Sv}^2(\theta) = \beta_0^2 \left[1 + \frac{\alpha_0^2}{\beta_0^2} \epsilon \sin^2(\theta) - \frac{\alpha_0^2}{\beta_0^2} D^*(\theta) \right],$$

$$V_{Sh}^2(\theta) = \beta_0^2 \left[1 + 2\gamma sin^2(\theta) \right], \text{ with} \tag{3.11}$$

$$D^*(\theta) \equiv \frac{1}{2} \left(1 - \frac{\beta_0}{\alpha_0} \right) \left\{ \left[1 + \frac{4\delta^*}{(1 - \beta_0^2/\alpha_0^2)} \sin^2(\theta) \cos^2(\theta) \right. \right.$$
$$\left. \left. + \frac{4(1 - \beta_0/\alpha_0 + \epsilon)\epsilon}{(1 - \beta_0^2/\alpha_0^2)} \sin^4(\theta) \right]^{\frac{1}{2}} - 1 \right\}.$$

Tsvankin continued with this work in 1997[67] to develop anisotropy parameters to fully describe the orthorhombic case:

$$\epsilon = \frac{C_{22} - C_{33}}{2C_{33}},$$

$$\delta = \frac{(C_{23} + C_{44})^2 - (C_{33} - C_{44})^2}{(2C_{33}(C_{33} - C_{44})},$$

$$\text{and} \tag{3.12}$$

$$\gamma = \frac{(C_{12} + C_{66})^2 - (C_{11} - C_{66})^2}{(2C_{11}(C_{11} - C_{66})}.$$

$$V_{S1} = \sqrt{C_{44}/\rho} \tag{3.13}$$

and many other useful relationships and the formulation of non-hyperbolic normal moveout often observed in areas affected by an anisotropic subsurface.

Schoenberg and Helbig (1997)[50] offer a hybrid method to compute a special orthogonal case that is closer to the reality than simpler VTI or HTI models, useful for this work, where there are VTI layers with vertical fractures. Mah and Schmitt (2016)[6] present elastic constants for hexagonal and orthorhombic symmetries determined from phase velocity, which is presented on Table 3.1 and where stiffness is trivial for zero value showed. The use of C_{ij} means that the stiffness must be determined by an inversion procedure or that the required formula is complicated. For isotropic or hexagonal symmetries we can formulate all required independent moduli. For the orthorhombic case however, the off diagonal moduli, C_{12}, C_{13} and C_{23} become problematic. That is why it was computed the hexagonal C_{ij} and then vertical fractures were inserted after it.

The orthorhombic model of a vertically fractured medium is composed of two ele-

Table 3.1: Summary of elastic constants for hexagonal and orthorhombic symmetries determined from phase velocity measurements (Modified from Mah and Schmitt 2016)[6].

Coefficients	Hexagonal	Orthorhombic
C_{11}	$\rho\, V_P^2$ along any $\mathbf{n}$	$\rho\, V_P^2$ along $\mathbf{n} = [\pm1, 0, 0]$
C_{22}	Same as C_{11}	$\rho\, V_P^2$ along $\mathbf{n} = [0, \pm1, 0]$
C_{33}	$\rho\, V_P^2$ along $\mathbf{n} = [0, 0, \pm1]$	$\rho\, V_P^2$ along $\mathbf{n} = [0, 0, \pm1]$
C_{44}	$\rho\, V_S^2$ within the polarization $\mathbf{n} = [0, 0, \pm1]$ along any $\mathbf{n}$ within xy plane.	$\rho\, V_S^2$ with polarization $\mathbf{n} = [0, 0, \pm1]$ along $\mathbf{n} = [0, \pm1, 0]$ or with polarization $\mathbf{n} = [0, \pm1, 0]$ along $\mathbf{n} = [0, 0, \pm1]$
C_{55}	Same as C_{44}	$\rho\, V_S^2$ with polarization $\mathbf{n} = [0, 0, \pm1]$ along $\mathbf{n} = [\pm1, 0, 0]$ or with polarization $\mathbf{n} = [\pm1, 0, 0]$ along $\mathbf{n} = [0, 0, \pm1]$
C_{66}	$\rho\, V_S^2$ within the polarization $\mathbf{n} = [0, \pm1, 0]$ along $\mathbf{n} = [\pm1, 0, 0]$ or with the polarization $\mathbf{n} = [\pm1, 0, 0]$ along $\mathbf{n} = [0, \pm1, 0]$	$\rho\, V_S^2$ with polarization $\mathbf{n} = [\pm1, 0, 0]$ along $\mathbf{n} = [0, \pm1, 0]$ or with polarization $\mathbf{n} = [0, \pm1, 0]$ along $\mathbf{n} = [\pm1, 0, 0]$
C_{12}	C_{11} - $2C_{66}$	C_{12}
C_{13}	$\rho\, V_S^2$ - $2C_{44}$ - C_{11} along $\mathbf{n} = [0, \pm1/\sqrt{2}, \pm1/\sqrt{2}]$ or $[\pm1/\sqrt{2}, 0, \pm1/\sqrt{2}]$	C_{13}
C_{23}	Same as C_{13}	C_{23}
C_{14}	0	0
C_{15}	0	0
C_{16}	0	0
C_{24}	0	0
C_{25}	0	0
C_{26}	0	0
C_{34}	0	0
C_{35}	0	0
C_{36}	0	0
C_{45}	0	0
C_{46}	0	0
C_{56}	0	0

ments. The first is a TI background medium with a vertical axis of symmetry. The transverse isotropy may be attributed to fine layering, shales with vertical symmetry axes, or horizontal fractures. This background medium often deviates considerably from isotropy, with compressional and shear speeds varying by as much as 30%. In condensed (6 X 6 matrix) notation, the stiffness tensor of the transversely isotropic background medium with a vertical axis of symmetry is presented in Equation 3.5 with C_{11} - C_{12} - $2C_{66} = 0$ and the second element is a set of parallel vertical fractures.

According to Schoenberg and Douma (1988)[51], a set of parallel fractures may be specified by a symmetric non-negative definite 3 X 3 fracture compliance matrix **Z**. The stiffnesses and compliances of the long-wavelength equivalent homogeneous orthorhombic medium are functions of the five stiffnesses C_{11}, C_{33}, C_{55}, C_{13} , and C_{66} of the TI background medium and of the three positive fracture parameters Z_N, Z_V, and Z_H, where Z_N is the excess compliance normal to the fractures, Z_V is the excess vertical tangential compliance, and Z_H is the excess horizontal tangential compliance.

Across the fractures, the normal motion - the opening and closing - is uncoupled from tangential slip motion. Generally, the tangential displacement and the tangential component of the traction across the fractures are not collinear, except in two mutually perpendicular directions. If these directions are horizontal (parallel to fractures) and vertical (parallel to the z-axis), the fracture compliance matrix **Z** of the orthotropic fractures specifying the behavior of the fracture set is the diagonal

non-negative 3 X 3 matrix in Equation 3.14.

$$\mathbf{Z} = \begin{bmatrix} Z_N & 0 & 0 \\ 0 & Z_V & 0 \\ 0 & 0 & Z_H \end{bmatrix} \tag{3.14}$$

Hence, the compliance matrix of the equivalent medium, in the long-wavelength limit, to the VFTI medium is $(\rho\mathbf{C})^{-1} + \boldsymbol{\Delta}$, and its density-normalized stiffness matrix is given by Equation 3.15

$$\mathbf{C} = [\mathbf{C}^{-1} + \rho\boldsymbol{\Delta}]^{-1} = \mathbf{C}[\mathbf{I} + \rho\boldsymbol{\Delta}\mathbf{C}]^{-1} \tag{3.15}$$

where $\mathbf{I}$ is the 6 X 6 identity matrix.

$$0 \leq \delta_N \equiv \frac{Z_N \rho C_{11}}{1 + Z_N \rho C_{11}} < 1,$$
$$0 \leq \delta_V \equiv \frac{Z_V \rho C_{44}}{1 + Z_V \rho C_{44}} < 1, \tag{3.16}$$
$$0 \leq \delta_H \equiv \frac{Z_H \rho C_{66}}{1 + Z_H \rho C_{66}} < 1.$$

The calculation outlined on Equation 3.15 using quantities introduced in Equation 3.16 results in Equation 3.17. It allows the formation of the effective orthorhombic elastic moduli matrix, including estimates for the off diagonal entries C_{12}, C_{13} and C_{23}.

$$\mathbf{C_{ij}} = \begin{bmatrix} C_{11}(1-\delta_N) & C_{12}(1-\delta_N) & C_{13}(1-\delta_N) & 0 & 0 & \\ C_{12}(1-\delta_N) & C_{11}\left(1-\delta_N\frac{C_{12}^2}{C_{13}^2}\right) & C_{13}\left(1-\delta_N\frac{C_{12}}{C_{11}}\right) & 0 & 0 & 0 \\ C_{13}(1-\delta_N) & C_{13_b}\left(1-\delta_N\frac{C_{12}}{C_{11}}\right) & C_{33}\left(1-\delta_N\frac{C_{13}^2}{C_{11}C_{33}}\right) & 0 & 0 & 0 \\ 0 & 0 & 0 & C_{44} & & \\ 0 & 0 & 0 & 0 & C_{44}(1-\delta_V) & \\ & & & & & C_{66}(1-\delta_H) \end{bmatrix} \tag{3.17}$$

Conditions for "mild anisotropy" are: 1 - that there be no anomalous polarization in any of the coordinate planes (Helbig and Schoenberg, 1997[50]), and 2 - that the highest q_S speed (over all directions) be smaller than the lowest q_P speed (over all directions).

$$C_{23} + C_{44} > 0,$$
$$C_{13} + C_{55} > 0,$$
$$C_{12} + C_{66} > 0, \tag{3.18}$$
$$\text{and}$$
$$\min(C_{11}, C_{11}, C_{33}) > \max(C_{44}, C_{55}, C_{66})$$

First three Equations in 3.18 could be strengthened by requiring that C_{23}, C_{13}, C_{12} > 0 (a generalization of requiring an isotropic medium to have a positive Poisson's ratio). According to Schoenberg and Helbig (1997)[50] those are generalizations of the mild anisotropy conditions discussed in Carrion *et al.* (1992)[74].

3.3.2 The Computational Code

The computational code *anisinpa* is based on the reflectivity method. Several modifications were made under the advising of Dr. Garossino, such as to build a FreeUSP routine *anisynpausp* which outputs USP format data easily plotted in xsd (a visualization box in FreeUSP platform). During his work many memory limitations were removed concerning the maximum number of output traces per record, the maximum number of horizons in the model, etc. Details of Garossino's modifications can be found in the work of Alison *et al.* (2015)[72].

The reflectivity method is a wavenumber or slowness integration method (MÜLLER, 1985[70]). Its name was introduced by Fuchs and Müller (1971)[75] to describe a technique in which all multiple reflections and conversions between wave types were retained in part of the structure. The function which is integrated is mainly the reflection coefficient, or the reflectivity, of a layered medium. The method accounts for amplitude information and the travel times of the earliest arriving phases. Since anisotropy affects amplitude and direction information in seismic data, the reflectivity method is appropriate for the modeling.

The program package includes a model file called anisi.f and by looking at that we realized that anisynpa could deal with a significant number of different layer symmetries:

- 'I' - Isotropic

- 'T' - Transversely Isotropic

- 'O' - Orthorhombic

- 'R' - Rotated Orthorhombic

- 'M' - Monoclinic

- 'C' - Triclinic

Each layer type required the user to supply all independent elastic constants appropriate for the chosen symmetry. Constants could be supplied as C_{ij}s, stiffness constants used to form the C_{ij} stiffness tensor, or V_{ij}s according to Equation 3.19

$$V_{ij} = \sqrt{\frac{C_{ij}}{\rho}}, \tag{3.19}$$

where ρ is the layer density. For Isotropic layering two independent constants are required: V_{33}, V_{44} or C_{33}, C_{44}. For Transversely Isotropic layering, 5 independent constants are required: V_{11}, V_{33}, V_{44}, V_{66} and V_{13} or C_{11}, C_{33}, C_{44}, C_{66} and C_{13}. Orthorhombic layering requires 9 independent constants: V_{11}, V_{22}, V_{33}, V_{44}, V_{55}, V_{66}, V_{12}, V_{13} and V_{23} or C_{11}, C_{22}, C_{33}, C_{44}, C_{55}, C_{66}, C_{12}, C_{13} and C_{23}.

Rotated orthorhombic layering demands the same 9 independent constants along with a rotation angle. The rotated orthorhombic stiffness tensor is computed within the program using the supplied constants and rotation angle. The author has not dealt with the Monoclinic or Triclinic cases.

For each layer one may also specify the layer thickness, density and quality factors governing both P and S wave propagation. The crux of the model parametrization is the computation of the required C_{ij}s or V_{ij}s. Some research for reasonable formulations for the Isotropic (I) and Transverse Isotropic (T) cases is fundamental.

The Orthorhombic (O) case is built through the creation of an orthorhombic hybrid by imposing vertical fractures on a VTI layer forming a Vertical Fracture Transverse Isotropy (VFTI) layer using Equation 3.17 and conditions for mild anisotropy from Equations 3.18. Orthorhombic C_{ij}s could be created for the effective layer by multiplying the VTI stiffness tensor by a 3x3 fracture compliance matrix (Schoenberg and Helbig 1997[50]).

To properly parameterize plane wave, the first step is to have the program computing the entire synthetic response. Parameters like minimum ray velocity (V_{min}) had to be worked out, along with trace and sample spacings, for each model under consideration to avoid partial response, and aliased output, temporally or spatially. The coding makes it easy to specify free surface or half space at top of model, or even direct arrivals are easily turned on or off.

3.4   Computational Modeling

The orthorhombic geologic model is generated based on real layers Mesaverde Sandstone and Mesaverde Shale with vertical fractures described in the work of Thomsen (1986)[5]. Multicomponent seismic modeling is made for nine components (9C) with three-component (3C) source and 3C sensors.

Anisinpausp outputs 9 binary data sets, indexed for 3D source and receiver alignments i and j where the first number represents the source orientation, the second, the particle motion orientation detected by the receiver. Then 11, 12, 13, 21, 22, 23, 31, 32, 33 are pairs ij which stand for the x,y and z axes. The output format is binary traces with no headers, similar to the DDS data type.

After several tests for survey parameters the model is written in a file for the code to read it. These parameters are modifiable any time, but other tests are needed for aliasing and completude in the seismogram. The model was chosen to create 6 seconds of data, at a 4 ms sample rate, $V_{min} = 1000$ m/s, 1600 ray parameters, taper in ray parameter space equals to 80%, filter using a 28 Hz Ricker wavelet, three component receivers at zero depth, offsets from 0-5980 m along the x axis, every 20 meters, 300 geophones, and three layers specified. All layers are defined using computed V_{ij}s according to Section 3.3 .

Consider two modeled examples presented below: first is a three-layer model with isotropic layers and second is a three-layer model where one is anisotropic due to vertical fractures. All the models presented are free surface half-space without direct arrival.

3.4.1   Isotropic Model

In this section, results for the isotropic computational modeling are presented. The model is three-layer based presented in Figure 3.2. Each layer is isotropic and their velocities, density and thickness are described in Table 3.2.

Table 3.2: Parameters for each layer in the isotropic model.

Layer	Lithology	V_P (m/s)	V_S (m/s)	ρ (g/cm³)	V_P/V_S	Thikness (m)
Layer 1		2,000	1,000	2.3	2.0	1,000
Layer 2		2,820	1,480	2.7	1.9	1,000
Layer3		4,000	2,000	3.0	2.0	0

Seismograms for isotropic three-layer model are presented in Figure 3.3 where nine
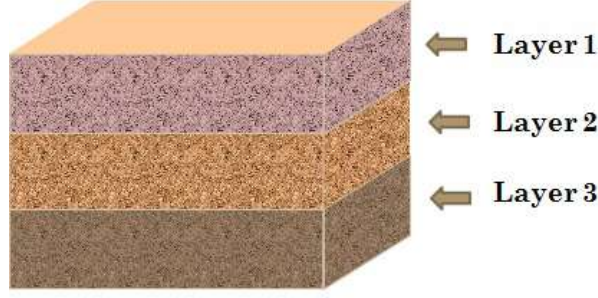
Figure 3.2: Three layer-model with isotropic layers.

panels have P, S, and converted P- to S-wave and S- to P-wave events. From now on, seismograms and panels have the same meaning in this work. Vertical axis shows time in seconds and horizontal axis shows offset in meters. Over each panel its identification ij is presented. Notice that panels 12, 21, 23, and 32 have no data because the layers are isotropic as described by Liu and Martinez (2012)[3].
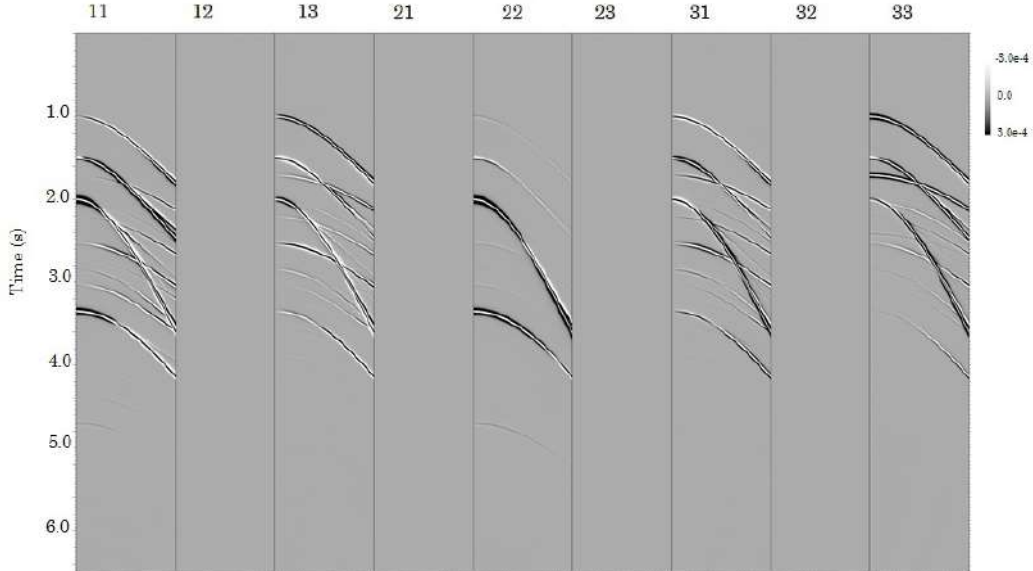
Figure 3.3: 9C panels for three layer isotropic model. Numbers on the top show source-receiver for the panel.

Figure 3.4 shows event identification for panels 11 and 13. Panel 11 is source polarized x direction and receiver polarized x direction. Early in time there is the P-wave arrival (PP1) at 1.0 s from the first interface, which shows low energy due to its nature of vertical polarization arriving over the horizontal geophone.

Following the time, at 1.33 s there is the converted-wave (PS1) from the first interface. Zero to low energy at zero offset is characteristic of converted-waves. Next event has too low energy and it is a P-wave (PP2) from the second interface at 1.66 s followed by the first monomode S-wave in x direction (SS1) at 2.0 s, which has strong energy from short to long offsets. That is the S_x to S_x wave.

36
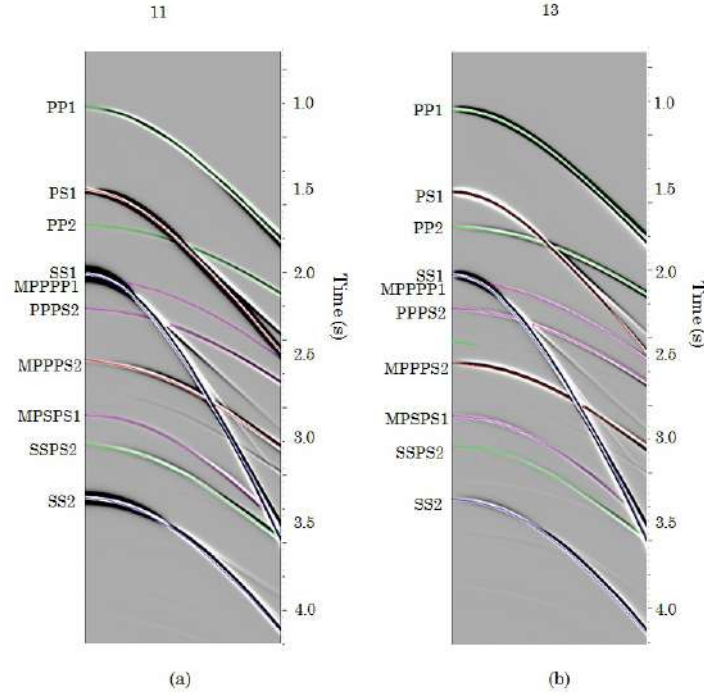
Figure 3.4: Panels show (a) source polarization x, receiver polarization x, and (b) source polarization x, receiver polarization y.

First multiple (MPPPP1) is present at 2.0 s. Converted wave (PPPS2) from the second interface is at 3.21 s. Multiple of converted-wave from the first interface (MPPPS1) appears at 2.50 s with low energy at short offsets. Converted wave (MPSPS2) from the second interface is at 3.21 s. Multiple of converted-wave from the first interface (MPSPS1) appears at 2.50 s with low energy at short offsets. Notice that there is no conversion S_X to S_Y (S_V to S_H). Converted-waves from second interface PPPS2 appear at 3.21 s. S-waves from the second interface show up at 3.35 s with strong energy.

Panel 13 is source polarized x direction and receiver polarized z direction. Almost all the same events are seen in this panel as in panel 11. S-wave events show up with low energy at short offsets, since it is a converted-wave, and strong energy at long offsets. P-wave arrivals (PP1, PP2) show stronger energy in panel 13 when comparing to 11, in contrast, S-wave arrivals (SS1 and SS2) show lower energy.

Figure 3.5 shows event identification for panel 22. Panel 22 is source polarized y direction and receiver polarized y direction. Only S-wave from first and second interfaces appear with strong energy at panel 22, which is S_X source to S_X receiver.

Figure 3.6 shows event identification for panels 31 and 33. Panel 31 is source polarized z direction and receiver polarized x direction. S-wave events still have good energy and P-waves appear.
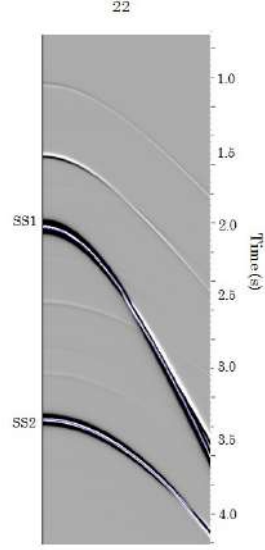
Figure 3.5: Panel shows source polarization y and receiver polarization y.
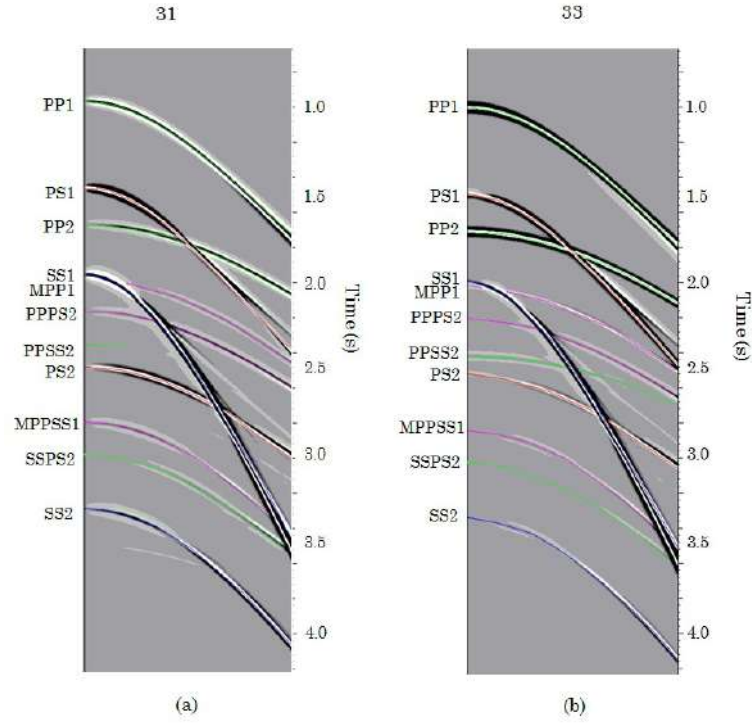
Figure 3.6: Panels show (a) source polarization x, receiver polarization z, and (b) source polarization z, receiver polarization z.

Panel 33 is source polarized z direction and receiver polarized z direction. P-wave events appear even stronger than they do at any other panel. S-waves lose energy and converted-waves have too low energy at the panel 33. P-waves have opposite polarizations when comparing 31 to 33 panels. Table 3.3 shows arrival times for event identification at the above panels.

Notice that S-waves (and PS waves) present a specific pattern. At the P-wave critical angle, the S-wave polarity changes as well as the phase. P-wave critical angle is $\theta_{cr} = 45.17°$ at the offset 1005 m for the first interface and $\theta_{cr} = 44.82°$ at the approximate offset of 1987 m for the second layer.

Table 3.3: Isotropic seismogram event identification.

Event	Arrival time (s)	Description
PP1	1.0	P-wave converted at the first interface
PP2	1.66	P-wave from the second interface
PS1	1.33	Converted P down, S up from the first interface
SS1	2.00	S-wave from the first interface
SS2	3.24	S-wave from the second interface
PSSS2, SSSP2	2.68	Converted-wave at the first interface
SPSS2, SSPS2	2.54	Converted-wave at the first interface
PPPS2, SPPP2	3.21	Converted-wave at the second interface
PPSP2, PSPP2	1.93	Converted-wave at the second interface
PPSS2, PSPS2	2.19	Converted-wave at the second interface
SSPP2, SPSP2	2.19	Converted-wave at the second interface
SPPS2	2.09	Converted-wave at the second interface
MPPPP1	2.00	P-wave multiple from the first interface
MSSSS1	4.00	S-wave multiple from the first interface
MPPPS1, MSPPP1	2.50	Converted-wave multiple from the first interface
MPPSS1, MPSPS1	3.00	Converted-wave multiple from the first interface
MPSSS1, MSSSP1	3.50	Converted-wave multiple from the first interface

When source (or receiver) is rotated at an angle θ from the receiver (or source), survey panels 12, 21, 23 and 32 present energy because receiver i and source j directions are not aligned anymore. Consider Figure 3.7 where receiver polarization is rotated 45° clockwise from the source. Events presented at the new panels are the same presented in the first modeling, but now they appear over all seismograms.

Even for the case when there is no anisotropy, if source i and receiver i are not polarized in the same direction, as well as source and receiver j, energy from source polarized i spreads to all the receivers, as well as source polarized j and k, as shown in Figure 3.8.

Notice i and j from source (S) not lined up with i and j from receiver (R). If there is vectorial fidelity in the survey, one can rotate the geophone to find the directions of lowest energy (SS events) offline (ij with $i \neq j$ varying from 1 to 2). That is why vectorial fidelity is of great importance when performing a survey. In the case of the ocean bottom nodes (OBN) technique, a 3D survey is performed and geophone rotations are used to discover the source or inline direction of the survey and correct for geophone deviation.
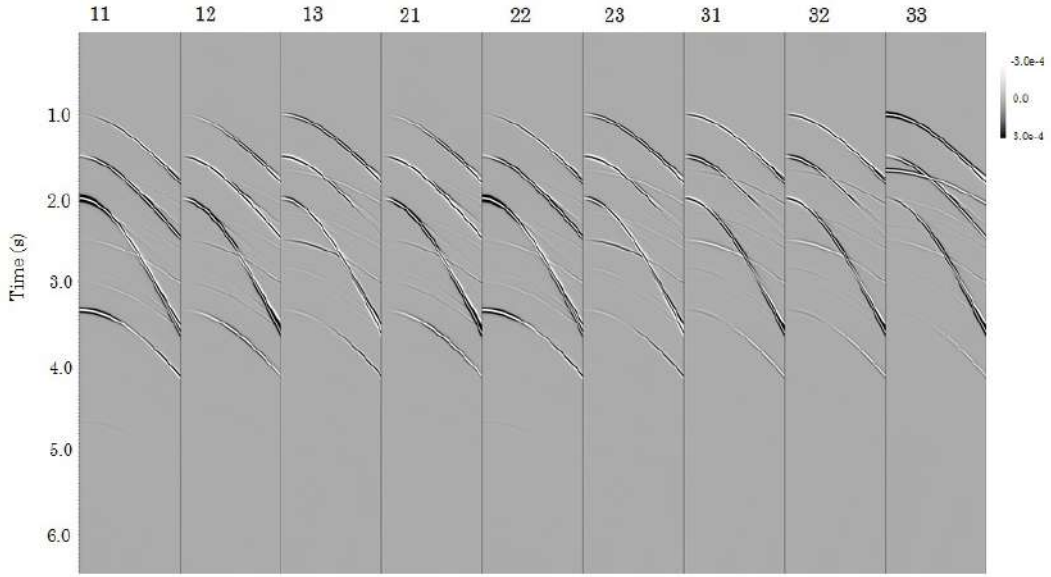
Figure 3.7: Panels show (a) source polarization x, receiver polarization z, and (b) source polarization z, receiver polarization z.
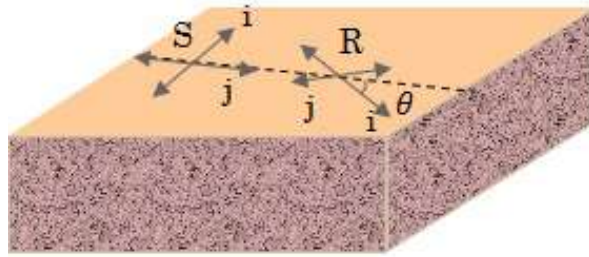
Figure 3.8: Scheme for 2C source (S) and 2C receiver (R) polarizations not aligned.

3.4.2 Anisotropic Models

Orthorhombic Modeling

Vertical fractures and horizontal fine layering combine to form a long-wavelength equivalent orthorhombic medium. Such media constitute a subset of all orthorhombic media. Orthorhombic elastic symmetry is the lowest symmetry for which the slowness surface (the solution of the Christoffel equation) is bicubic rather than sextic. Various properties of orthorhombic media, such as the number and location of conical points and longitudinal directions, may be derived from the slowness surface or, because of its bicubic character, the squared slowness surface, which is a cubic surface.

From the occurrence and angular orientation of some of these distinctive features, conclusions can be drawn with respect to the properties of the medium and to the parameters of the assumed underlying causes of the anisotropy. The estimation

of these more subtle properties gains greater importance with the proliferation of multi-azimuthal seismic surveys and the ability to drill along ever-more complicated 3-D well trajectories. In this section computational modeling of VTIF anisotropic seismic data based on Schoenberg and Helbig's theory showed in Section 3.3 is presented.

The model showed in Figure 3.9 is composed of three layers which parameters are described in Table 3.4. The first layer is isotropic, the second is vertically fractured, and third is isotropic. C_{ij} coefficients for the orthorhombic media where computed from Equation 3.17 from a VTI media.
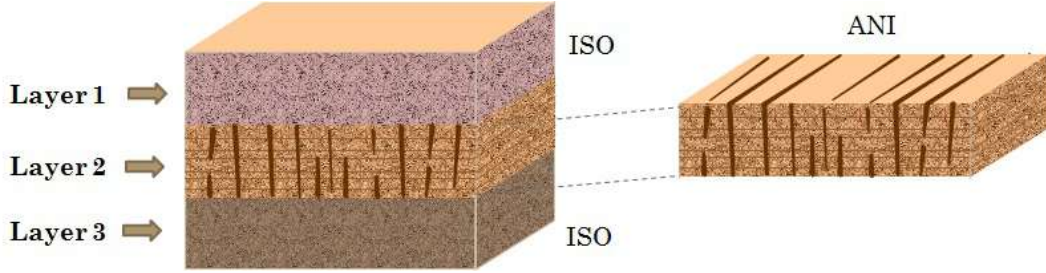
Figure 3.9: Three layer-model: first is isotropic, second is vertically fractured, and third is isotropic.

Table 3.4: Parameters for each layer in the anisotropic model.

Layer		V_P (m/s)	V_S (m/s)	ρ (g/cm^3)	V_P/V_S	Thickness (m)	ϵ	δ	γ
Layer 1	Mesaverde Sandstone	4,237	3,018	2.69	1.40	1,000	0.036	0.039	0.030
Layer 2	Mesaverde Shale	3,901	2,682	2.64	1.45	1,000	0.137	0.012	0.026
Layer3	Mesaverde Sandstone	4,237	3,018	2.69	1.40	0	0.036	0.039	0.030

Figure 3.10 shows the rose wind with all angles on the left and their relation with fractures (main axes of symmetry) on the right which are lined up with a proposed North. Axes x and y are also presented in the figure. At 0°, y is aligned with North (and with fractures) and x and y are susceptible to clockwise rotations keeping 90° in between always. In other words, when the geophone is rotated in the survey, the angle increases from 0° clockwise. Notice black arrows every 45° which are going to be pointed for following analysis.

C_{ij} required for the computational code to model the orthorhombic media are obtained by:

$C_{11} = C_{11b}(1\text{-}\delta_N)$,

$C_{22} = C_{22b}(1\text{-}\delta_N(C_{12b}^2/C_{11b}^2))$,

$C_{33} = C_{33b}(1\text{-}\delta_N(C_{13b}^2/(C_{11b}C_{33b}^2)))$,

$C_{44} = C_{44b}$,
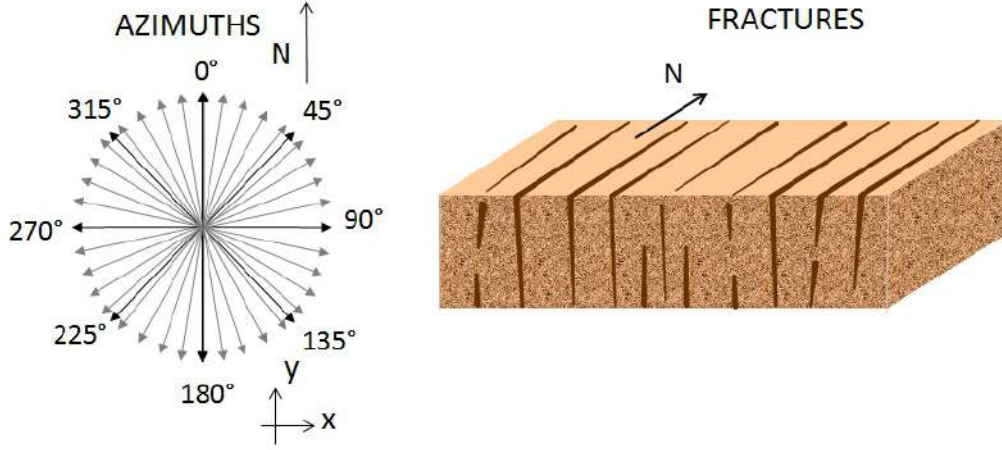
Figure 3.10: Scheme for the fracture orientation in the methodology.

$$C_{55} = C_{44b}(1\text{-}\delta_V),$$

$$C_{66} = C_{66b}(1\text{-}\delta_H),$$

$$C_{12} = C_{12b}(1\text{-}\delta_N),$$

$$C_{13} = C_{13b}(1\text{-}\delta_N), \text{ and}$$

$$C_{23} = C_{23b}(1\text{-}\delta_N(C_{12b}/C_{11b})),$$

where, b indicates original C_{ij}. The code needs V_{ij} as input. C_{ij} is converted into V_{ij} by Equation 3.19. Below there are values computed for V_{ij} this modeling.

$V_{11} = 4158.44$, $V_{22} = 4421.19$, $V_{33} = 3898.74$, $V_{44} = 2682.00$, $V_{55} = 2374.74$, $V_{66} = 2346.24$, $V_{12} = 1995.25$, $V_{13} = 1219.46$, $V_{23} = 1282.45$.

Figure 3.11 shows the seismograms with panels for survey at 0°, aligned with fractures. Colors stand for events showed in Figures 3.12, 3.13 and 3.14, where P-wave, S-wave and C-wave are shown according to Table 3.5.
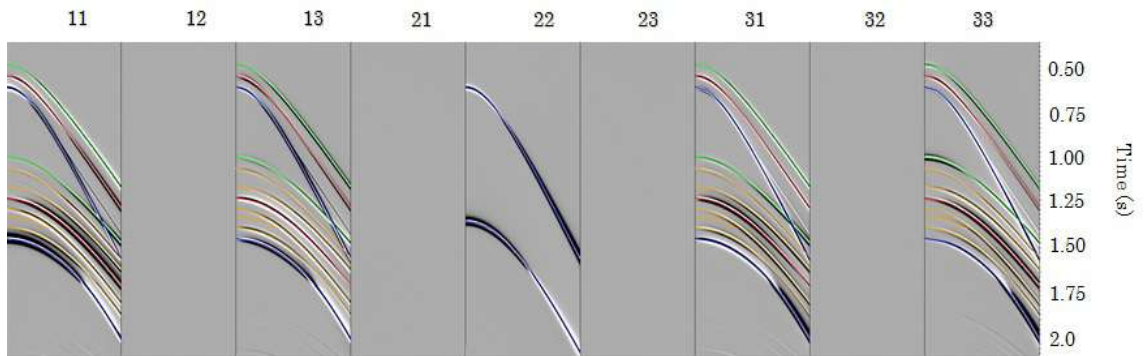
Figure 3.11: Seismograms for survey at 0° with fractures.

Table 3.5: Orthorhombic model arrival time by event.

Event	Arrival time (s)	Description
PP1	0.47	P-wave converted at the first interface
PP2	0.98	P-wave from the second interface
PS1	0.55	Converted P down, S up from the first interface
SS1	0.66	S-wave from the first interface
SS2	1.40	S-wave from the second interface
PSSS2, SSSP2	1.27	Converted-wave at the first interface
SPSS2, SSPS2	1.27	Converted-wave at the first interface
PPPS2, SPPP2	1.06	Converted-wave at the second interface
PPSP2, PSPP2	1.06	Converted-wave at the second interface
PPSS2, PSPS2	1.16	Converted-wave at the second interface
SSPP2, SPSP2	1.16	Converted-wave at the second interface
SPPS2	1.90	Converted-wave at the second interface

Figure 3.12 shows event identification for panels 11 and 13 (survey at 0°). Notice the lack of energy for panels 12, 21, 23 and 32, which means that there is no conversion from P- to S_H-wave, from S_V to S_H-wave, neither from S_H to P or S_V in the survey when aligned with fractures. Panel 11 is source polarized x direction and receiver polarized x direction. Early in time there is the P-wave arrival (PP1) at 0.47 s from the first interface (Mesaverde Sandstone - Mesaverde Shale), which shows low energy due to its nature of vertical polarization arriving over the horizontal geophone.
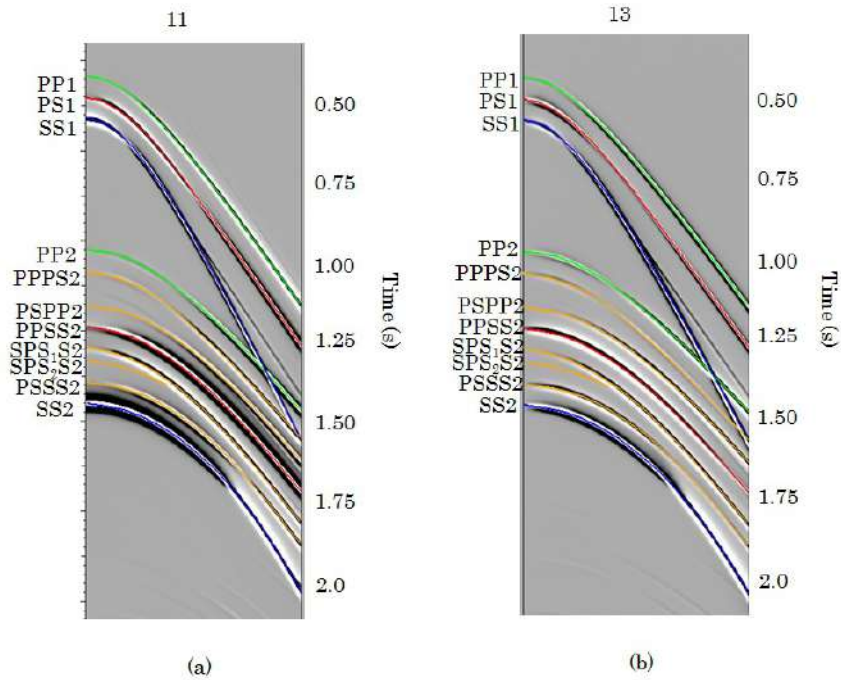
Figure 3.12: Event identification for panel 11 and 13.

The next event in time, at 1.51 s there is the C-wave PS1 at the first interface. Then, the first S-wave reflected at the first interface SS1 appears at 0.66 s with strong

energy as expected in the horizontal geophone. At the second interface several other evens are shown as follows.

The P-wave from the second interface is PP2 which shows up close to 1.24 s, followed by C-waves showed in Table 3.5. The last event is SS2 from the second interface. Multiples reverberations are show in Figures 3.11, 3.15 and 3.16 deeper in time, but they are not our focus in this work, so they were neglected during analysis.

Figure 3.13 shows event identification for panel 22. Panel 22 is source polarized y direction and receiver polarized y direction. Only S-wave from first and second interfaces appear with strong energy at panel 22, which is S_Y source to S_Y receiver. Notice that the event SS1 and SS2 change in phase after the P-wave critical angle at the corresponding layer.
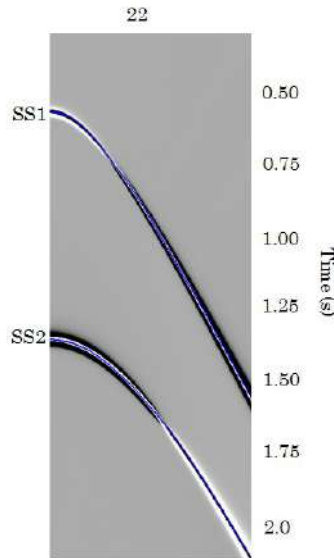
Figure 3.13: Event identification for panel 22.

Figure 3.14 shows event identification for panels 31 and 33. Panel 31 is source polarized z direction and receiver polarized x direction. S-wave events still have good energy and P-waves appear.

Consider the case where geophones are rotated clockwise by 45° from the fractures. Figure 3.15 shows the event identification for all panels. Notice that there are two SS2 arriving at different times. This is due to S-wave splitting which happened at the second layer.

Consider the case where geophones are rotated clockwise by 90° from the fractures, events are showed in Figure 3.16. Notice at panel 22 that SS2 arrives later in time, because the alignment is orthogonal to fractures, then S-wave faces resistance to travel.
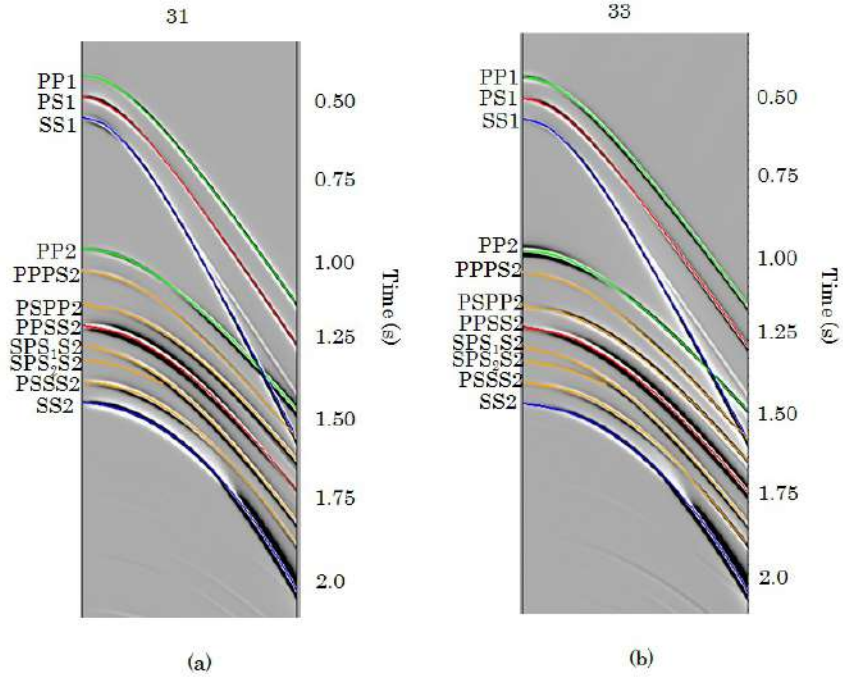
Figure 3.14: Event identification for panels 31 and 33 for survey at 0°.
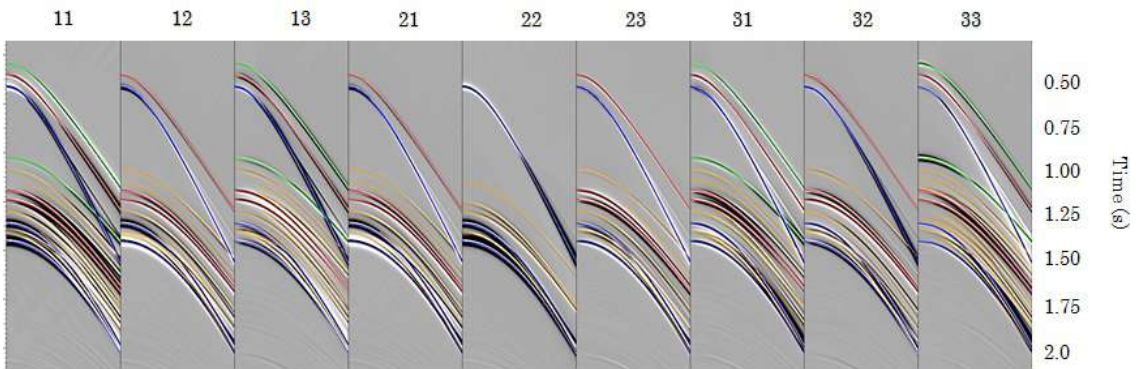
Figure 3.15: Event identification for all panels for survey at 45°.
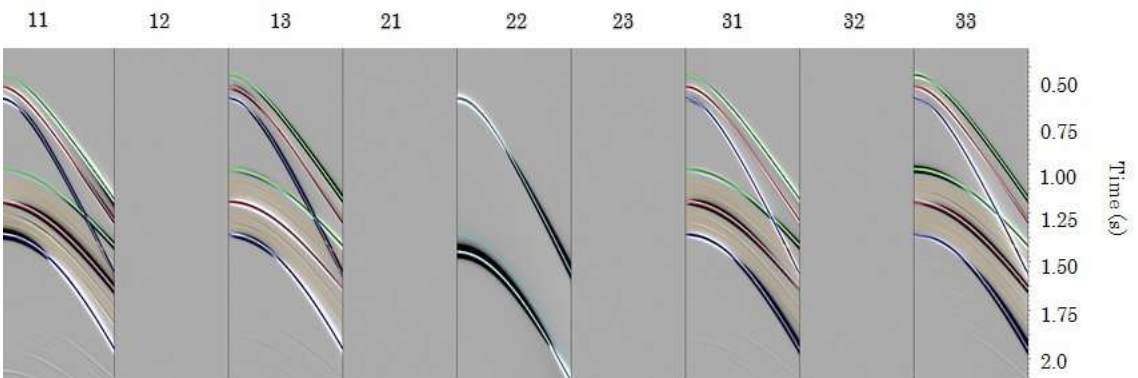
Figure 3.16: Seismograms for survey at 90° with fractures.

C-wave Analysis

45

When one focuses on the vertical sensors, he/she is looking mainly at energy from vertical wave polarization that reflected and/or converted to vertical polarization. Nonetheless, other waves can occasionally convert part of their energy to vertical polarization, therefore, appearing in those sections. In this subsection the triplet of traces at 180 m offset from panels 13, 23 and 33 are showed. Remember that 13 is source x and receiver z, 23 is source y and receiver z, and 33 is source z and receiver z.

Figure 3.17 presents the triplet of traces at vertical sensors for survey at 0° to fractures (aligned). From Table 3.5 we can see first interface reflections close to 0.47 s and second interface reflections around 0.98 s.
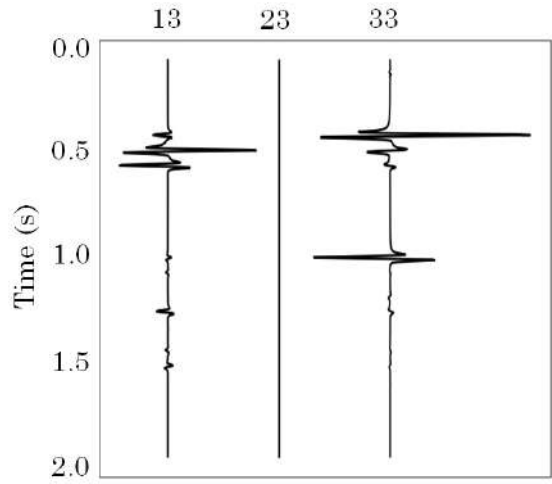
Figure 3.17: Traces 31, 32 and 33. Survey is 0° with fractures.

Event seen at 0.47 s at trace 33 is PP1 which is present at the panel 31 with lower amplitude due to conversion. Event at 0.98 s is PP2 which have traveled through the fractured layer. It is possible to notice some energy left from other events that can also be seen in Figure 3.11.

Figure 3.18 shows the triplet from survey making 45° with fractures. Panels 13 and 23 show little energy from the S-wave splitting event.

Figure 3.19 shows the triplet from survey making 90° with fractures. No meaningful difference is noticeable from the comparison between the triplets at 0° and 90°.

S- to S-wave Analysis

Now if one focuses on the horizontal sensors, he is looking mainly at energy generated with horizontal polarization that reflected and/or converted to horizontal polarization. In this subsection the quartet of traces at 180 m offset from panels 11, 12, 21 and 22 are showed. Remember that 11 is source x and receiver x, 12 is source

46
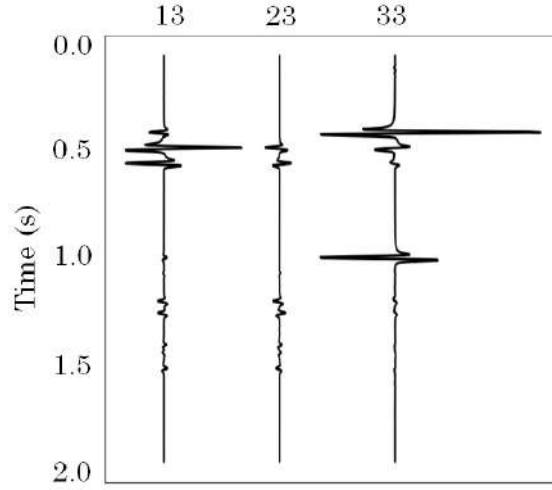
Figure 3.18: Traces 31, 32 and 33. Survey is 45° with fractures.
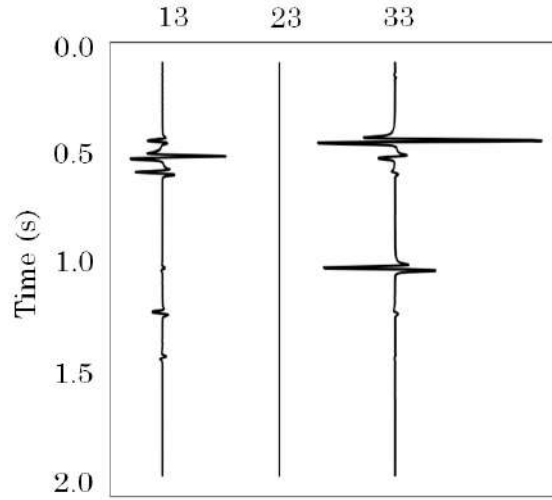
Figure 3.19: Traces 31, 32 and 33. Survey is 90° with fractures.

x and receiver y, 21 is source y and receiver x, and 22 is source y and receiver y.

Figure 3.20 presents the quartet for survey at 0° with fractures (aligned). From Table 3.5 we can see first interface reflections close to 0.66 s and second interface reflections around 1.4 s. Traces 12 and 21 are zeroed since the survey is aligned with the main axis of symmetry in the medium, then, there is no conversion S_x to S_y and *vice − versa*.

According to Figure 3.20, the event from the second interface, which have traveled through the fractures at layer 2, arrives first at the panel 22 (SS2^f) and later on panel 11 (SS2^s). One can clearly see energy at offline receivers (12 and 21) which are converted SS waves. At t = 0.66 s (or around it) there is the S-wave reflection from the first interface. Close to t = 1.4 - 1.5 s there is the S-wave from the second interface, which has traveled through the fractured layer.
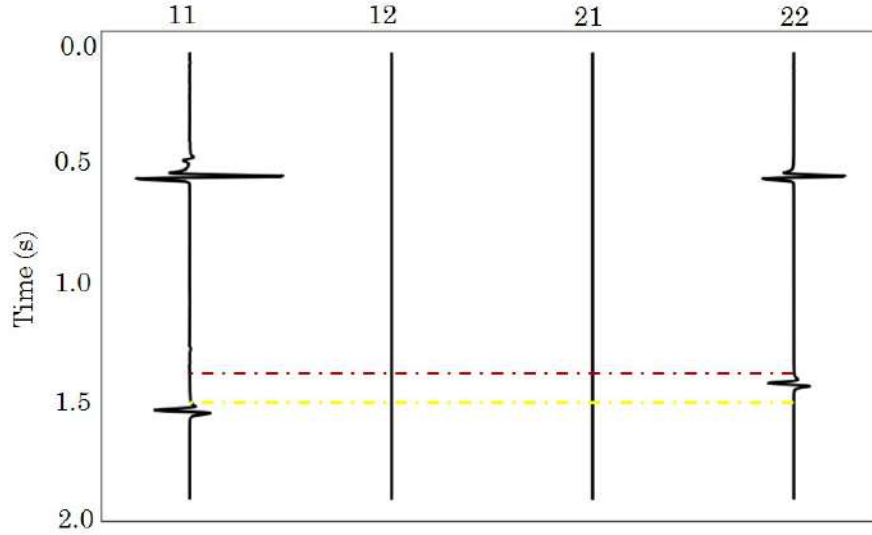
Figure 3.20: Traces 11, 12, 21 and 22. Survey is 0° with fractures.
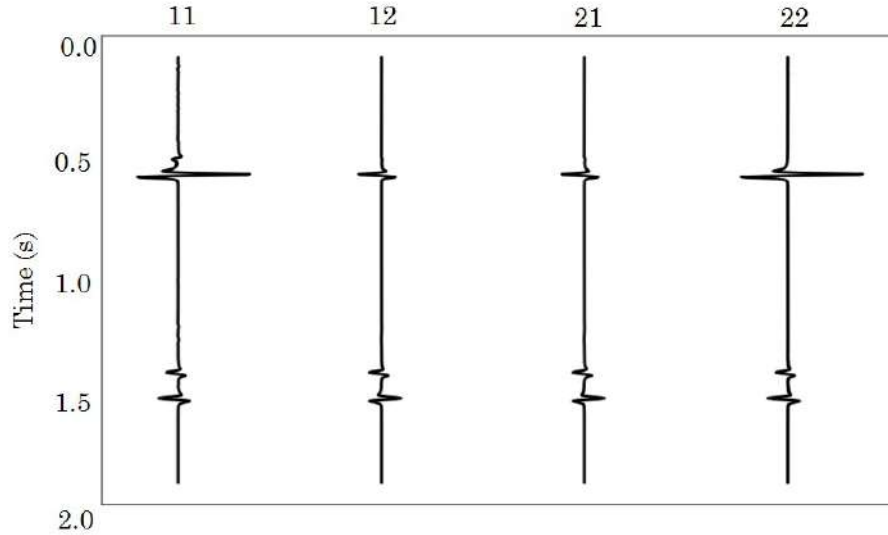
Figure 3.21: Traces 11, 12, 21 and 22. Survey is 45° with fractures.

When the survey is rotated by 90° from the fracture alignment as showed in Figure 3.22 data is similar to the data showed in Figure 3.20, but now, $SS2^f$ is polarized 11 direction then it arrives earlier in 11 and there is no data at 12 and 21 panels due to the alignment between the geophones and the symmetry axis in the medium. Same delay in time should be presented by $SS2^s$ - $SS2^f$.

If the survey is 30° with fractures (Figure 3.23) the amount of energy at the S-wave splitting for the second interface is proportional to the angle ($SS2^f$ and $SS2^s$ showed close to 1.4 s).

Consider the comparison of panel 22 with source polarization at 0°, 45° and 90° showed in Figure 3.24. A first S-wave reflection (SS1) happens at the first interface,

48
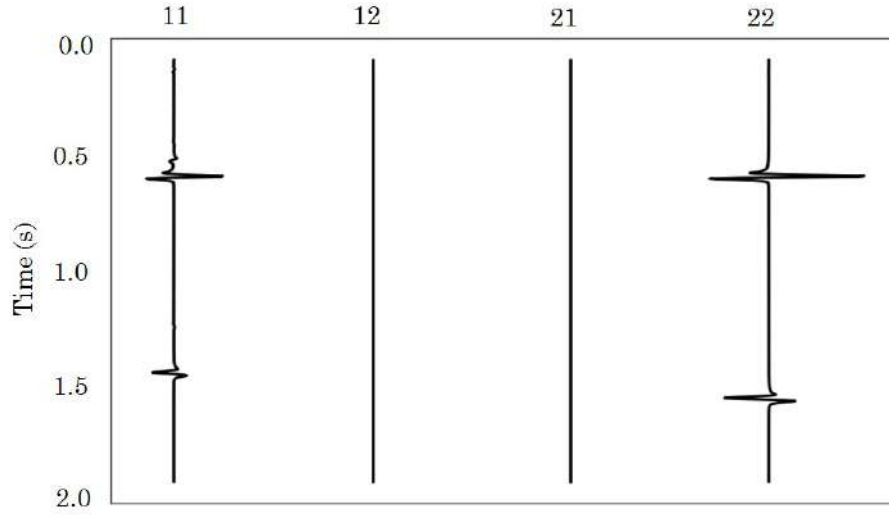
Figure 3.22: Traces 11, 12, 21 and 22. Survey is 90° with fractures.
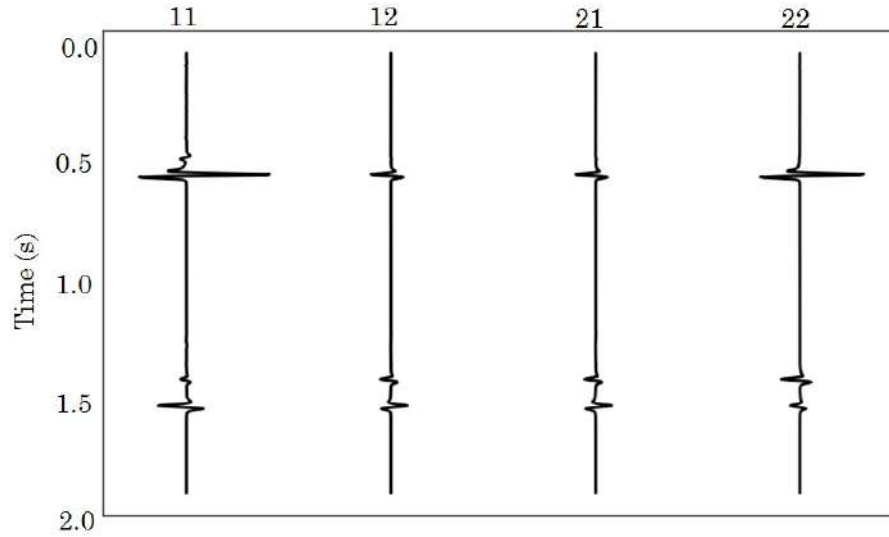
Figure 3.23: Traces 11, 12, 21 and 22. Survey is 30° with fractures.

and later in time a second S-wave event reflection from the second interface shows up (SS2).

As one could see in Figures 3.20, 3.21 and 3.22, S-wave from the second interface arrives at two different times with different amounts of energy depending on the azimuth, and both can be seen at any angle different from $n\pi/2$ (for n integer)(see Figures 3.21 and 3.23). SS2 clearly presents the S-wave spitting. In addition, the delay in time seems to decrease with offset.

Converted P- to S-wave Analysis

Converted P- to S-waves are showed for the offset $= 180$ m below in panels 31 and 32, while 33 records vertical polarized energy. Remember that for each pair ij, i stands

49
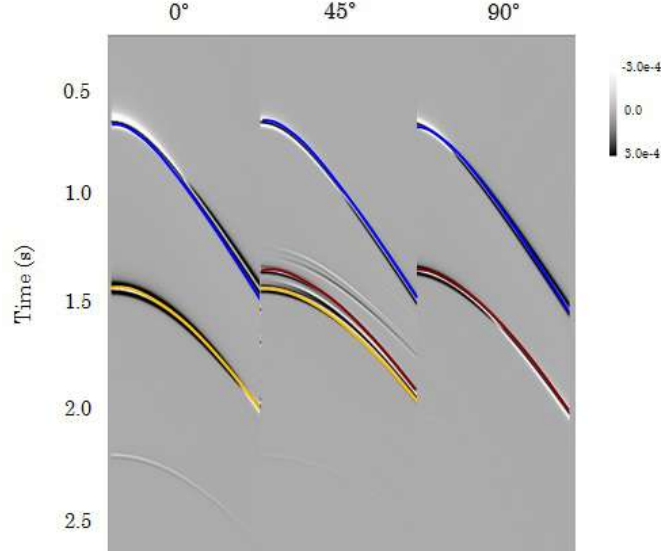
Figure 3.24: Panel 22 at 0°, 45° and 90°.

for source polarization and j for receiver polarization, and that 1 is polarized x, 2 is polarized y and 3 is polarized z direction. In other words, the panel 31 records energy polarized x direction including P- to S-wave inline conversions. While 32 records energy from polarization y including P- to S-wave offline, the well known PS_H wave. Panel 33 records z polarized energy, including the monomode P-waves.

Figure 3.25 shows panels 31, 32 and 33 in (a) for survey is 0° with fractures. Vertical axis is time from 0 to 2.0 seconds. Zoom in at the time 0.3 s to 0.8 s in (b) shows reflections from the first interface. The first one with large amplitude at 33 is PP1 close to time 0.47 s, which appears slightly perceptible at 31 due to vectorial conversion from non-zero offset. The second event is the C-wave PS1 that appears at 0.55 s which left some energy for the panel 33 with short amplitude. The third event is some of the energy from SS1 event which appears close to 0.66 s.
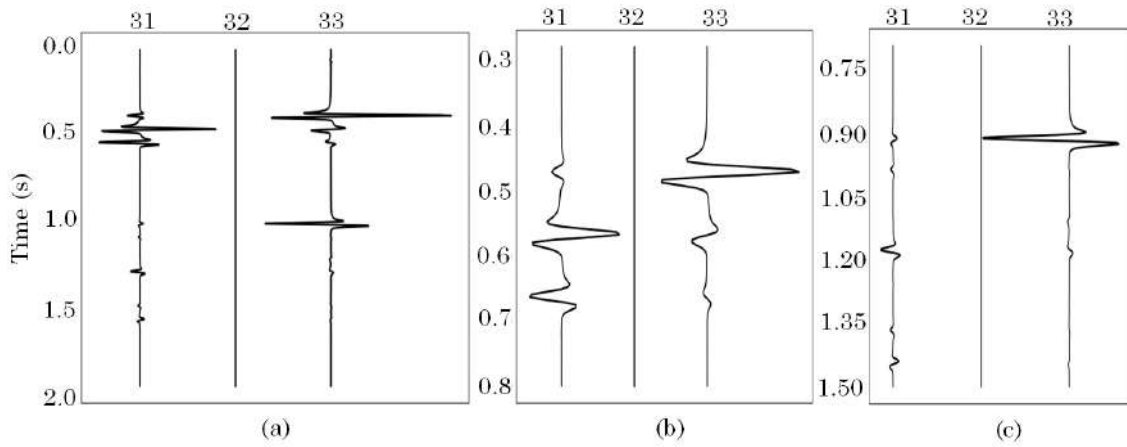
Figure 3.25: Traces 31, 32 and 33. Survey is 0° with fractures.

Zoom in at the time 0.75 s to 1.50 s in Figure 3.25 (c) shows PP2 between 1.0 s and 1.2 s. Both PP1 and PP2 show up with large amplitude due to their particle motion polarized at the same direction as the geophone z. Then, at 31 SS2 is showed split into two delayed from each other in time. Close to 1.20 s there is the converted-wave from the second interface, PS2. Panel 32 has no energy in it due to the alignment between the survey and the fractures.

Consider rotation clockwise of the survey in 45°, where receivers at 180 m offset are presented in Figure 3.26 (a). Panels 31, 32 and 33 present converted P- to S-waves. Same events showed at Figure 3.25 are present in Figure 3.26, but now receivers are not lined up with fractures anymore. Due to this non-alignment, one can see energy at the panel 32, which would be horizontal sensor polarized y direction. That only happens when there is anisotropy caused by vertical or tilted alignment or fractures.
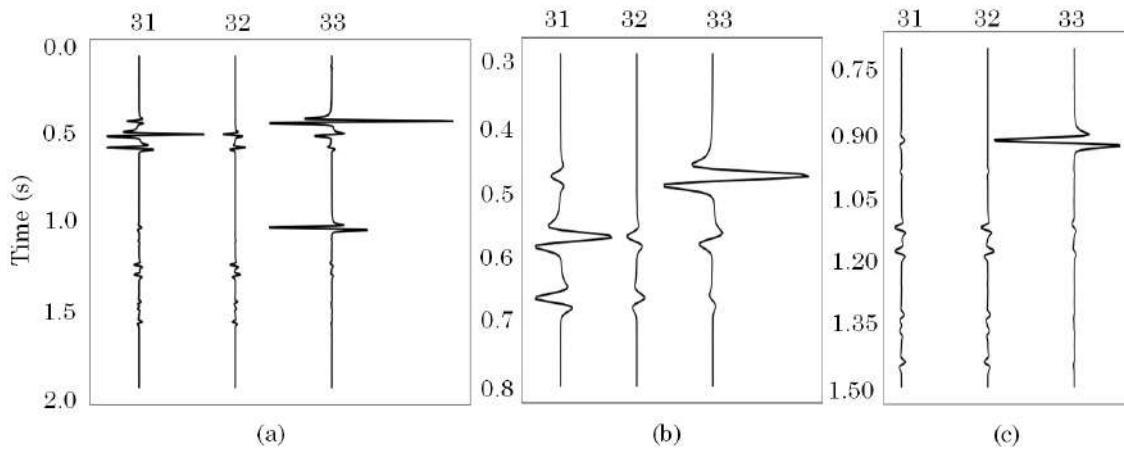
Figure 3.26: Traces 31, 32 and 33. Survey is 45° with fractures.

Figure 3.26 (b) shows first interface reflections and Figure 3.26 (c) shows second interface reflections. Notice C-wave P- to S-wave splitting for the second layer (PS2) between 1.05 s and 1.20 s at the panels 31 and 32 in (c). That did not happen for the survey lined up with fractures (0° with fractures, Figure 3.25).

Figure 3.27 (a) shows panels 31, 32 and 33 for receivers in the survey making 90° with fractures. Figure 3.27 (b) shows first interface reflections and Figure 3.27 (c) shows second interface reflections.

The only noticeable differences between survey at 0° and 90° are possible positive/negative polarization changes and that PS2 arrives first for the 90° alignment. As S and PS waves have shown indicatives of azimuthal anisotropy, it might be interesting to investigate their efficiency in pointing directions of fractures by performing hodogram analysis

Hodogram Analysis

51
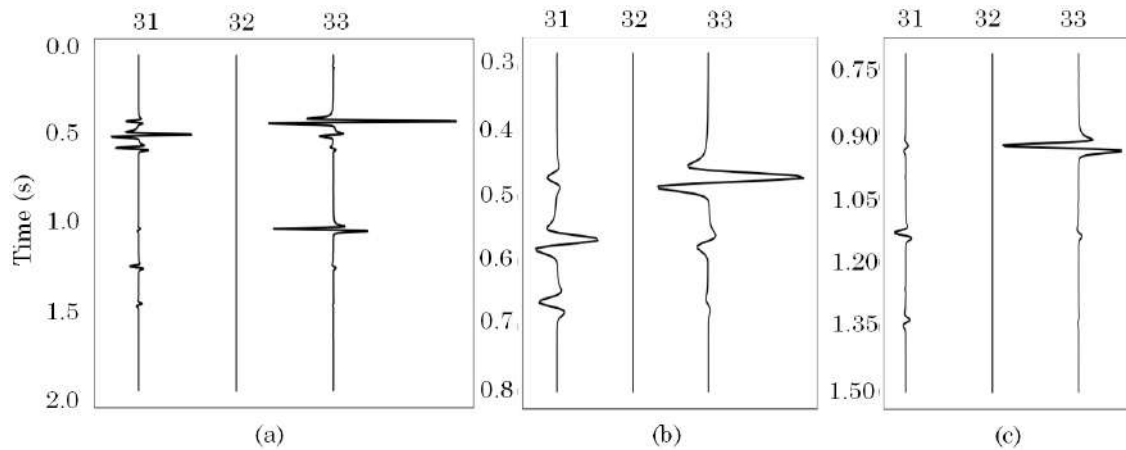
Figure 3.27: Traces 31, 32 and 33. Survey is 90° with fractures.

Particle motion diagrams, also known as hodograms, are plotted to show the direction of the particle motion. Assuming that the data has not many multiples and a good vertical resolution, they may be helpful to identify the main direction of fractures.

Although variation of velocity with direction is certainly characteristic of seismic propagation in anisotropic media, shear-wave splitting (or the generalized three-dimensional coupling of surface-wave motion), easily identifiable in particle-motion diagrams (hodograms), is highly diagnostic of some form of effective anisotropy.

Hodograms for 11 versus 22 panels at each 10° interval from $\theta = 0°$ to 180° are presented in Figure 3.28 including $\theta = 45°$ and $\theta = 135°$. Vertical axis is y and horizontal axis is x particle motion. The darkest event is the S-wave reflection at the first interface, SS1. The lighter event has lower amplitude and represents the S-wave from the second interface, SS2.

There is a slight change in particle motion for any angle for SS1 but it is still noticeable that the particle motion varies with fractures. In other words, just by touching the fractured layer the S-waves align with the main axes of symmetry in the medium below. SS2 directions change considerably and they are showed in Figure 3.29.

In Figure 3.29 S-waves split into two modes, one is faster and the other is slower, then, again there is a darkest event, which arrives earlier S_1, and the slight event S_2 (subscript indicates the arrival time order). When survey is 0° aligned with fractures, the event that arrives earlier is pointing vertically at the hodogram, while the other points horizontally. Comparing this hodogram to the rose wind presented in Figure 3.10 one will notice that those are exactly confirming the model, fractures aligned with y direction, so the faster S-wave arrives pointing to y axis.
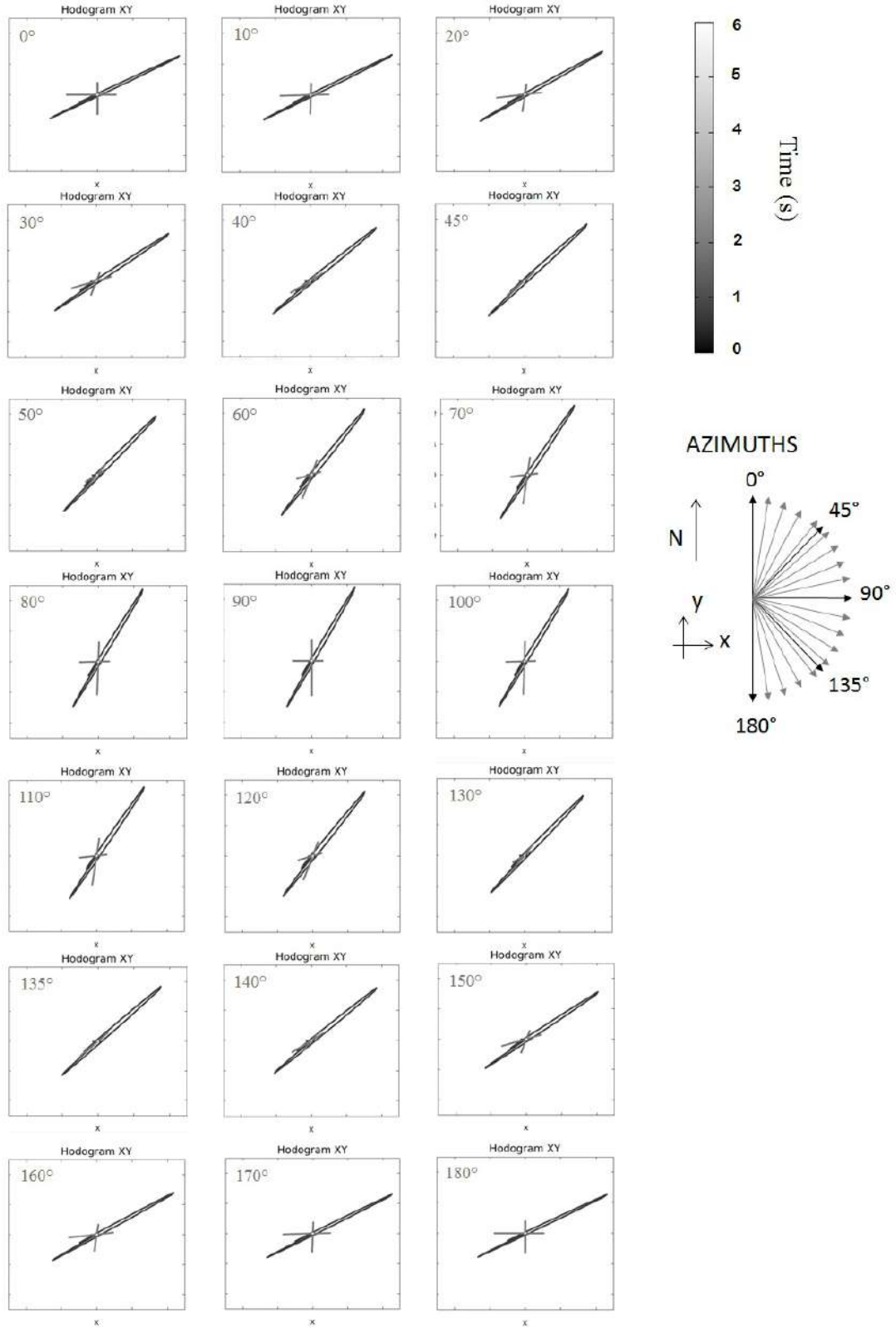
Figure 3.28: Full azimuth XY hodograms.

From the last assertion, we can see that S_1 will show exactly the direction of fractures in the medium. When we align the survey at 30° we see S_1 pointing to 30° at the hodogram and the same happens and analogously to all other angles, S_1 polarization
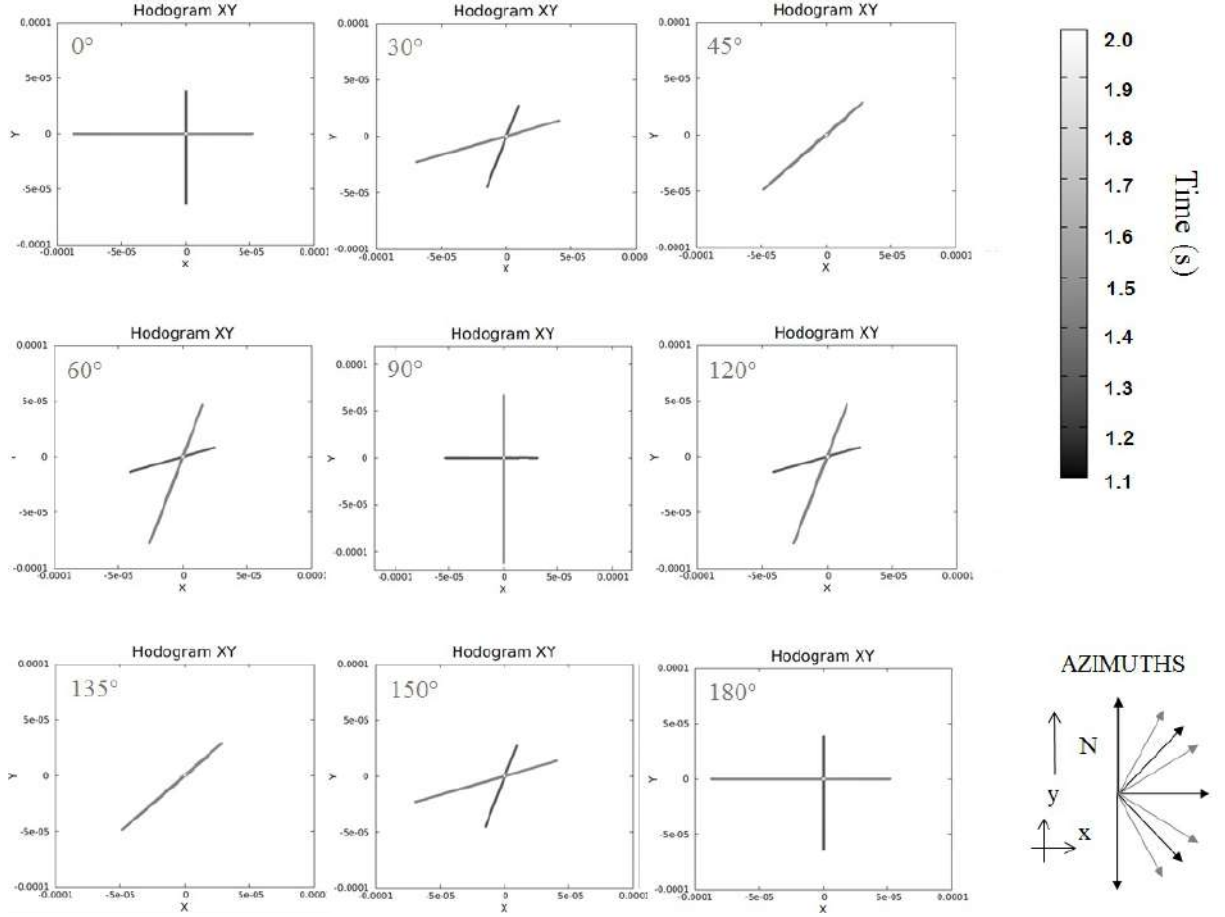
Figure 3.29: Full azimuth XY hodograms windowed for the SS event from the second interface.

helps to find out the direction of the set of fractures.

Considering the panels that are able to show information about the C-wave P- to S-wave, Figure 3.30 shows hodograms for them: 31 versus 32 panels at each 10° from $\theta = 0°$ to 180° including $\theta = 45°$ and $\theta = 135°$.

The darker event in Figure 3.30 shows the converted-wave P- to S-wave at the first interface. It looks like its direction changes slightly with azimuth, and it is different at each quadrant of the rose wind (pointing up or down). The lighter events are converted-wave from the second interface, which split into two with different directions. If we window the data for them, we will have Figure 3.31.

Those converted-waves clearly present changes in their direction with the azimuth with fractures. The faster C-wave (the darkest), let us call it PS_1, points to the azimuth with fractures, as S_1 does in Figure 3.29.

Some elements listed below arise by observing Figures 3.28, 3.29, 3.30 and 3.31.

- Notice that S_1 events do not split into two with time delay in Figure 3.28, but
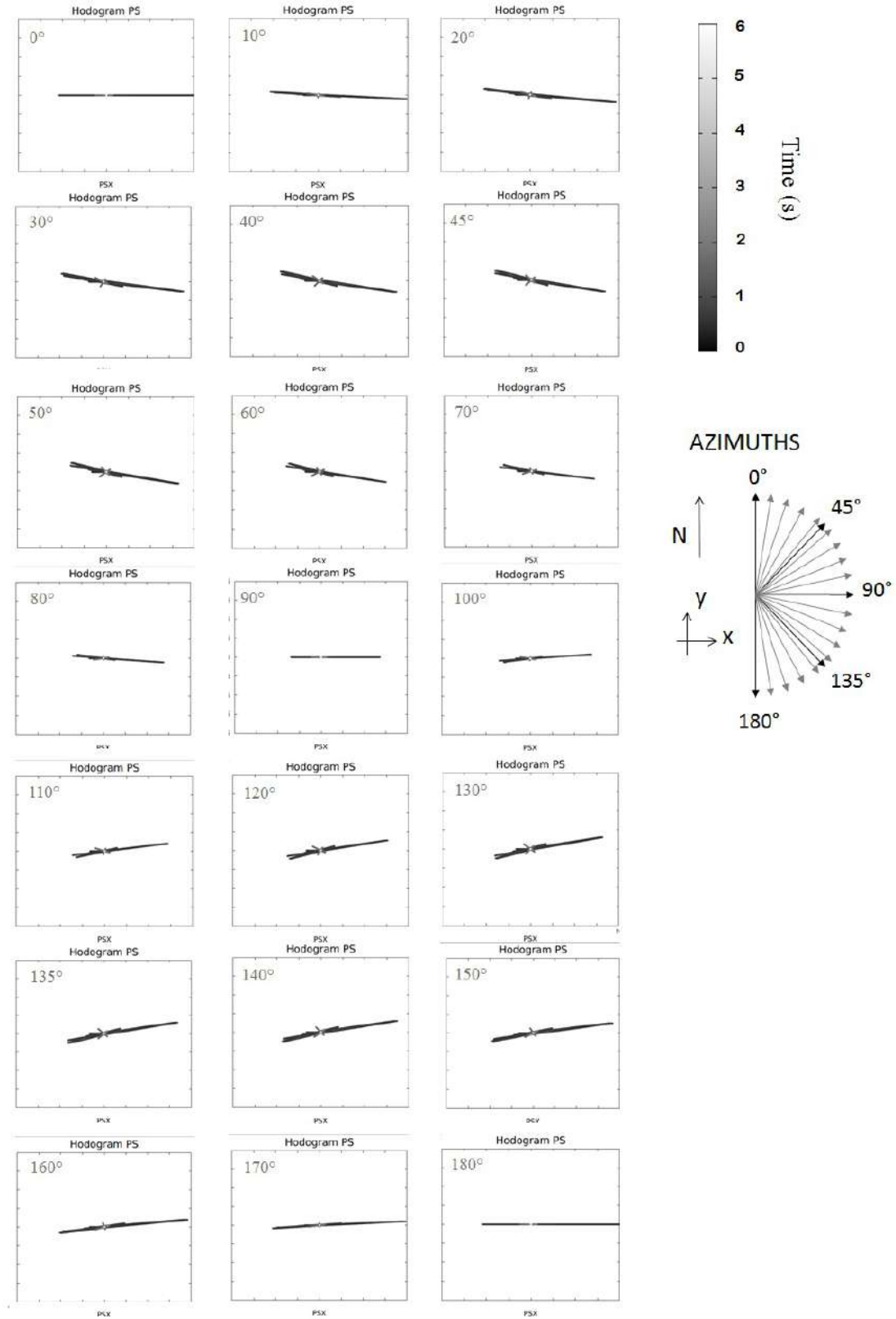
Figure 3.30: Full azimuth hodograms zx *vs* zy (panel 31 *vs* panel 32).

they polarize in the main axis of symmetry in the medium just by touching the surface of the fractured layer.
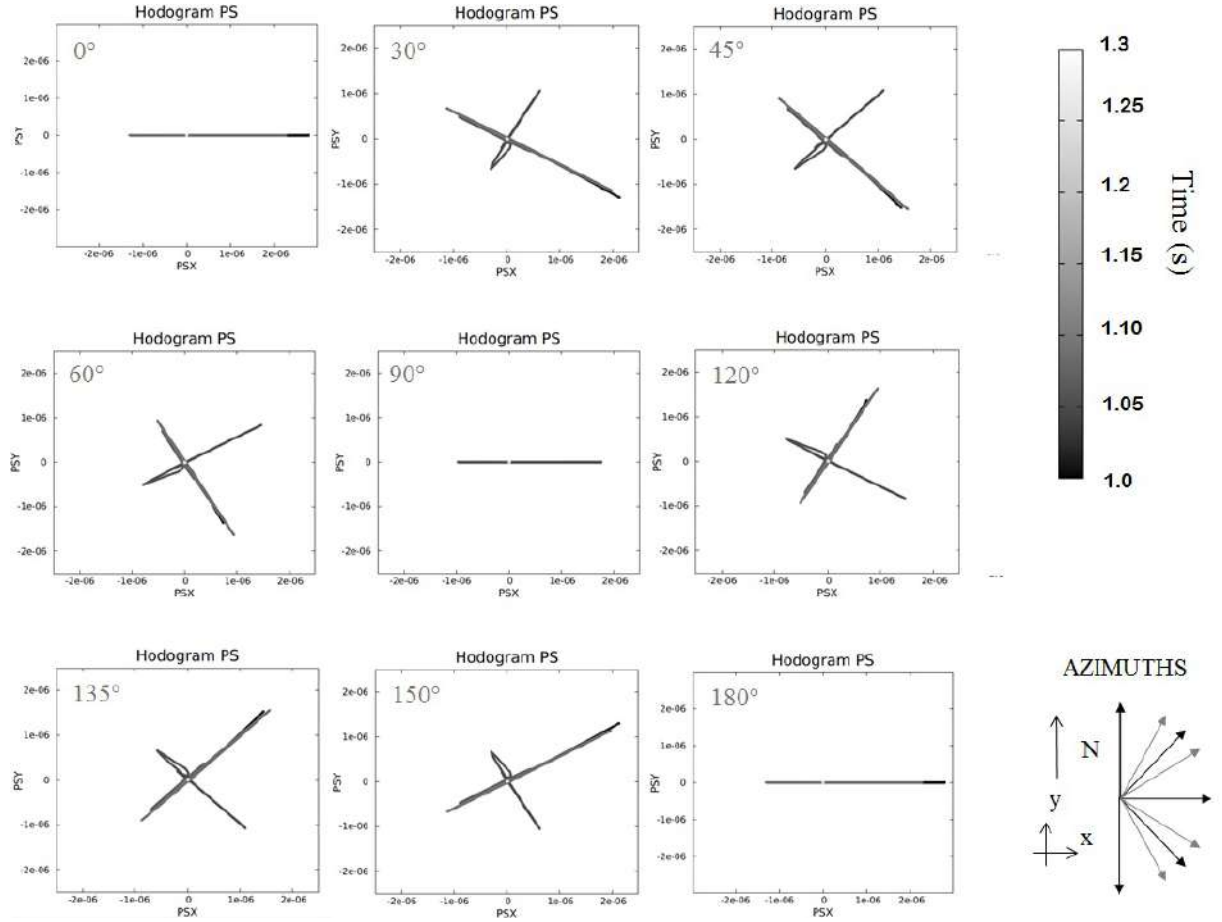
Figure 3.31: Full azimuth hodograms zx *vs* zy (panel 31 *vs* panel 32) windowed for events from the secondinterface.

- S-waves split into two and the faster is lined up with fractures.

- C-waves of nature PS do split into two C-waves and the faster is lined up with fractures.

3.5   Conclusions

This chapter proposed the modeling of anisotropic layers due to vertical fractures. Anisotropic coefficients were computed for a vertically fractured model from a pseudo orthorhombic medium. Multicomponent data were modeled for isotropic and orthorhombic medium via the Reflectivity Method program *anisinpausp*. Synthetic isotropic and anisotropic data showed that the algorithm is successful and robust by providing features of both S and PS waves. S-waves show features such as polarity asymmetry around the source, and changes in polarity and phase after the P-wave critical angle for any of the models.

Besides, shear and converted P- to S-waves showed birefringence when the geophones in the survey are not aligned to the main axes of symmetry in the medium when it comes to orthorhombic anisotropy. S_V- to S_H-wave energy appears in the survey as the angle increases with the direction of the vertical sets of fractures (from 0° to 90°). At 0° and 90° there is no conversion from S_V- to S_H. Therefore, when at 0°, only fast S-wave appear at panel 22 and at 90° only slow S-wave is observed at the panel 11. Converted P- to S-waves show features like S-waves do, such as the absence of energy at zero offset, polarity asymmetry around the source, and also changes in polarity and phase after P-waves critical angle.

To conclude, both shear and converted P- to S-waves presented anisotropy features. In addition, the hodogram analysis pointed to certain directions on faster S-wave. However, althought we can detect the presence of anisotropy, only by the hodogram analysis it is not possible to measure the anisotropic of the medium. Complementary anisotropy analysis should then be carried on to confidently estimate directions and degree of anisotropy. Those analysis are proposed in this work in Chapter 5.

Chapter 4

The Ultrasonic Water-bottom Physical Modeling Experiment

4.1   Summary

This chapter presents the results of a water-bottom ultrasonic modeling experiment undertaken at the Allied Geophysical Laboratory (AGL) in the University of Houston. It reports the acquisition, processing of compressional and converted-waves and the analysis of multi-offset seismic data. 4C ultrasonic physical scaled modelling seismic surveys were conducted to simulate the Ocean Bottom Nodes (OBN) method and to study converted waves from the water-bottom. The model is composed of a carbonatic rock layer with a semi-ellipsoidal anomaly carved at its bottom, to emulate a dome structure or an anticline usually associated with petroleum reservoirs. The carbonatic rock layer is detected and imaged with OBN data converted waves. In addition, carbonate rock properties are measured; P- and S-wave velocities behavior with water saturation, density, bulk, and shear modulus, Vp/Vs and Poisson's ratio, and we estimate the effective porosity (21%) by the fluid saturation in the rock; reflection and transmission coefficients for the model interfaces are studied. The resulting processed data clearly exhibit the caved dome anomaly at the carbonatic rock bottom interface. Furthermore, anisotropy evidences were found at the PS water bottom data, which are going to be investigated in detail in specifically designed 2C experiments which will be later presented. Those results support the idea that converted-waves are suitable for imaging and work in partnership with compressional waves to improve results and optimize the exploration. To our knowledge, this is the first controlled laboratory experiment on OBN and carbonates in the ultrasonic frequency range.

4.2   Introduction

To conduct this part of the research the author stayed for six months (from June to December of 2017) at the University of Houston, Texas, as a Research Scholar under the supervision of Dr. Robert Ronald Stewart and Dr. Nikolay Dyaur[1] . The experiment and simulations were undertaken at the Allied Geophysical Laboratory, a dedicated facility for Geoscience research and training within the Department of Earth and Atmospheric Sciences at the University of Houston.

The goal of the author in going abroad was to join people with know-how concerning to multicomponent seismic and anisotropy applied to petroleum search, mainly water-bottom data, and find out how to deal with this type of data in practice. Time in Houston provided with great talks, courses with the Society of Exploration Geophysicists, and excellent meetings with the AGL group. All that combined with planning the survey, executing and processing the data helped the author to achieve the goals.

The author had already performed computational modeling of multicomponent seismic surveys for isotropic and anisotropic medium. But features that usually appear in a seismic survey in the physical world are not all present in computational modelings due to its approximation with the reality through mathematical models and assumptions made to make it possible. A survey project like this in the real world would cost hundreds of thousands of dollars. On the other hand, to get permission to use public real data from an Ocean Bottom Nodes survey in a thesis takes too long in Brazil, when it is possible.

Besides that, planning a survey can improve a Geophysicist knowledge and experience. The latter is important in order to prevent the researcher from learning from his mistakes during a real seismic survey. That was a great opportunity to deal with planning and performing the survey, processing the data with an anomaly as in real world and still have the multicomponent data to play with other physical properties and features in the end.

Dr. Stewart proposed the OBN experiment to the author, therefore she would be able to have this whole experience and data with real features and lower costs to play with. Experiment planning and execution were performed in about five and a half months. Data was pre-processed by the author in a week to be presented as a final Multicomponent project in Houston by December, 2015. Improved processing was obtained months later in Brazil.

---

[1]Faculty, Research Scientist at University of Houston.

The major difficulty faced by the author in this chapter was concerning to find the appropriate software for processing. Free softwares are usually not appropriate to process neither converted-waves nor water-bottom data. The first idea when Dr. Stewart first proposed the experiment was to use an anisotropic material as the model.

We have tested many materials looking for anisotropy but none of them could cause high S-wave splitting that would be readable and separable in the data. We ended up giving up about the anisotropy and choosing the carbonate layer that was certainly heterogeneous but we did not expect it to be anisotropic, what was found later in the data.

This chapter presents a water-bottom ultrasonic modeling experiment, which includes acquisition, processing of compressional (P) and converted-waves (C-waves) and analysis of multi-offset seismic data. 4C ultrasonic physical modelling seismic surveys were conducted to simulate the OBN method and study converted waves from the water-bottom. The experiment is 1:10,000 scale in space, time and frequency.

A carbonatic rock layer is employed as the model to be imaged and a semi-ellipsoidal anomaly is carved at the bottom to emulate a dome structure or an anticline that is imaged with P- and C-waves. The model, which dimensions are presented in the experimental set-up, is placed under the fresh water in a tank at the AGL. Three component (3C) transducers and a spherical hydrophone are used to build the four-component sensor. In the 3C transducer, there are one vertical and two horizontal (inline and crossline) sensors simulating a 3C geophone; and the spheric sensor simulates a hydrophone.

A carbonatic rock layer is detected and imaged with OBN data converted waves. Carbonate rock properties as compressional and shear-wave velocities are measured; the median connected porosity for the model's carbonate is estimated through rock fluid saturation; reflection and transmission coefficients for the model interfaces are studied to choose a good material as the model and make sure we will have good amplitudes for the reflections.

Instead of performing or showing anisotropic seismic processing, the main objectives in this chapter are to learn to design and execute the survey, to perform a simple processing and to look for features to show the power of C-waves. Among the goals of this chapter there are:

- to perform an ultrasonic water-bottom experiment scaled in space, time and frequency;

- to obtain water-bottom multicomponent;

- to process the data and

- to understand the seismic response of converted-waves from the water-bottom.

The aforementioned understanding of converted-waves is important in a way that one can get additional and supplementary information from the overburden, as for anisotropic attributes such as symmetry axes in the medium and time delay between two shear-waves, known as S-wave splitting, caused by anisotropy.

Though there might exist other water bottom experiments, this is the first controlled laboratory experiment on OBN and carbonate in the ultrasonic frequency range. The ultrasonic water bottom experiment was thought to be the first step to successful start a sub-sea laboratory in the AGL facilities.

4.3   Preliminary investigations

The first stage of this study was the choice of the material that would be used for the experimental model. The author's will was to find a material preferably with azimuthal anisotropy (horizontal axis of symmetry), to image in and look for some C-wave features from water-bottom data.

Among tested models were two plexiglass layers, one filled by dry penny-shaped cracks and the other was fractured by laser to emulate an anisotropic effective-medium. After taking some shear wave velocity measurements, we realized that the fractured plexiglass models did not show a strong S-wave splitting. There was also a sandstone that presented vertical symmetry axis by fine layering and that was not the type of anisotropy we were looking for.

Options remained were models made of a flexible material that would not work well for shear wave recording; an isotropic plexiglass layer; and a carbonate layer without any information about its origin. There was not much time for the student to stay in Houston, so there was no possibility to buy or build an azimuthal layer from scratch to use. We decided to take tests with the last two layers and use the model that presents suitable physical features. The carbonate rock is a piece of sandstone that has been in the AGL for years and had never been used for experiments before. We are not sure, but it is probably from Mexico. Later on the research the carbonate showed azimuthal anisotropy.

To have enough coupling for horizontal components in the water several fluids

were tested. Among them, honey, lipstick, eye brown, a tar based material, etc. After several tests, we opted to cover the surface of the model with a tar based material coat of 0.2-0.3 mm and that would not dry in water, keeping (from our practice) high viscous coupling properties on the horizontal and vertical receivers for more than two months.

Dr. Nikolay Dyaur helped to build parts of the experiment or advising on how to work to prepare and take the experiment. He built two holders and the 4C sensor. One of the holders was to grip the sensor (Figure 4.1 (a)) that touches the rock and moves 2.5 mm each shot, and the other would grip the spherical source (Figure 4.1 (b)) just below the water surface, as in a sea-bottom marine survey. Its size is large when converted to real-world dimensions, so we consider its center to be 70 m depth.

Figure 4.1: (a) multicomponent sensor and (b) spherical source.

Meanwhile, we started to prepare the pool for the experiment. The pool was out of use for a long time, so it had to be cleaned and filed with water. The pool has transparent glass windows on two of its four walls so that we could follow the automated source and receiver positioning and take pictures during experiments. They are shown in section 4.5.

A Labview software [2] was used for commanding holder movements carrying the source and touching receivers in the pool, as many centimeters as we needed. Then we put the carbonate rock layer under water for saturation during several days and started the ultrasonic water-bottom simulations when it was ready.

4.3.1 Rock Properties Measurements

Before the acquisition took place the carbonate layer was immersed in the water for a month. In the first stage, the water surface reached only half of thickness of the layer. Only after the surface of the carbonate layer became wet we increased the

---

[2]Labview software was coded years before by Anoop William former Staff and Dr. Robert Willey Researcher at the University of Houston.

level of water to experimental condition. The water saturation of the porous rock was completed in two weeks due to porosity and capillary pressure.

To predict elastic properties of the layer after being immersed a long time in water, we studied the changes in compressional-wave velocity V_P and shear-wave velocity V_S during saturation. For the rock properties measurements in this work, a sample of the carbonate layer was extracted before building the model (Figure 4.2). Weight and velocity of compressional and shear waves were measured in the sample and rock density and connected porosity were computed. Figure 4.3 shows pictures of other carbonate samples from different perspectives. A one cent coin is on the saide for dimensions comparison.

Figure 4.2: Carbonate sample for rock properties study.

Figure 4.3: Pictures of the carbonate sample.

One of the samples was put in a vacuum machine for saturation while its properties were measured in steps of water saturation. Velocity was measured with ultrasonic transducers (500 kHz peak frequency) and its mass was measured from dry to fully saturation in a precision weighing scale, therefore, relations between velocity, density and water saturation could be established. Figure 4.4 shows V_P (a) and V_S (b) decreasing with water saturation assuming values of 4.032 km/s and 2.055 km/s for P- and S-wave, respectively, for full saturation. The sample is considered to be

zero saturation under laboratory conditions (24°C and sea level pressure). On the other hand, a hundred percent saturation indicates that all connected pores in the sample were filled with water. That is the effective porosity.
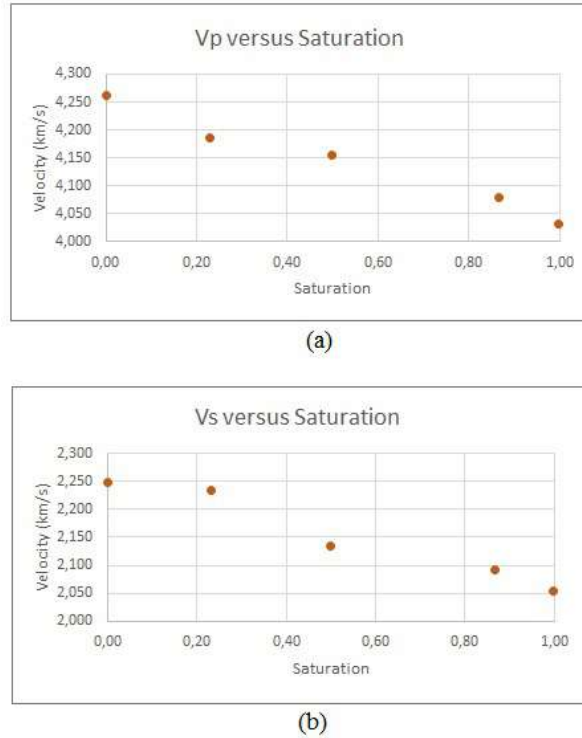
Figure 4.4: Velocities varying with water saturation during rock properties measurements in the carbonatic rock sample: (a) P-wave velocity and (b) S-wave velocity.

Figure 4.4 shows saturation, V_P (a) and V_S (b) decreasing with water saturation. While V_S decreases with saturation due to its inverse dependence on density, V_P should increase due to its stronger dependence on the bulk modulus rather than on density only. The influence of pore fluid saturation on the P-wave velocity of rocks cannot be separated completely from its matrix features or pore geometry. However, several factors influence or dominate the effects of fluid on wave velocities. Among them are fluid compressibility, fluid density, microcracks in cement, and chemical interactions between the fluid and solid materials around grain contacts.

Besides that, saturating the limestone may be softening it via dissolution, chemical action on the cracks and contacts. This could cause lower P and S velocities. The influence that each factor has on a given rock is often quantitatively unpredictable. However, they do exist together and we cannot predict it through ultrasonic data only. Therefore, we had to take direct measurements to have the integral changes in velocity.

According to Biot (1956[76] and 1956[77]), there is a relative motion between the fluid and the solid frame due to inertial effects for high frequencies of wave propa-

gation, so that the fluid and solid are essentially decoupled. It might be a reasonable explanation for the difference in velocities behaviors in the ultrasonic experiment. Fabricius *et al.* (2008)[78], who have shown in some carbonates compressional sonic velocities decreasing with water saturation, found results that are similar to ours.

The fact that P-wave velocity is not behaving as expected for seismic waves gives a hint that it could be due to the frequency range that is being worked with. Biot (1956[76] and 1956[77]) developed a theory of wave propagation in fluid saturated porous media that focus on macroscopic fluid-flow (fully discussed by Johnson, 1986[79]). According to that theory, there is a relative motion between fluid and the solid frame due to inertial effects during acoustic wave propagation. It shows that at high frequencies, the fluid and solid are essentially decoupled. Therefore seismic waves are almost always in the low-frequency range of Biot's theory. Its low-frequency limit yields the well-known Gassmann's equations (GASSMANN, (1951)[80]).

The author's results attest to his theory, where ultrasonic laboratory measurements were being affected by mechanisms operating at different frequency range and they may not be entirely representative of velocities at seismic frequencies. But that is not a big deal since we are not willing to look for the exact seismic velocities but working with ultrasonic data. See graphs on Appendix B.

Table 4.1 shows V_P, V_S, shear modulus μ, bulk modulus K and rock density ρ, Poisson's ratio σ, varying with water saturation Sat, in a carbonate sample. Saturation increases from 0 to 100% from table top to bottom.

Table 4.1: Rock properties varying with the water saturation in the carbonatic rock.

Sat (%)	V_P (km/s)	V_S (km/s)	ρ (g/cm^3)	μ (GPa)	K (GPa)	V_P/V_S	σ
0	4.262	2.247	1.97	9.95	22.52	1.89	0.308
23	4.185	2.234	2.02	10.08	21.94	1.87	0.301
50	4.155	2.134	2.08	9.47	23.28	1.94	0.321
87	4.079	2.091	2.15	9.40	23.24	1.95	0.322
100	4.032	2.055	2.18	9.21	23.17	1.96	0.325

Table 4.1 shows shear modulus changes, for carbonate sample from dry to brine saturation, of up to 9% showing to be sensitive to small amounts of moisture or partial water saturation (ASSEFA *et al.*, 2003[81]). Several laboratory studies have also reported μ changes between 5% and 20% from dry to water or brine saturation in carbonates (ASSEFA *et al.*, 2003[81]; BAECHLE *et al.*, 2005[82]; SHARMA *et al.*, 2006[83]). The high Poisson's ratio $\sigma > 0.3$ found in our study is similar to values found by Adam *et al.* (2006)[84]. They propose the use of empirical correlations to correct Poisson's ratio because their objective was to compare measured physical

with modeled properties. In this work, we are not aiming to do that, so we will keep our values since they are in agreement with the literature.

4.3.2   Reflection and Transmission Coefficients Study

Reflection (R) and transmission (T) coefficients indicate how much of the incident energy travels back by reflection and how much travels to the next layer. They are related to the difference in impedance between two media. In order to choose the most suitable material for the experiment in terms of those coefficients, some materials other than carbonate were also studied. In this section, we present the study of the coefficients for the limestone carbonate layer and for the isotropic plexiglass, since others were eliminated in this part of the study.

In the ultrasonic experiment, waves are generated by the source and propagate down the water to the model. At the interfaces water-model and model-water velocities and density change, as well as their products called impedance. At the interface, part of the energy is transmitted down to the next medium and the other part reflects, or echoes, back to the surface.

Two sets of physical equations govern the reflection and transmission of waves. One of them is the Snell's law, which gives the basic geometry of the ray paths. The other are Zoeppritz equations which describe how the incident wave energy encountering an interface becomes partitioned between reflected and transmitted waves. They give angle-dependent reflection and transmission coefficients for elastic plane waves at a non-slip horizontal boundary between two semi-infinite isotropic elastic media.

Aki and Richards (1980)[85] *apud* Stewart (2002)[59] showed that there is an asymmetry in the P-S ray path that is described by Snell's law according to the Equation 4.1

$$\frac{\sin(\theta)}{V_P} = \frac{\sin(\phi)}{V_S} \tag{4.1}$$

where the P-wave angle of incidence and S-wave angle of reflection are given by ϕ and θ, respectively.

Figure 4.5 shows a downward-propagating P-wave converting into an upward-propagating S-wave due to impedance contrast of the layers. Directions of positive phase as shown by arrows. MP is the midpoint between source and reciever for monomode reflection, and CP is the convertion point for bimode P- to S-wave.

Note that CP is shifted towards the receiver Since $V_S < V_P$, ϕ is smaller than θ, so the S-wave raypath is closer to vertical making the pattern seen in Figure 4.5.
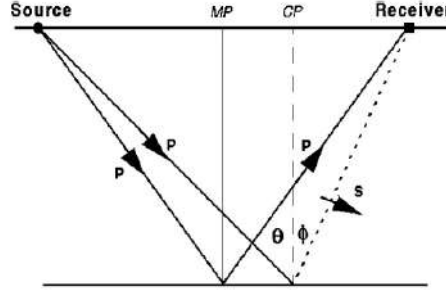
Figure 4.5: Comparison between converted-wave (P-S) reflection at its conversion point (CP) and pure mode P-wave reflection at its midpoint (MP)

When either a P-wave or S-wave is traveling through different materials, it will run into boundaries. At this point it may be reflected as either a P-wave or S-wave, or it may be transmitted through the boundary as a P- or S-wave with changes in direction. Normally it is split up into a combination of these kinds of outgoing waves, and the magnitudes of the coefficients calculated from the Zoeppritz equations show the relative amplitudes of the waves produced by each of these four possibilities.

Thus, the energy partition at the interface is governed by reflection (Equation 4.2) and transmission (Equation 4.3) coefficients, which depend on the impedance contrast across the interface and the incidence angle of the incident wave. Considering the simple case of normal incidence for P-wave:

$$R = \frac{A_R}{A_i} = \frac{\rho_2 V_2 - \rho_1 V_1}{\rho_2 V_2 + \rho_1 V_1} \tag{4.2}$$

$$T = \frac{A_r}{A_i} = 1 - R \tag{4.3}$$

where ρ_1 is density in the incidence medium, the first, and ρ_2 in the second medium. V_1 and V_2 follow the same idea for compressional velocities.

Coefficients in this section were computed by Crewes Explorer program, a Webpage showed in the references of this work links to CREWES interactive Java Explorers, Plotters, and Calculators. CREWES is an applied geophysical research group concentrating on the acquisition, analysis, and interpretation of multicomponent seismic data. Their plots show how the reflection coefficients change with the angle of incidence. To see how the coefficients change with properties of each medium

one can control a panel to change the density and velocities of each layer. Entries are density, compressional and shear-wave velocities of two media. Output choices are the exact solution of Zoeppritz equations, Aki-Richards approximation (AKI and RICHARDS, 1980[85]) and Bortfeld approximation (BORTFELD, 1961[86]) with the choice of displaying one or both, magnitude and phase.

For choosing the model several materials were tested and in this section the reader will see the comparison for two of them: the plexiglass and the carbonate coefficients. Consider a three-layer model where the first one is water; the second one is the model; and the third one is water, similar to the OBN geometry. The model has two interfaces: water-model and model-water. The notation that will be adopted from now on for each coefficient is a three-letter acronym such as RPP or TPS. The first letter indicates whether it is a reflection (R) or transmission (T) coefficient. The second letter indicates whether the incident wave is P or S. The third letter indicates whether the outgoing wave is P or S.

The magnitudes of the four coefficients RPP, RPS, TPP, and TPS give us an idea of how P-wave energy is distributed when it reaches an interface. The coefficients RSP and TSP give us an idea of how it does for S-wave energy. There is no RSS or TSS since both interfaces are with water: model-water or water-model interfaces. The PP, PS and SP coefficients are shown in Figure 4.6.

Figure 4.6 shows the model scheme for the coefficients study. First interface is water-model, second interface is model-water. Some coefficients are ilustrated in the figure. Parameters used and results for carbonate and plexiglass are shown next.
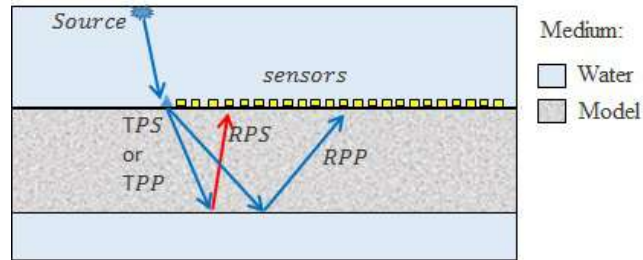
Figure 4.6: Model scheme for the coefficients study.

If there is a high RPP at the water-model interface we might deal with high energy multiples from the water bottom. We are interested in high RPP and RPS at the model-water interface for small to median angles of incidence, to get high amplitude for P-wave and C-wave from the model bottom interface. On the other hand, if there is a high RSP and RPS we might deal with strong energy multiple from mode converted events. We are also interested in low transmission coefficients (TPP and TPS) for the model-water interface, in order not to lose energy at the

model bottom. In addition, converted S- to P-wave coefficients (TSP and RSP) were also investigated at the model-water interface.

Velocities and densities used in the simulations are presented in Table 4.2

Table 4.2: Input for computing the reflection and transmission coefficients.

Medium	V_P (m/s)	V_S (m/s)	ρ (g/cm^3)
Water	1,500	0	1.029
Carbonatic rock	4,032	2,055	2,18
Plexiglass	2,730	1,250	2,018

Results on the Figures 4.7 and 4.8, show vertical axes with magnitude of the coefficients solid line (increasing from -1 to 1) on the left side and phase on the right side in dashed line. The horizontal axis shows the angle of incidence in degrees increasing from 0 to 90° and there is a color legend on the bottom of each panel.

Figure 4.7 shows how the reflection and transmission coefficients change with angle of wave incidence for two interfaces, water-rock (right panel) and rock-water (middle and left panels).
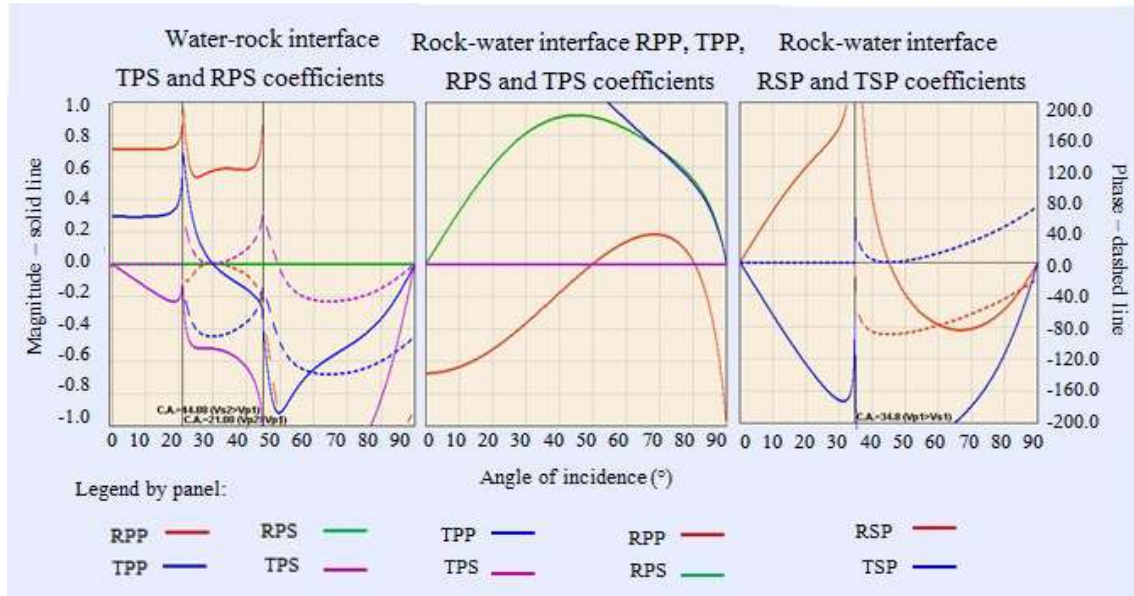
Figure 4.7: Reflection and transmission coefficients for the rock-water and water-rock interfaces. Solid line is magnitude and dashed line is the phase. Legend is showed by panel.

Figure 4.8 shows how the reflection and transmission coefficients change with angle of wave incidence for two interfaces, water-plexiglass (right panel) and plexiglass-water (middle and left panels).

69
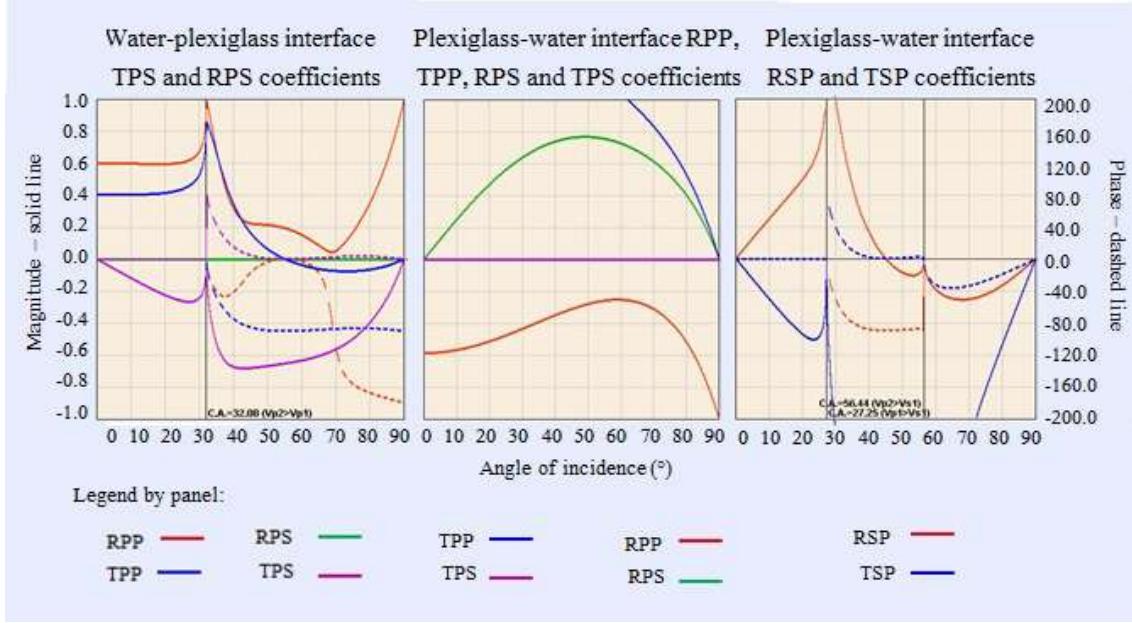
Figure 4.8: Reflection and transmission coefficients for the plexiglass-water and water-plexiglass interfaces. Solid line is magnitude and dashed line is phase. Legend by panel.

- Interface 1 - Though TPS critical angle happens to be lower for the carbonate (22°) than for the plexiglass (33°), TPS is higher for plexiglass than for the rock at the water-model interface. TPS have asymptotic behavior at the water-rock interface while it behaves better for the plexiglass. That means that there is no PS-wave transmitted to the carbonate for angles higher than 40°. RPS is null for both, the water-rock and the water-plexglass interfaces for obvious reasons, S-waves do not propagate in water.

- Interface 2 - TPS is null at the model-water interfaces for the same reason. At the model-water interfaces, TPP exists for higher angles ($\theta \geq 54°$ for rock and $\theta \geq 60°$ for plexiglass), probably due to refraction. RPP is constantly negative and keeps its median amplitude higher for the plexiglass-water interface, while it is higher value for short angles, $0° \leq \theta \geq 30°$, and goes to zero at $\theta=50°$ and 80° becoming positive for the rock-water interface for major values of θ. RPS is positive for short angles inverting the amplitude from $\theta \geq 45°$, showing major magnitudes for the rock-water interface. RSP and TSP have asymptotic behavior at $\theta \geq 35°$ for both model-water interfaces and again at $\theta \geq 60°$ for plexiglass. Anyway, the absolute value of RSP and TSP is higher for the rock model at shorter offsets.

Ultimately, the comparison between the reflection and transmission coefficients of plexiglass and carbonate lead to the decision of using the carbonate as the model. Its real aspect will probably give us a more realistic result concerning to seismic data

from real survey. Furthermore, RPP, RPS and RSP are greater for the carbonatic rock at the model-water interface at shorter angles, what will provide us with good quality data in shorter offsets. As the model is composed by just one layer the target is shalow, therefore, imaging with short offsets is enough.

Next, we perform computational modeling in order to predict features that the ultrasonic water-bottom experiment will present for P-wave and C-wave.

4.4 Computational Modeling

Computational modeling helps to figure out how the data looks like before the survey. Though they are not the same as the real data, by comparison, we can look for similar features in the data during processing steps. Experience in seismic surveys and performing computational modeling reduce costs, predict events and prevent from mistakes usually found in seismic surveys that did not have it, as well imaging the target and perform the event identification.

In this section computational modeling is performed using isotropic simulations on Reflectivity method[3] and Hampsonrusel's software[4] to predict events and patterns.

C-wave positive polarity showed by arrowhead in Figure 4.5 provoke an asymetric pattern around the source as shown in Figure 4.9. This happens due to the particle motion vectorial nature because P-wave do not convert for zero offset reflections. The horizontal channels record particle motion, revealing those features. Several authors have presented analysis of the asymmetric reflection point trajectory (CHUNG and CORRIGAN, 1985[87]; TESSMER and BEHLE, 1988[88]) and its importance in P-S imaging.
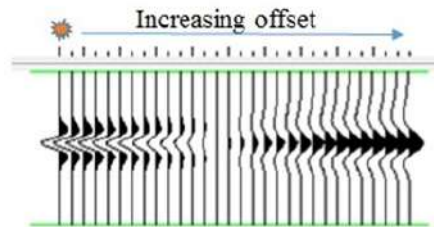
Figure 4.9: NMO corrected PS-wave from Hampsonrussel shows P-wave refraction angle causing lack of amplitude and phase change.

---

[3]See chapter 3 for details on theory and computational code.
[4]Compagnie Générale de Géophysique (CGG) software.

At zero offset there is no vectorial conversion, therefore, in the case of the converted-wave event, there is no amplitude at such offset. Amplitudes increase with offset up to the offset where incidence angle is the P-wave critical angle θ_c. According to (GAISER, 2015[89]) for offsets larger than θ_c, amplitude decrease to zero followed by phase change at longer offsets as showed in Figures 4.7 and 4.8.

Figures 3.3 in chapter 3 is isotropic computational modeling that shows features of monomode P-wave and C-wave reflections. Such features are mentioned below. For monomode P-wave, events are all starting from zero offset, because there is no conversion, they are reflections from P to P-wave.

Converted-wave events do not start from zero offset, due to the non-vectorial conversion at null angle. At a certain offset, there is a lack of amplitude, and that is the P-wave critical offset, where there is the critical angle of incidence. Next there is a change in phase and polarity. That is usually neglected during processing.

Table 4.3: Parameters for each layer in the isotropic model.

Layer	V_P (m/s)	V_S (m/s)	ρ (g/cm³)	V_P/V_S	z (m)
Layer 1	2,000	1,000	2.3	2.0	1,000
Layer 2	2,820	1,480	2.7	1.9	1,000
Layer3	4,000	2,000	3.0	2.0	0

4.4.1 Expected Events

Expected events are showed in Figures 4.10 and 4.11. Figure 4.10 (a) is a direct event, usually called water bottom event (WB). A primary reflection is a seismic wave that propagates in the earth and has one single bounce, upward bounce, in the subsurface. After that single bounce, the wave is measured in the surface. Figure 4.10 (except for (a)) shows primary reflections where (b) is the P-wave reflection, (c) S-wave reflection and (d) converted PS-wave reflection from the carbonate bottom.

On Figure 4.10 (c) and (d) are C-waves. In (c) the conversion happened during transmission, and in (d) it happened during reflection at the carbonate bottom. From here on we will focus on (d) event due to the higher TPP coefficient in comparison with TPS showed in section 4.3.2.

A multiple is a seismic reflection event that has at least one downward bounce. If the bounce is happening at the surface it is a surface related multiple. If the downward bounce is happening at somewhere else in the subsurface it is an internal
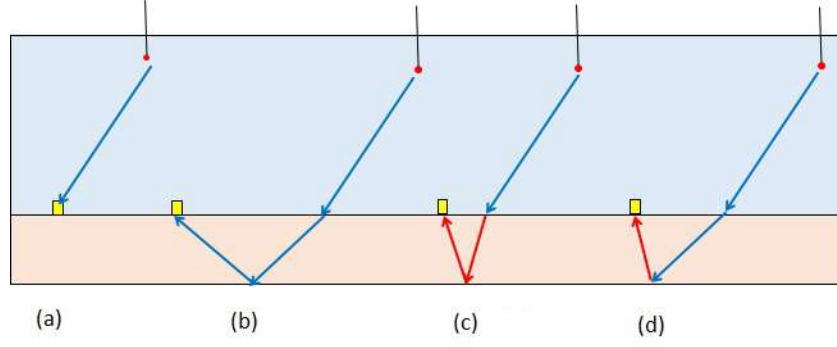
Figure 4.10: Expected events. (a) P-wave water-bottom (direct) arrival (WB), (b) P-wave reflection, (c) S-wave reflection and (d) converted PS-wave reflection from the carbonate bottom.

multiple (BERKHOUT & VERSCHUUR, 2005[90]). Figure 4.11 shows first order multiple events, from water bottom (WBM1) and internal multiple (M1).
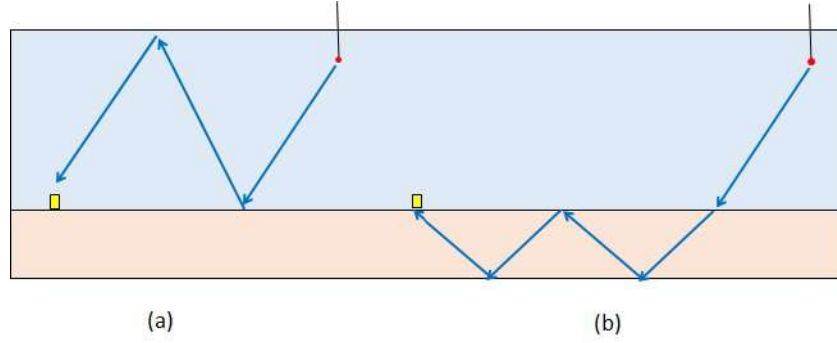
Figure 4.11: Unwanted but expected events: (a) Water-bottom multiple (WBM1), (b) internal multiple (M1).

Higher level multiples are the reverberations that have suffered multiple reflections (more than two) before being recorded. Multiple events will happen for P-waves and for C-waves (converted waves). During processing, multimode multiples will be taken into consideration to attenuate them via filtering or predictive method which are discussed later during processing.

Table 4.4 presents the calculated arrival times for the main events. M1 and M1WB are shown in Figure 4.20. M2, M3, M4, M5, M6 and M7 are internal multiples from events that reflected 3, 4, 5, 6, 7 and 8 times, respectively, inside the carbonate. M2WB and M3WB are water-bottom multiples that reflected at the carbonate surface 3 and 4 times, respectively, before being recorded.

Table 4.5 presents the calculated arrival times for the main events. MC1 and MC1WB are shown in Figure 4.20. MC2, MC3, MC4, MC5, MC6 and MC7 are internal multiples from converted-wave events that reflected 3, 4, 5, 6, 7 and 8 times, respectively, inside the carbonate. MC2WB and MC3WB are water-bottom

Table 4.4: Computed arrival time for the main events at vertical channel.

Event	T_0 (ms)
WB	641
P-wave	932
M1	1,221
M2	1,511
M1WB	1,924
M3	1,947
M4	2,237
M5	2,527
M6	2,817
M7	3,107
M2WB	3,206
M3WB	4,489

multiples converted-waves that reflected at the carbonate surface 3 and 4 times, respectively, before being recorded.

Table 4.5: Computed arrival time for the main events at inline channel.

Event	T_0 (ms)
WB	641
C-wave	1,072
MC1	1,221
MC2	1,511
MC3	1,652
MC4	1,845
M1WB	1,924
MC5	2,038
MC6	2,231
MC7	2,424
M2WB	3,206
M3WB	4,489

By looking at Tables 4.5 and 4.4 it is clear that the target is shallow and not strongly affected by the water bottom multiples and that it might be affected by some of the internal multiples during the processing.

In this section the computational modeling helped to identify features in the C-wave data, to predict events that are expected to be in vertical and horizontal channels. This sections helps to plan the survey and processing the data. Its results will be used for the following sections.

4.5 Experimental Set-up

Through the design for the OBN survey the author's goal was to learn how to design a seismic survey, getting experience and acquire good quality multicomponent data, namely converted-waves, for further investigations.

The model is a carbonatic rock layer with an semi-ellipsoidal anomaly, showed in Figure 4.12 carved at the bottom to emulate a dome or an anticline. Simulations were run with the model top surface under 100 mm fresh water layer in a pool. Cave dimensions can be seen in Figure 4.13.

Figure 4.12: Sculpted cave in the carbonate layer.

a=33.0 mm, b=50.0 mm and c=17.5 mm
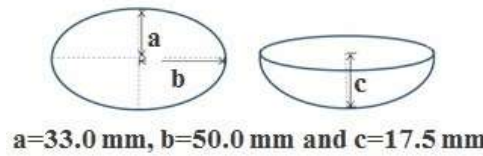
Figure 4.13: Cave dimensions.

Pool dimensions are 3.85 m x 1.82 m x 1.5 m size. Figure 4.14 (a) shows the scheme of the pool top view and distances from the pool wall to the model edges. The model is centered in the pool. Figure 4.14 (b) shows the model laid down with the piece of carbonate turned down over a steel table for z positioning with water layer over the rock surface. Figure 4.14 (c) shows details of the wood spacer placed under the rock with 1.2 cm to keep water under the model and the rough surface placed 1.2 cm below the rock bottom to spread the incident energy. This was because we were not willing to record energy that is transmitted down the carbonatic layer.

Figure 4.15 shows details of the scheme for the shot and receiver line, model

The pool top view

Y pool

The pool

X1

Y1   Model   Y2   X pool

X2

(a)

The pool side view

Y pool   (b)

The pool

Side B   table   Model   Rough surface

Z table   Side A

X pool

Z pool

The table side view

Model

Z Model=58.5 mm

Z wedge   Z Rough surface

Z table   wedge

Rough surface

(c)
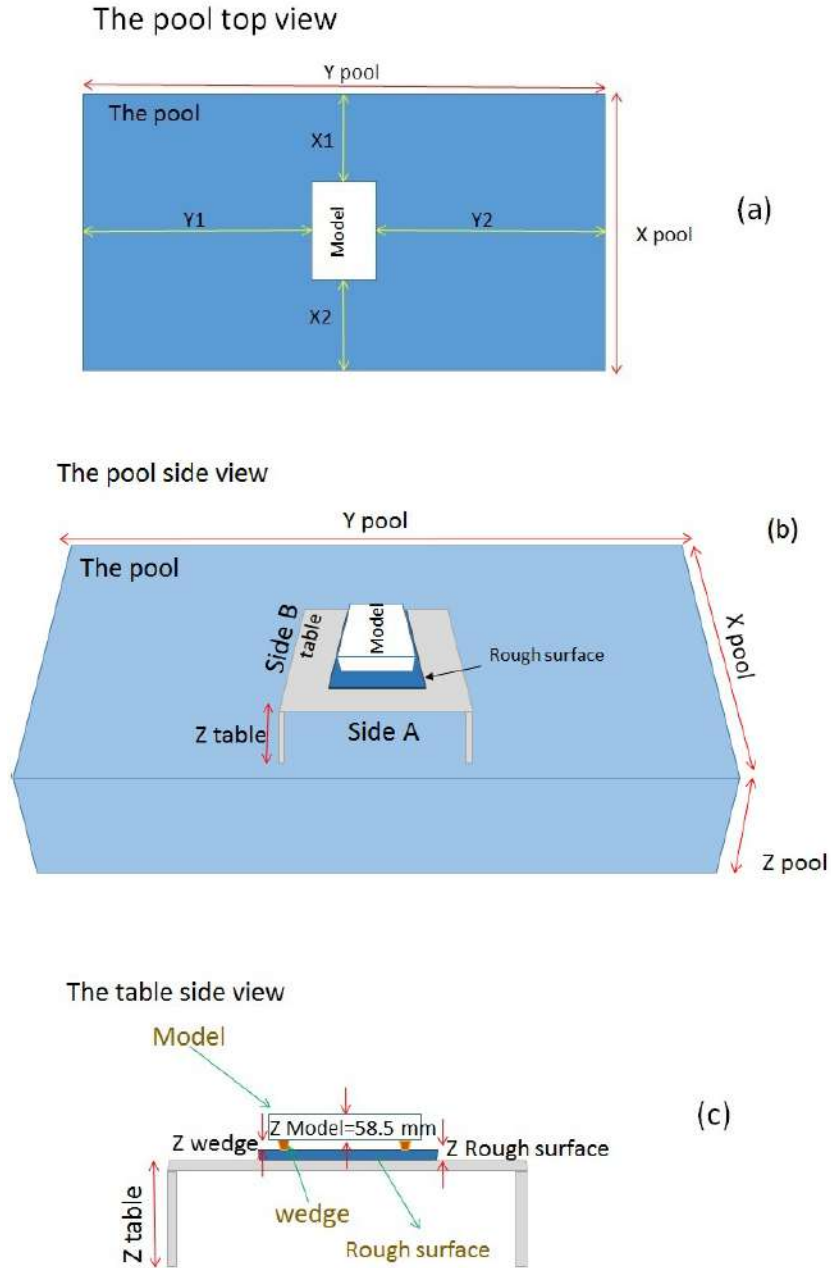
Figure 4.14: (a) pool top view, (b) side view and (c) table dimensions and the experiment components.

and reference coordinate system. Compare side A (a) and side B (b) with Figure 4.14 (b).

Table 4.6 show dimensions in Figures 4.14 and 4.15.

To record good amplitude signal one must have a good coupling between the receiver and the model. Under those circumstances, a sample was cut off the carbonate layer to be used in a series of coupling tests. That sample was named as sample carbonate layer 3 (CL3). For these coupling tests with CL3 we used P-

76
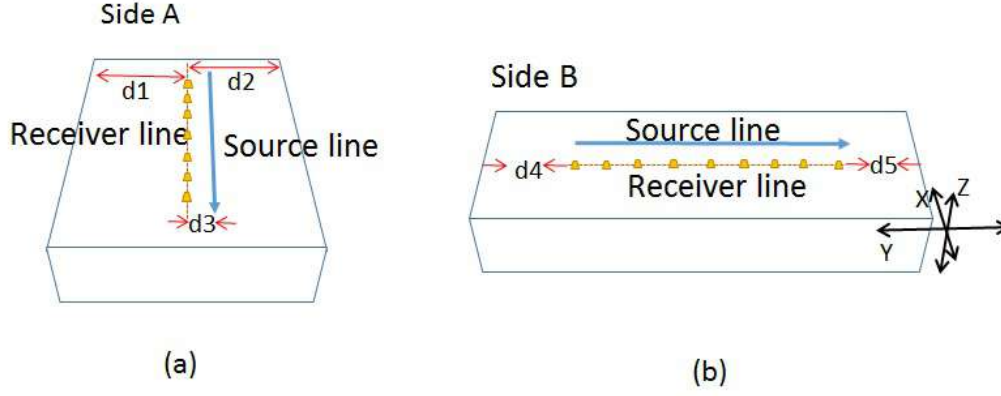
Figure 4.15: Pool top view, side view and the dimensions in the experiment.

Table 4.6: Experiment dimentions.

	Dimention	Length [mm]	Description
Pool Size	X_{pool}	1820	Pool size in x direction
	$Y_{pool}l$	3850	Pool size in y direction
	Z_{pool}	1500	Pool size in z direction
Distances from model to pool edges	X_1	620	Model offset to pool wall in x direction
	X_2	560	Other model offset to pool wall in x direction
	Y_1	1790	Model offset to pool wall in y direction
	Y_2	1610	Other model offset to pool wall in y direction
	H_{table}	600	Table height
Model Dimentions	H_{wedge}	12	Wedge height
	T_{rough}	52	Thickness of rough surface
	T_{steel}	9.4	Steel table thickness
	$T_{carbonate}$	58.5	Carbonate layer thickness
	d_1, d_2	210	Receiver line offsets from the major model edges
	d_3	0	Shot line offset to reciever line
	d_4, d_5	105	Reciever line offsets to minor model edges

and S-transducers with central frequency of 500 kHz. Some of the tested coupling materials were: water, honey, eyelash mask, asphalt paint, lipstick, among others. After the first measurements and coupling tests the asphalt paint proved to be the best S-wave coupling, so it was chosen to cover the whole model surface.

The next step was to set-up the experiment. With the top surface covered by the asphalt painting the model was placed 12 mm over the rough surface (by using wood spacers) (Figure 4.15 (b) and (c)). Then the whole set was placed 100 mm under the water (see water level in Figure 4.16 (a)).

Figure 4.16 (a) shows the side view scheme with the source and receiver positions. The source was placed just under the water surface. The receiver hold has two supporting points forming a triangle and a spring to make a better coupling on the paint over the model. The receiver was stationed at one of the 80 stations over
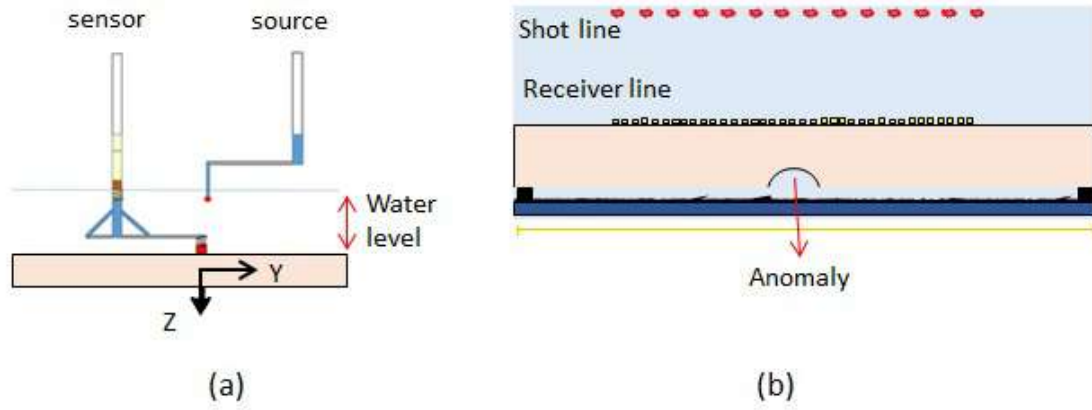
Figure 4.16: Acquisition scheme: (a) sensor and source holders and (b) shot and receiver lines over the model.

the carbonate surface (Figure 4.16 (b)) at the time .

There is only one 4C sensor that moves over all stations each shot to build a receiver gather. The source moves 161 times for each of the 80 sensor stations, changing its position 12,880 times. Each trace was composed by 30 source pops stacked for good signal to noise ratio. In the end, almost four hundred thousand shots were done to produce the final data (not counting previous tests). The receiver holder moves precision wise in the x direction after each shot commanded by a Labview code in the master computer. The source holder is able to move in the x direction to perform the shot line with 161 shots.

The sensor holder grips a 4C receiver which is composed by three component transducers (the vertical and two horizontal, inline and crossline), simulating a 3C geophone; and a spherical hydrophone as in Figure 4.16. The experiment was performed in the ultrasonic frequency range. The source is an ultrasonic spherical transducer with frequency of approximately 300 kHz. The three component has central frequency of 1.0 MHz, that means we are able to read signals from tenth kHz up to 2-3 MHz, but the maximum sensitivity is 1.0 MHz. The hydrophone (4th component) has central frequency 300 kHz. They were put in contact with the solid model on the bottom of a water layer. Pressure sensor was used just above the sea floor to simulate the 4C Ocean Bottom Nodes sensor as in the figure 4.17.

The acquisition parameters and its equivalent in the real world can be seen in the Table 4.7.

Mason (2013)[91] observes that converted-wave imaging is improved by reducing the source spacing, due to the higher fold, using deeper sources and receivers (onshore) and employing larger sources. In this study, we have used a large source and short source spacing for higher fold.
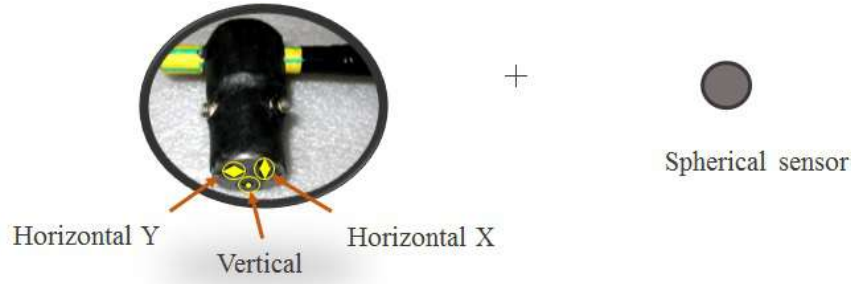
Figure 4.17: 4C sensor composed by a 3C and a spherical sensor.

Table 4.7: Acquisition parameters.

Parameters	Values	Model values
Line length	4000 m	400 mm
Receiver interval	50 m	5.0 mm
Source interval	25 m	2.5 mm
Water level	1000 m	100 mm
Source depth	70 m	7 mm
Number of shots	161	-
Number of receiver positions	80	-

The figure 4.18 is the picture from the tank's glass window on the pool's side.

Figure 4.18: Acquisition running. The model is placed over a table, covered by water and the water mirror on the top of the picture.

The physical modeling was performed several times, in the way that 2D seismic data was acquired and processed for 161 shots and repeated 80 times.

4.6 Data Preview and Processing Planning

The basic purpose of this section is to get to know the data, assign geometry and to plan the workflow that will be applied for processing the data. Water-bottom data was acquired at a 2D line avoiding the first stage geophone rotation to source azimuth direction correction (e.g. GUIMARÃES *et al.*, 2017[92]).

79

Multicomponent data usually have all channels well ordered in the dataset. The very first step is to know from the survey which channel each trace comes from; and then separate components to set up geometry to start processing it channel by channel.

After components separation, data is organized in common receiver gather (CRG). These CRG are analysed via a quality control workflow and this is also the sort used for OBN data processing due to the density of traces presented at each gather, with its equidistant spacing lowering the spacial alias effect.

Figure 4.19 show zoom out at the CRG 1 for the vertical channel with event identification.
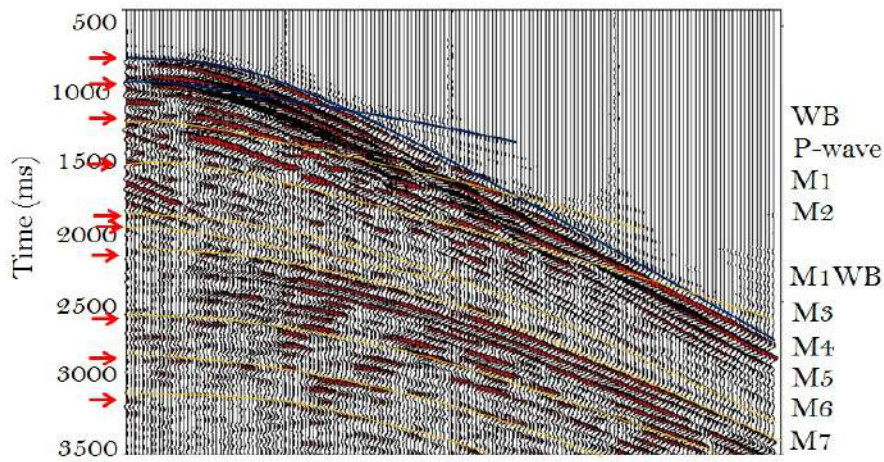
Figure 4.19: CRG 1 shows event identification at vertical channel.

The first two events are water-bottom or direct wave from the source and carbonate bottom reflection (P-wave first reflection in the figure). Computed arrival times are shown in Table 4.4 in computational modeling section 4.6. P-wave first reflection is higher velocity than water-bottom event. Figure 4.20 shows zoom in at the CRG 1 for the vertical channel with event identification. Zero stack shows events in Figure 4.21.

Dip events below 1,500 ms might be boundary reflection from the left and right sides of the carbonate layer. Alias at the zero stack data is due to low sampling for limited offset data while full offset data is free from alias. As shown by the computational modeling, multiples (M1 to M7, and M1WB, M2WB and M3WB) are not messing up events of interest at zero offset (WB and P-wave reflection), because they appear later in time (see Figure 4.19). The first internal multiple, M1, might be a problem if it interferes with the P-wave reflection at longer offsets. Therefore, multiples will be attenuated via Radon parabolic transform which works with differences in features of moveout from events. Next there is the first velocity analysis

80
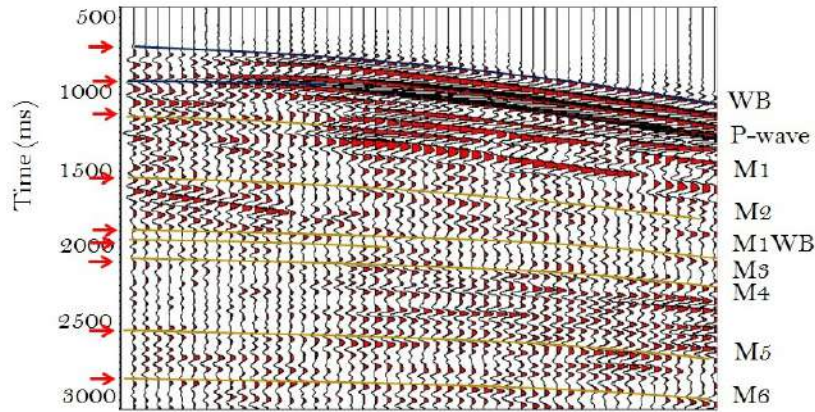
Figure 4.20: Zoom in at CRG 1 shows event identification at vertical channel.
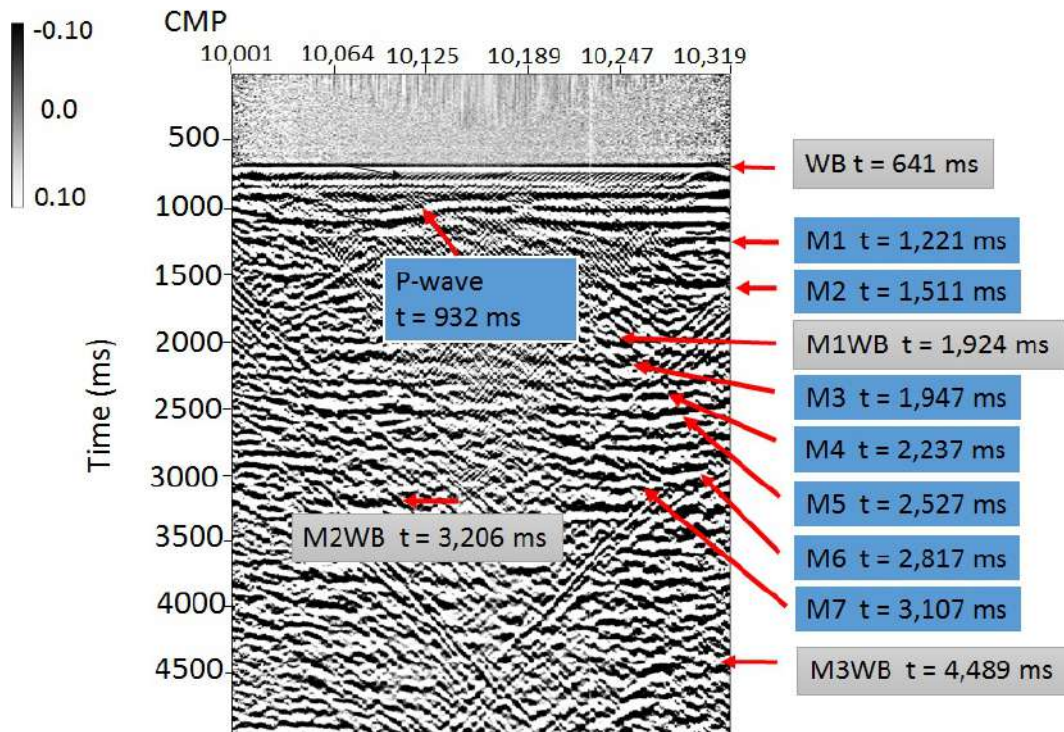
Figure 4.21: Event identification at CRG stacked data.

followed by multiple attenuation and a second velocity analysis with comparison. Most of the multiples are deeper in time than the two main events so they might not cause troubles at short offsets. However, multiple attenuation is a good approach to get rid of major undesirable energy in the data.

4.6.1 Processing Workflow

A summary of the processes in the seismic processing workflow sequence are presented on Table 4.8.

Table 4.8: Seismic processing workflow

General Processing Step	Details of Application
Geometry	Assigning the geometry in header
Preprocessing	Checking spherical divergence and
	datum statics, CCP and CMP sorting
Trace edit	Kill trace 1611 and polarity reversal for PS-wave
Frequecy Content	Frequency panel
Filters	Bandpass filter and other filter tests
Deconvolution	Spyke deconvolution to make the wavelet sharper
Multiple atenuation	Least Square Parabolic Radon transform
Velocity analysis (velan)	NMO correction and two iteractions of velan
Migration	Prestack Kirchhoff Time Migration
Final filters	Filter tests

Trace number 1,611 is an extra trace which is repeated in the data accidentally. It should be removed from each channel before processing to avoid geometry problems. Besides, traces from converted-wave data need to have their polarity inverted at one side of the source, due to the asymmetry generated around the source, showed in section 4.4.

The processing workflow that is applied to the ultrasonic water-bottom data is presented channel by channel. You may notice that repeated processes for the horizontal components are omitted in the sections for simplicity. The processing flow was implemented using the Seismic Unix and some of Vista software[5]. From here after, time, frequency and space will be treated as in real world scale.

A physical modeling experiment scaled 1:10,000 is expected to have drawbacks due to sensor size that might cause some diffractions. In this case, it possibly cause some confusion at arrival time at zero offset.

4.6.2   Geometry and Fold Map

Since geometry and datum corrections are similar for any channel, they will be treated in this section. Dr. Nikolay from AGL had made a good work in sanding the carbonate layer model at the UH. He also sculpted the anomaly and helped me with the experiment. Due to his well done work, we will assume that there is no near-surface distortions and there is no need to apply statics corrections in the data.

Assigning the geometry is always a challenge even for the most experienced people in the geophysicist industry and it was no different for the author. Despite

---

[5]Schlumberger software, license provided to the University of Houston.

not having processed several seismic data sets previously the author learned a lot during the processing of the water-bottom data. Basically, the data says what it needs to be applied. Even if you are not an experienced geophysicist in seismic processing, with some theory and advising you will find the right workflow with time.

Assigning geometry was started in Houston, using Vista Software (Schlumberger student license for the University of Houston). Back in Rio and no longer with Vista available the author started using Seismic Unix (Colorado School of Mines open software). That was a challenge to insert the field geometry with the data coordinates of shots and receivers to match correctly in the headers working with softwares that are not appropriate for water-bottom geometries.

Yilmaz (2001[58]) says that "Many types of processing problems arise from setting up the field geometry incorrectly", and the author could experience what he had said. A couple of months later, the problem was solved. Then it was all set to start the processing.

Shots are done over an end-on beginning and ending geometry with asymmetric to symmetric split-spread in between as shown in Figure 4.22
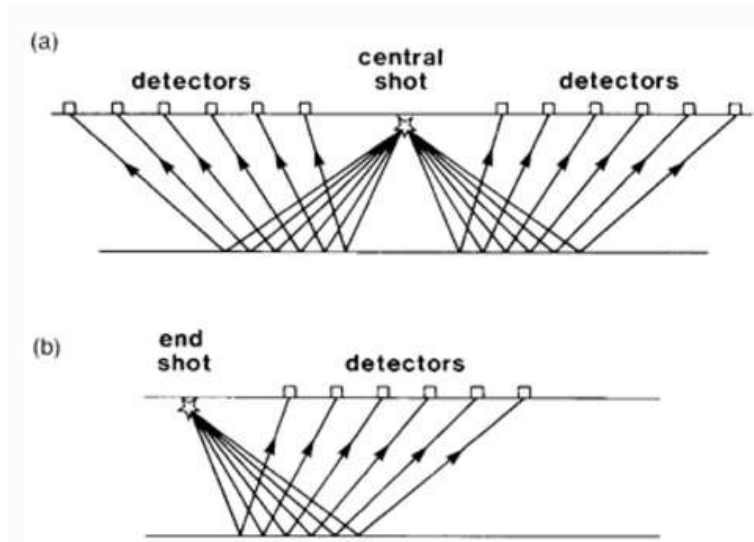
Figure 4.22: (a) split-spread and (b) end-on geometries.

The main goal of seismic processing is signal enhancement and noise suppression. Data redundancy using the multiple ground coverage method provides the leverage and is necessary for accurate velocity determination (NEIDELL *et al.*, 1980[93]). Seismic data acquisition is done in shot-receiver coordinates, while many seismic data processes are carried out in midpoint-offset coordinates.

Each trace is assigned to the midpoint location to achieve the coordinate transformation, based on the field geometry, this is halfway between the source and the receiver considering flat layered geometry. Through this sorting, traces with the same midpoint location are grouped together to form a common midpoint gathers (CMP). According to Yilmaz (2001[58]), a CMP is a set of traces with different offsets which sample the same subsurface point to enhance the strength of reflected arrivals.

The first thing done as quality control (QC) for the geometry is the fold map. ΔCMP = 12.5 m and ΔCCP = 8.33 m are computed according to Equations 4.4 and 4.5, respectively. For C-wave they are calculated as a function of the offset, the reflector depth and the velocity ratio $\frac{V_P}{V_S}$.

$$\Delta CMP = \frac{X_S - X_R}{2} \tag{4.4}$$

$$\Delta CCP = \frac{X_R - X_S}{1 + \frac{V_P}{V_S}} \tag{4.5}$$

where, X_R is receiver coordinate, X_S is source coordinate, V_P is compressional-wave velocity and V_S is shear-wave velocity. While CMP is located halfway between source and receiver, CCP is located about $\frac{1}{3}$ receiver-source distance, closer to receiver.

After stacking CMPs and CCPs the fold is computed. P-wave and C-wave fold maps are showed in Figures 4.23 and 4.24. P-wave maximum fold is 80 and C-wave maximum fold is 26, placed over the target for both as planned and that should image the anomaly. While P-wave fold increases from 1 to 80 and decreases to 1 at the last CMP keeping its maximum coverage at the central CMP, C-wave fold increases from 0 to 26 at CCP = 160 keeping the maximum coverage until CCP = 220 decreasing to 0.
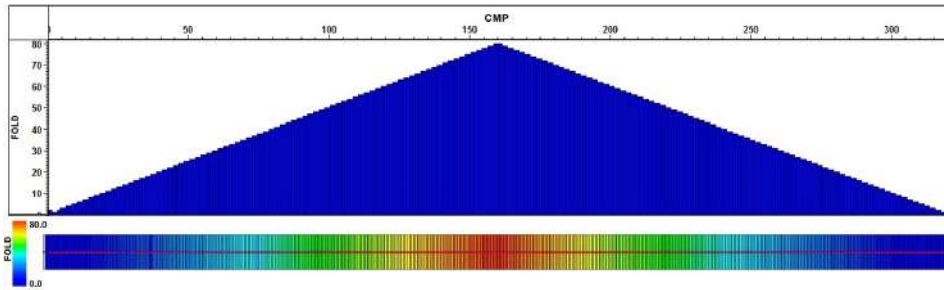
Figure 4.23: P-wave fold map shows coverage by CMP.

Though P-wave has bigger maximum fold, the number of common midpoints (CMPs) is smaller than the number of common conversion points (CCPs), providing
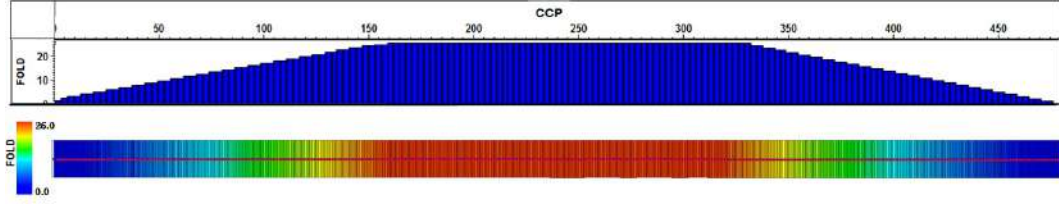
Figure 4.24: C-wave fold map shows coverage by CCP.

C-wave larger spacial sampling at shallow target than P-wave in agreement with theory (AKI & RICHARDS, 1980[85]). After assigning and QC geometry, seismic processing starts for each channel separately.

4.7 Vertical Channel Processing

Vertical channel in the 4C water-bottom data is the best source of P-wave information and also largely processed around the world. It provides good images from the overburden and information for the converted-wave data processing.

Raw CRGs at every 10 receiver stations are shown in Figure 4.25. Data from seismic surveys usually show energy decreasing with time due to geometric spreading, absorption and loss at interfaces by reflection (Sheriff, 1984[94]).
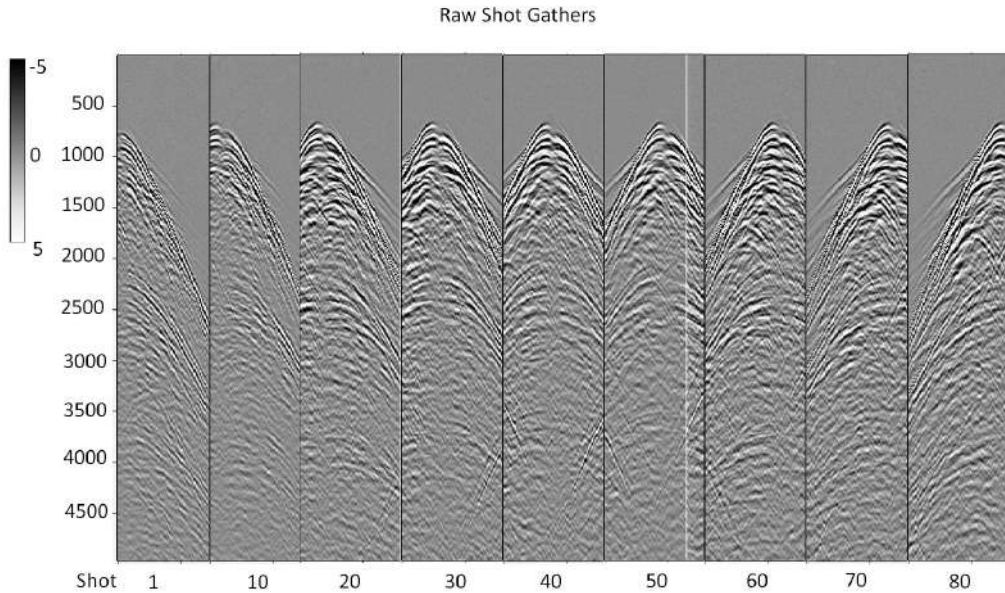
Figure 4.25: Raw CRG.

For this experiment, the model is composed by one layer, the water column over and below it, so there is no need to stress energy at greater time. Some of the receiver gathers on deeper events have shown even stronger amplitudes. In this case,

there is no need to apply gain recovery function to correct for the amplitude effects of spherical wavefront divergence (YILMAZ, 2001[58]). Besides that, it is already known the events of interest are shallow (computed event identification showed in computational modeling section 4.6), so it is not useful to apply spherical divergence correction).

By looking at CRG 40 it is possible to see those shallow events did not match very well for lower offsets (around the source) as in Figure 4.26. It may be an interference due to the diffractions and other effects from the top of the source, which is too large when it comes to the real-world dimensions. Sensors are less than two centimeters, but it represents more than a hundred meters size in the real world. We might need to kill traces around the source, hence not migrate near offset traces.
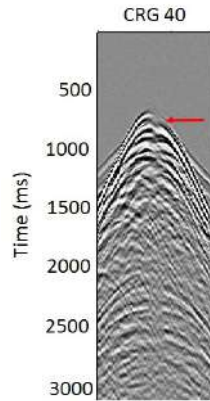
Figure 4.26: Diffraction from the receiver top mess up events for shallow data.

4.7.1 Frequency Content

Figure 4.27 show frequency versus amplitude spectrum. Frequency content shows high frequency due to the source frequency and sensors peak. Dominant frequency is 147 Hz and noise dominates the data for frequencies above 440 Hz.

Figure 4.28 show frequency panels with 100 Hz range each confirming that noise dominates the data above 400-500 Hz.

The best suitable bandpass filter to attenuate a few high and low-frequency noise and keeps important data features is 0-4-220-260 Hz. The filtered CRG is showed in Figure 4.29.

The comparison of Figures 4.29 (a) and (b) shows that a non-narrow bandpass filter improved data quality.
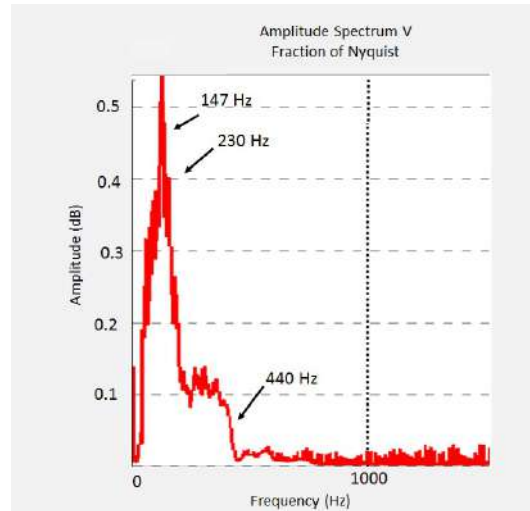
Figure 4.27: Frequency versus amplitude for vertical component.
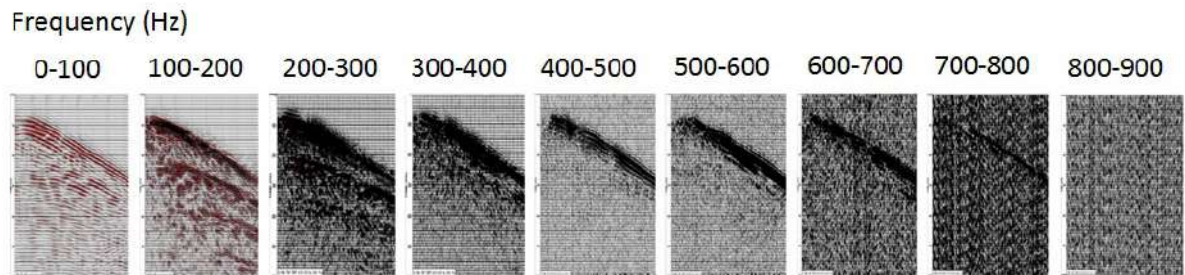
Figure 4.28: Frequency panels with 100 Hz each.
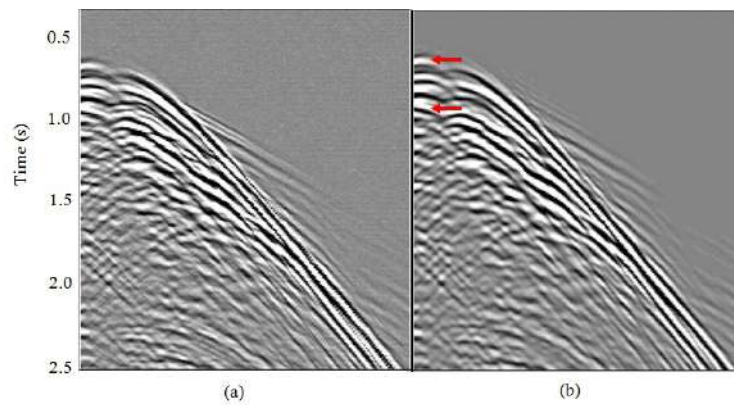
Figure 4.29: Bandpass filter applied to the CRG 7 for vertical component (2-4-220-260 Hz). (a) before and (b) after bandpass filter. Arrows highlight improved regions.

4.7.2   Velocity Analysis

Next, Normal Moveout (NMO) correction is applied to the data to correct (shift traces) and stack to enhance signal to noise. The velocity analysis process was started. The reflection travel time equation (Equation 4.6) predicts a hyper-

bolic shape to reflections in a CMP gather. The hyperbole become flattened with increasing velocity. Conventional semblance analysis of CMP gathers worked well to estimate velocity.

$$t_x^2 = t_0^2 + \frac{x^2}{V_1} \tag{4.6}$$

For each guess of normal moveout velocity (Vnmo), the data are vertically shifted by a time t_x, after which the semblance is calculated across all traces in the gathers within a vertical analysis window. These semblance "spectra" are plotted and picked by the seismic processor. Figure 4.30 shows semblance and CMP during velocity analysis. In (a) CMP 65 on the left of the anomaly, in (b) CMP 61 over the anomaly, and in (c) CMP 189 on the right of the anomaly. Red arrows shows correction for events of interest (compare with Figure 4.21).
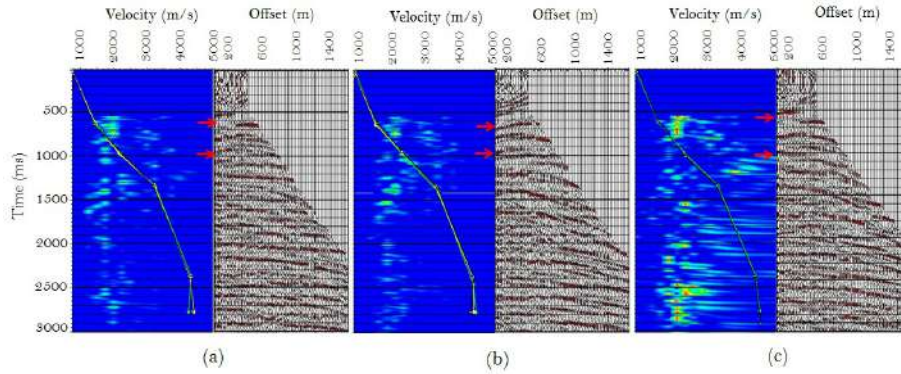
Figure 4.30: Velocity analysis (a) on the left of the anomaly, (b) over the anomaly and (c) on the right.

The stretched zone appears as a low-frequency distortion in low-frequency zone in the shallow section. For data with large offsets, stretching contaminates the shallow events when CMP gathers are stacked. Sometimes it is not worth to migrate long offsets if the target is shallow, because the fold is enough for imaging the target without major issues.

One of the major difficulties was to pick events via their energy in the data. The reason for this might be the big amount of multiples, water-bottom and internal multiples[6], were present in the data at deeper times as shown in Figure 4.19.

Figure 4.31 shows CRG 1 with NMO correction applied. Most events are flattened from shot 1 to shot 25 (approximately 625 m offset). Though larger offsets

---

[6]Seismic reflection event that has at least one downward bounce is happening at somewhere else in the subsurface it is an internal multiple. You will see better definitions in the multiple attenuation section.

show the pull-up or 'hockey stick' form for reflections between WB and P-wave
(Figure 4.20), the events of interest are well corrected by using the first velocity
analysis. As the non-corrected events are not the focus in this data, we just neglect
it for now.
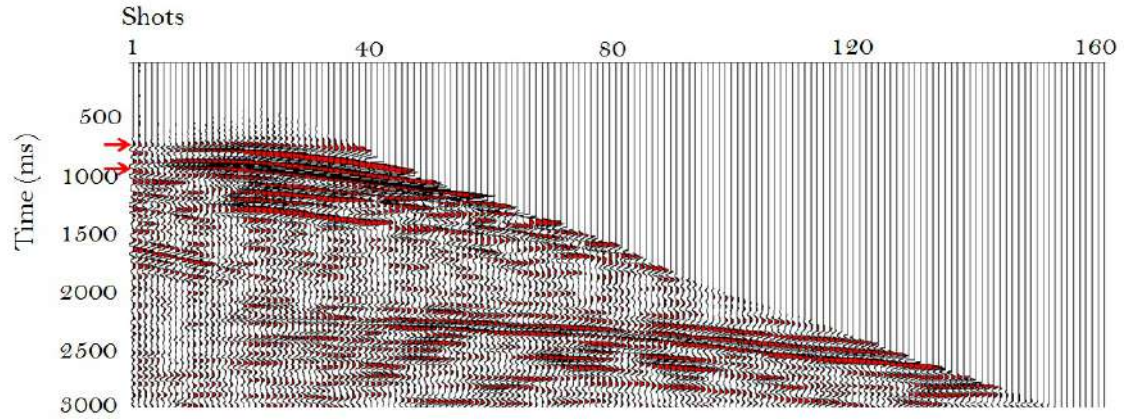
Figure 4.31: NMO corrected CRG 1 shows flatened events.

After the first velocity analysis stacked data is seen in Figure 4.32. Strong
energy events show up close to 2,000 ms, 3,000 ms and 4,000 ms. They are likely
to be water-bottom multiples which have been previously computed in the event
identification showed in the computational modeling Section to be close to 1,924
ms, 3,206 ms and 4,489 ms.
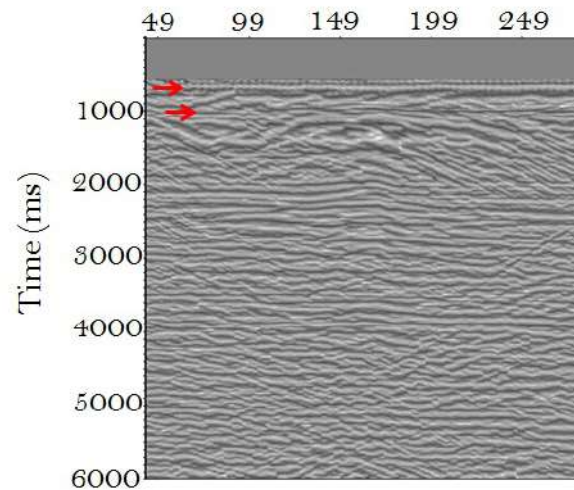
Figure 4.32: CMP stack.

4.7.3 Trace Edit

Traces around the source were killed to improve events at the stacked data.
Figure 4.33 shows raw CMP stacked data with all offsets (a) before and (b) after
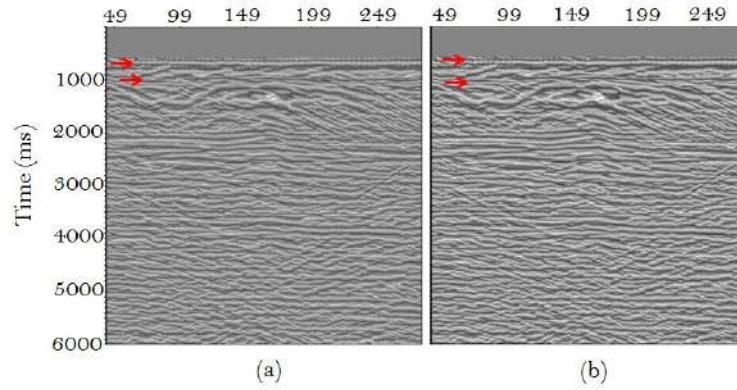
killing traces.

Figure 4.33: CMP stacked data. (a) before and (b) after killing traces around the source.

Figure 4.33 (a) show mismatch along the events, probably caused by mismatched amplitudes showed in Figure 4.26. Figure 4.33 (b) shows an improvement in the continuity of the events after killing traces with amplitude mismatch around the source. Trace 1611 is killed as mentioned in the workflow planning section.

4.7.4 Deconvolution

Deconvolution is a filtering process that actually applies the reverse process of convolution. It is designed to compress the source waveform to approximate a spike and therefore improves the temporal resolution between closely spaced reflections (YILMAZ, 2001[58]; STEIN *et al.*, 2003[95]). It reduces the source wavelet to a spike. The filter that best achieves this is called a Wiener filter. Spiking deconvolution was applied to the data (Figure4.34) to make events sharper and try to minimize the effect of reflections from the top of the source left after trace edit.

Deconvolution was applied with 60 ms operator length. Figure 4.34 demonstrates that wavelet shaping removed the strong influence of the near offset noise. Figure 4.35 shows raw CMP stacked data with all offsets before surface consistent deconvolution in (a) and after in (b). Reflections indicated by arrows are "sharper" after shaping.

4.7.5 Multiple Attenuation

Multiple events will happen for P-waves and for C-waves (converted waves). During processing multimode multiples will be taken into consideration to attenuate
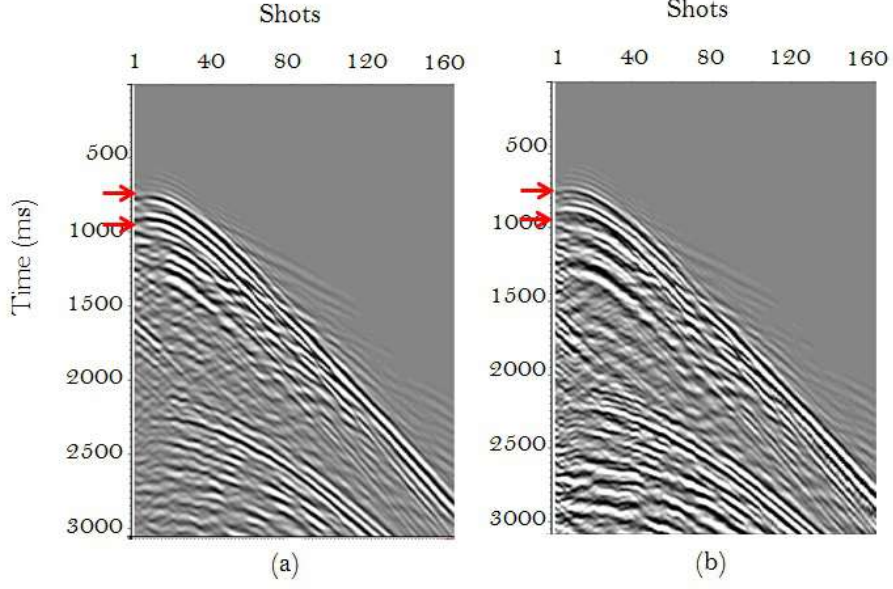
Figure 4.34: Representative CRG before (left) and after deconvolution (right).
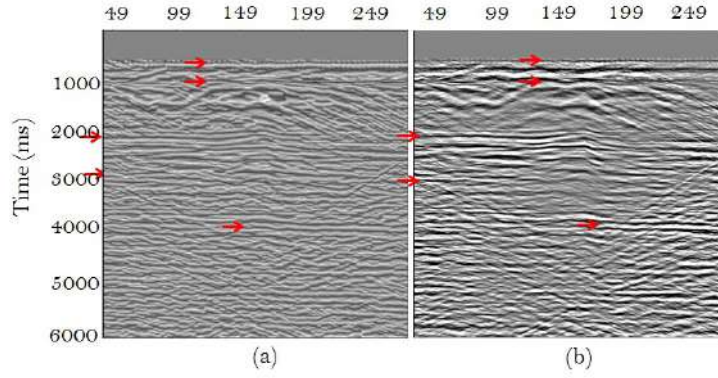
Figure 4.35: CMP stacked data. (a) before and (b) after deconvolution.

them via filtering or predictive method. Filtering methods are based on differences in features of the primaries and multiples and the predictive method is based on periodicity of multiples. Examples of filtering methods are FK, Radon, and t-x. Examples of predictive methods are predictive deconvolution and Surface Related Multiple Elimination (SRME).

Usually, multiples are considered to be a big problem in seismic measurements. For deep water (> 1,000 m) surface related multiples are reflections that arrive later in time, because the sea-bottom is late in time too. These reflections are usually more horizontal than the primaries. It is common that internal multiples arrive early in time due to the higher velocity in layers when comparing with water.

Multiple removal techniques can be subdivided into two main categories. One is based on difference in spacial behavior like moveout difference in offset direction

91

(mostly in CMP offset domain) or dip related difference after stack or migration (target oriented structural filtering). The other main category is based on periodicity and predictability. In this category one needs a primary to predict the multiple, it can be one-dimensional predictive deconvolution or multi-dimensional wave equation-based prediction.

The parabolic Radon technique is based on the fact that primary and a multiple reflection have different moveouts. If two events arrive around the same time in the seismogram, multiples have propagated more in the shallow part of the earth exhibit lower velocities, assuming that velocity slowly increases with depth. From the same assumption, a primary reflection would propagate at the deeper part of the earth, so being exposed to higher velocities, thus the arrival angle is slightly different. That would give it a moveout behavior as a function of the offset.

During Radon parabolic process one applies normal moveout correction and brings the data from the T-X domain to the Radon domain for muting the area with uncorrected events. Multiples will be undercorrected due to their slower velocities and so they will be removed. Though Radon Transform is one of the most used methods for multiple removal, that is not a perfect filtering. Small overlap in radon domain yields artifacts in reconstruction, especially for near offsets. Least-squares Radon transform was recently presented with more accuracy due to its high resolution for separation. Thus under the assumption that there is a moveout difference between primaries and multiples the filter will work fine.

Weighted Least Square Radon was applied with 150 ms maximum moveout for signal, and 4000 m of reference offset. Figure 4.36 (a) shows the Radon domain. Most events are at offsets between 0 m and 1,000 m. Figure 4.36 (b) shows semblance before Radon transform, where multiples can be seen all the way down the image. The first event is the water-bottom direct event with about 1,500 m/s and should appear at 641 ms but it seems that the amount of energy in multiples is vanishing its energy. At 932 ms almost in the middle of the image (about 2,300 - 2,600 m/s) there is a strong event which is a primary reflection from the carbonate rock bottom. Below this event others appear all the way down with lower velocity. They are internal multiples that are removed together with the water-bottom multiples after Parabolic Weighted Least Square Radon Transform. Figure 4.36 (c) shows the semblance after multiple removal. Energy from multiples are showed in (d).

With the aim of comparing a CMP before, after and the muted multiple Figure 4.37 outputs the multiples from the workflow. In Figure 4.37 (a) CMP 40 before applying Radon transform, with events of interest (0.641 s - 0.932 s) and multiples. Figure 4.37 (b) shows CMP after multiple removal and Figure 4.37 (c) shows multiple
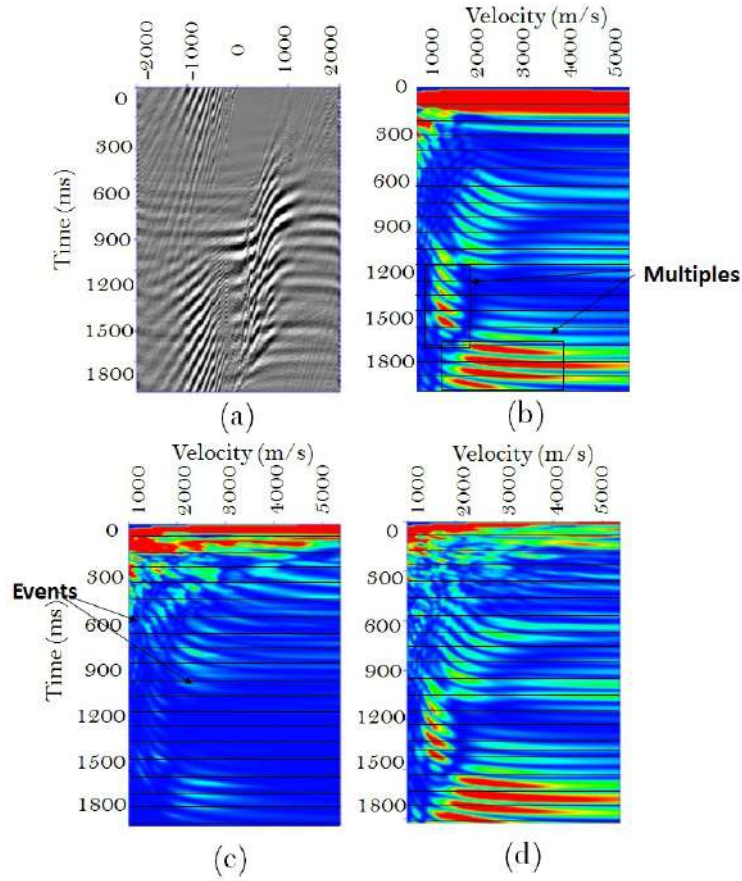
Figure 4.36: Radon Parabolic Transform and velocity analysis. In (a) Radon domain, (b) CMP before multiple attenuation, (c) after and (d) energy of multiples.

removed from the data.
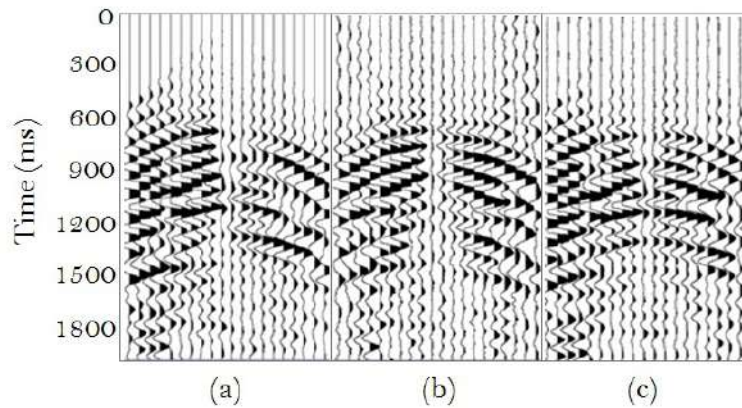
Figure 4.37: CMP 40 (a) before, (b) after Radon transform, and (c) muted multiples.

Attenuating multiples is useful to improve semblance quality helping in velocity peak. A combination of Radon Transform and Surface-related multiple elimination (SRME) would be a great choice to attenuate multiples in marine seismic data. The events from the target in the water-bottom data are shallow and the multiples

did not spoil them, so we will not go further in that direction. After assessing all the setbacks in the way, understanding those events, the second velocity analysis iteration was performed.

4.7.6 Migration

After NMO correction, events from dipping reflectors are still plotted in the wrong place on the stacked section. In this step they were corrected by migration which is the process that moves stacked seismic data into its correct position in both space and time. Reflectors need to be moved "up-dip" along the hyperbola in order to put them in the correct place. The shape of this hyperbola depends on the velocity field. Prestack migration is a process that moves each sample to all possible reflector positions and creates the image using the principle of constructive and destructive interference.

Bancroft *et al.* (1997)[96] define Kirchhoff time migration as curvilinear with linear ray paths approximation (Figure 4.38). Kirchhoff migration was applied to the data, summing energy along "diffractions"and placing them at the apex of the diffraction.
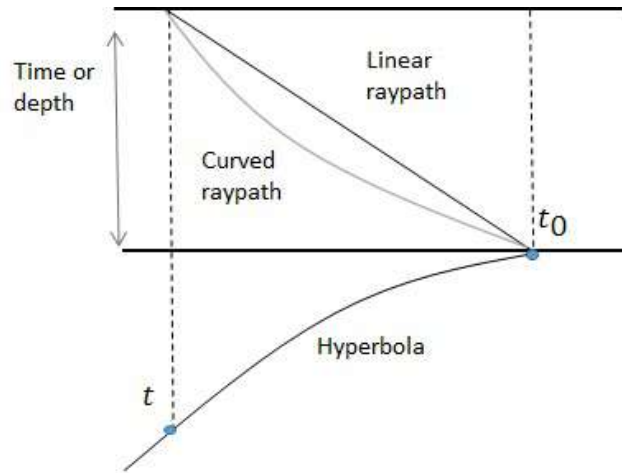
Figure 4.38: Migration scheme.

Figure 4.39 shows several common offset gathers (COG) and the anomaly clearly visible at short to mid offsets. It means that long offsets (> 600 m) can be muted without loss of quality in the anomaly image.

Data was migrated from -650 m to 650 m offset. Figure 4.40 shows the final section in time in (a) and in depth in (b) after Phase Shift Poststack Time Migration for P-wave.

94
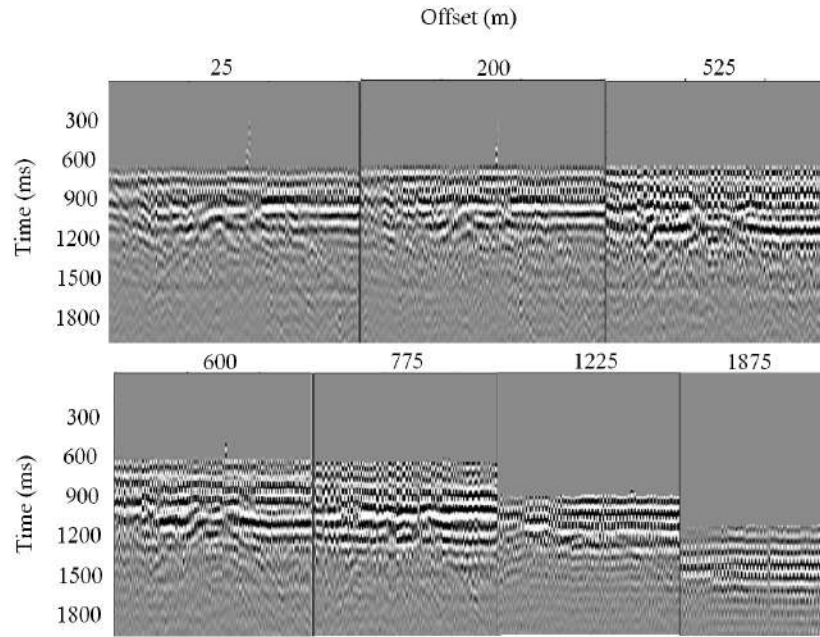
Figure 4.39: Offset stacks shows anomaly.
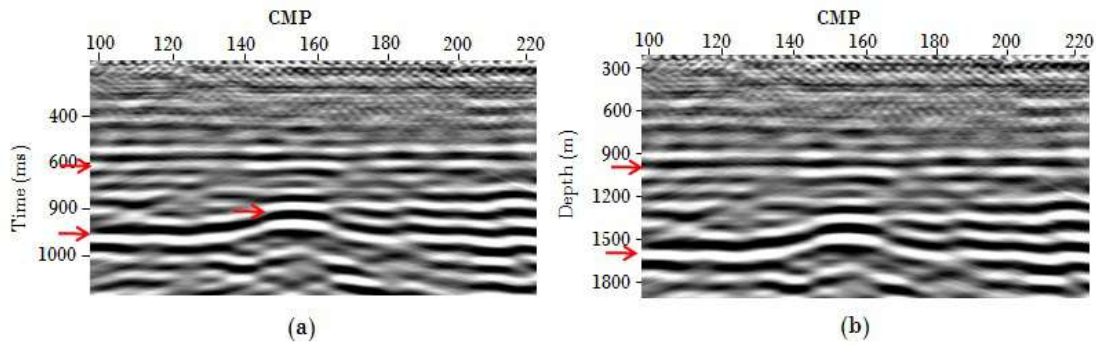
Figure 4.40: Final sections. (a) P-wave section in time and (b) P-wave section in depth.

Figure 4.40 shows anomaly clearly present in P-wave sections (a) and (b), the anomaly is correctly placed in both sections in time and depth. Water-bottom horizon appears at 6.41 ms, the reflection from the carbonate bottom is at 931 ms showed by arrows at the time section (a). At depth section, one can clearly see horizons at 1,000 m and 1,585 m depth (b).

4.8   Horizontal Inline Channel Preprocessing

This section presents the horizontal inline channel processing. For C-waves, data processes are carried out in CCP coordinates. For water-bottom data we expect to see converted-waves at the horizontal channel with inverse polarity around

the receiver station in CRG. Polarity reversal is applied and the data is sorted to Common Conversion Point (CCP) rather than CMP because of converted-waves' vectorial nature (See Figure 4.5).

The more complex part of C-wave processing is told to be their asymmetric source-to-receiver raypaths. C-wave have smaller reflection angles than P-wave reflections so that more information can be acquired in the same aperture. Many works state that lateral position of a conversion point varies with depth when the offset is constant (Chung and Corrigan, 1985[87]). In this experiment we are dealing with small offset to depth ratio, therefore, the asymptotic CCP binning approximation is usually good enough and we do not need to deal with depth-variant binning algorithms.

Asymptotic conversion point is showed in Equation 4.7 as gathering location. C-wave binning is showed in Figure 4.41 where ACP is the asymptotic conversion point and CCP varies with distance between source and receiver as well as the P- and S-wave velocities, or depth in the real world case.
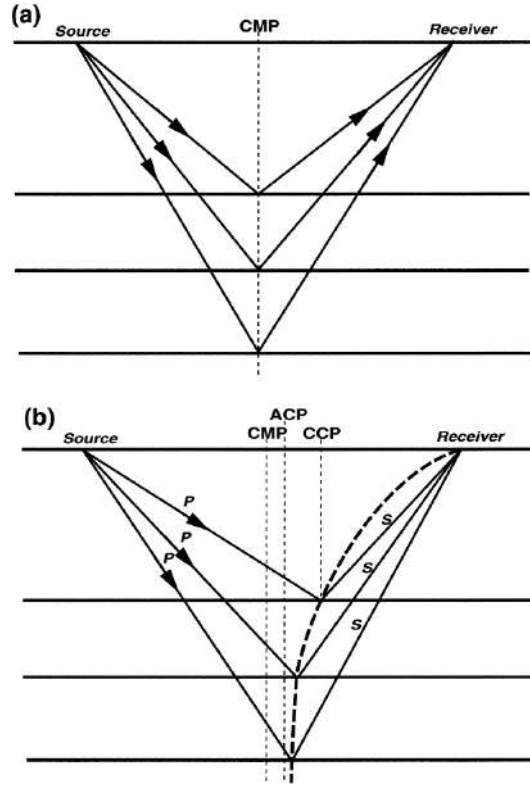
Figure 4.41: Scheme for (a) CMP and (b) CCP trajetory with many parallel layers (Dr. R. R. Stewart, class material).

$$X_{PS} = \frac{X_{sr}}{1 + \frac{V_P}{V_S}} \tag{4.7}$$

where X_{sr} is the distance between source and receiver and X_{PS} is measured from the source.

The C-wave stacking velocity is showed in Equations 4.8 and 4.9.

$$V_{rms}^2 = \frac{\sum_{i=1}^{N} V_{Pi}V_{Si}t_{PSi}}{t_{PS}} \tag{4.8}$$

$$t_{PS} = \sum_{i=1}^{N} t_{PSi} \tag{4.9}$$

t_{PSi} is two-way vertical travel time trhough i'th layer. V_{Pi} is the P-wave velocity of $i-th$ layer. V_{Si} is the S-wave velocity of $i-th$ layer.

C-wave reflection point is showed in Equation 4.10

$$X_{PS} = \frac{X}{1 + \frac{V_P^{1j2}T_P^{1j}}{V_S^{1j2}T_S^{1j}}} \tag{4.10}$$

As the experiment model is a shallow depth layer, we expect to see higher resolution PS-waves than for P-waves (MARK A. MEIER and PAUL J. LEE, 2009[97]). Figure 4.42 shows representative CRGs for the inline channel.
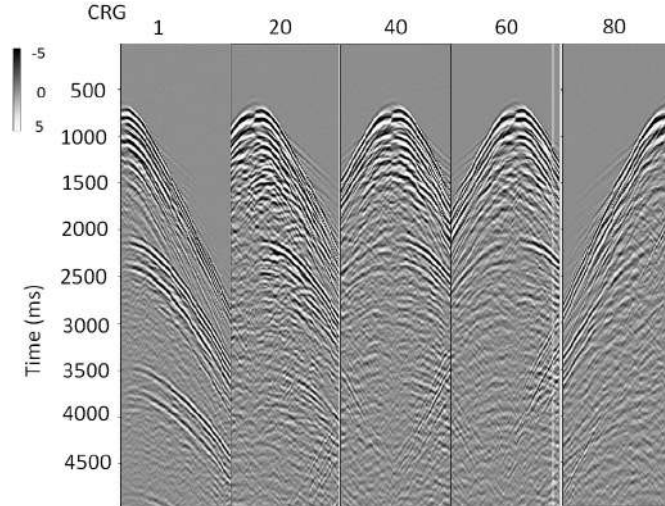
Figure 4.42: Representative CRGs for the inline channel

Some of the same features shown by the previous data are exhibited now at the inline component. Possible diffractions are messing up data around the source, presented on the right side of Figure 4.43. Inline channel present polarity reversal at one side as showed in earlier sections.
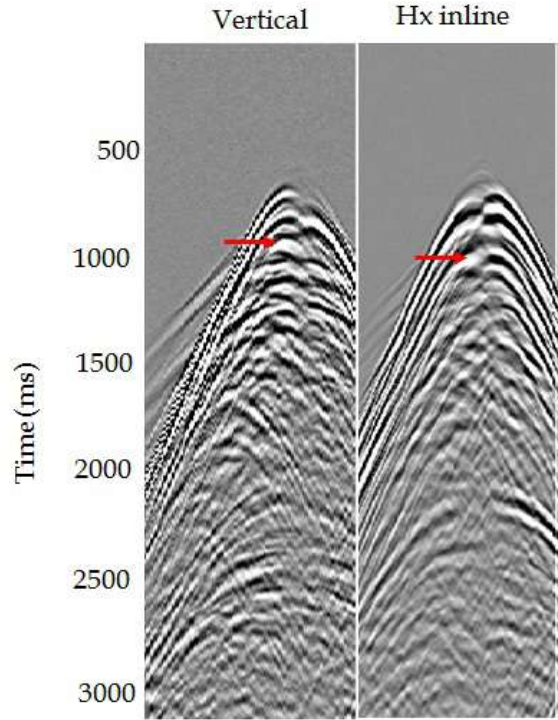
Figure 4.43: Comparison between CRG 50, Vertical channel on the left and horizontal inline channel on the right. Both present a sort of diffraction on the data.

Spherical divergence correction was not applied to the data because there was no need to see shallow reflections. As shown by the computational modeling, multiples (Mh1 to Mh7, and M1WB, M2WB and M3WB) might not mess up events of interest (WB and C-wave reflection), because they appear later in time.

4.8.1 Frequency Content

Figure 4.44 shows frequency versus amplitude spectrum. Frequency content shows high frequency due to the source frequency and sensors peak. Dominant frequency is 133 Hz and noise dominates the data for frequencies above 420 Hz.

Figure 4.45 show frequency panels with 100 Hz range each for P-wave confirming that noise dominates the data above 445 Hz.

Using a light bandpass filter that attenuates a few high and low-frequency noise but keeps important data features was chosen to be the best. BP filter was applied at the data as 0 Hz - 200 Hz. The receiver gather after filtering is showed in Figure 4.46. Red arrows show enhanced signal in the region of interest.
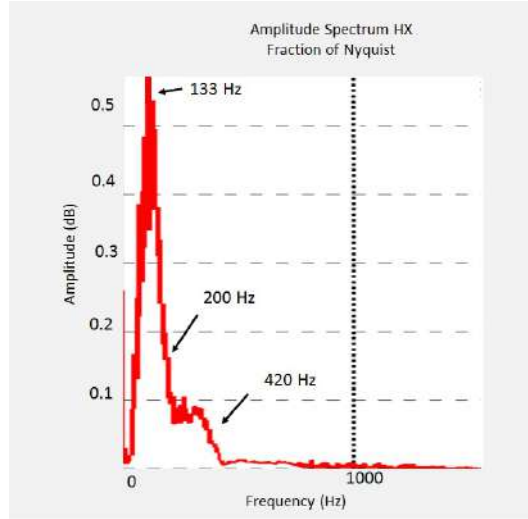
Figure 4.44: Frequency versus amplitude for vertical component.
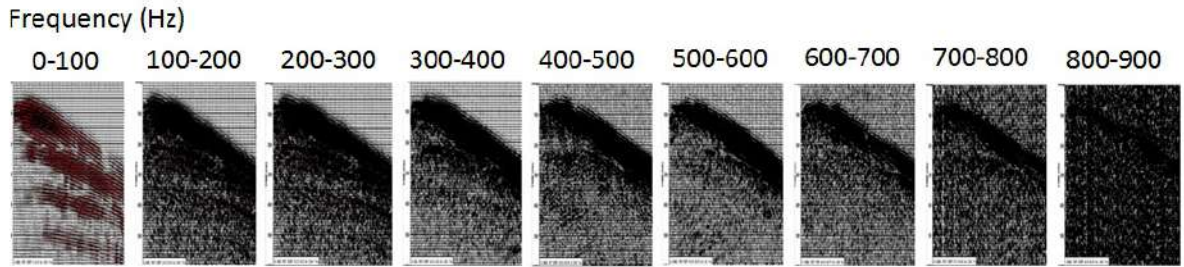
Figure 4.45: Frequency versus amplitude for Horizontal inline component.
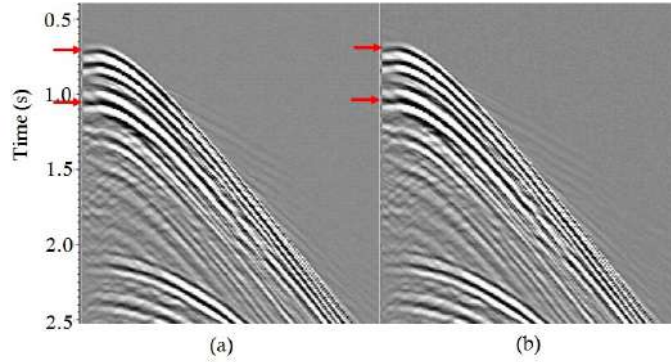
Figure 4.46: Bandpass filter applied to the CRG for horizontal component (0-2-180-200 Hz). (a) before and (b) after BP filter.

4.8.2 Trace Edit

As shown in the computational modeling section, horizontal components have opposite polarities on both sides due to the nature of the sensor that measures the wave horizontal particle motion. During processing, data is sorted to common conversion point (CCP) to apply trace stack enhancing the signal. Stacking traces in CCP would cancel amplitudes due to the asymmetry in polarity. Polarity of the

99

inline data with negative offset was reversed. This technique prevents stacking of the data with offsets of opposite signs to cancel each other. The resultant CRG 14 is showed in Figure 4.47
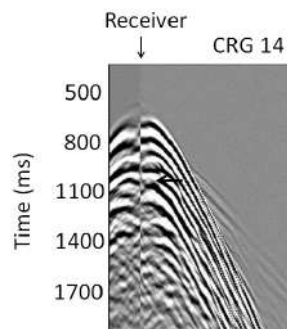
Figure 4.47: CRG 14 after aplying reverse polarity.

Notice that events are matching both sides of receiver station and there is a lack of signal in the very close to receiver region that is due to the absence of conversion at zero offset as mentioned before. Due to that, it is not necessary to kill traces around the receiver position. Anyway, if that is still a problem we might not migrate real short offsets. Trace 1611 is killed as mentioned in the workflow planning section.

For PS-waves, the reflection point imaging is asymmetric even for zero-dip events. Each trace is assigned to the CCP location to achieve the coordinate transformation, based on the field geometry, P-and S-wave velocities in the medium. In this data the CCP is located somewhere around a third the offset between source and receiver (closer to receiver) considering flat layered geometry. Through this sorting, traces with the same CCP location are grouped together to form a CCP gather.

For this data, each CCP gather contains from 1 to up to 26 traces, with maximum fold equals to 26. CCP numbers range from 1 to 480. Next, Normal Moveout correction is applied to correct (shift traces) and stack to enhance signal to noise. Next step is the velocity analysis process.

4.8.3 Velocity Analysis

The horizontal component had also a complex velocity to pick since there are several high energy events from multiple reverberations. Semblance is showed in Figure 4.48 with corrected CMP during velocity analysis on the side. In (a) CMP 170 on the left of the anomaly, in (b) CMP 240 over the anomaly, and in (c) CMP

310 on the right of the anomaly. Red arrows show events of interest at the CCP gather.
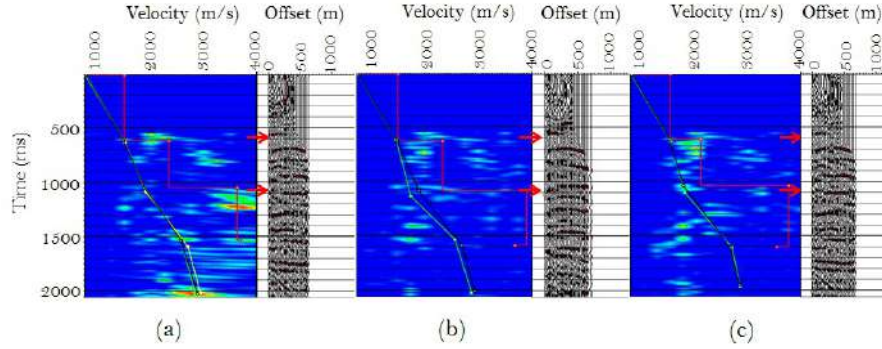
Figure 4.48: Velocity analysis (a) on the left of the anomaly, (b) over the anomaly and (c) on the right.

First CCP stack is showed in Figure 4.49
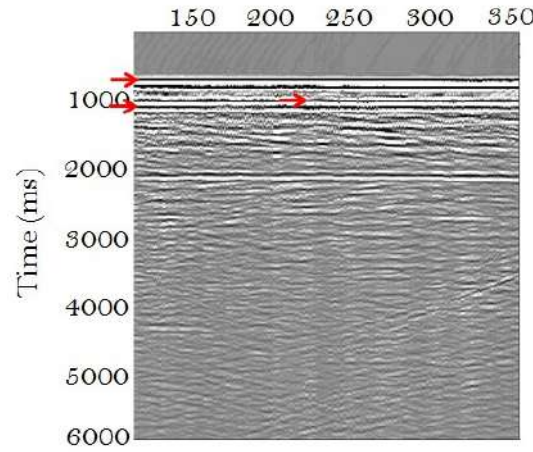
Figure 4.49: CCP stack of the inline channel.

There is an event with strong energy close to 2,000 ms, which is probably the water bottom multiple M1WB identified at 1,924 ms in Table 4.5 (Section 4.4). The anomaly is not too clear in the CCP stack as it was in the vertical component. Migration prestack can be suitable for the converted wave and it is worth the computational time to make the anomaly visible.

4.8.4   Deconvolution

Spiking deconvolution was applied to the data to make events sharper and try to minimize the effect of reflections from the top of the receiver. Figure 4.50 shows data before deconvolution in (a) and after deconvolution in (b). Notice arrowheads showing main events.
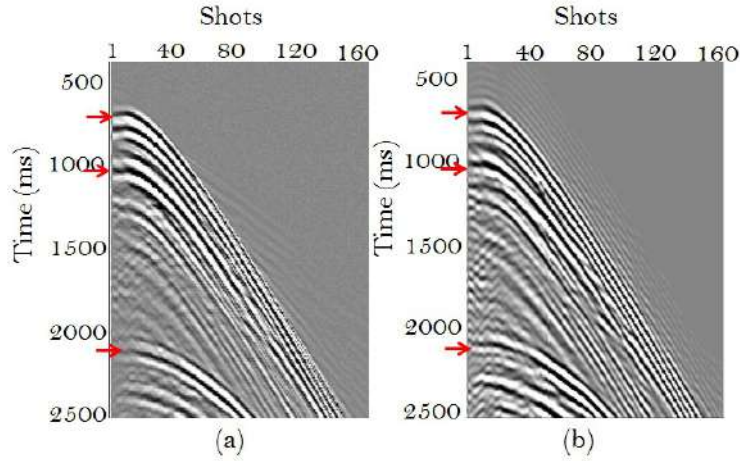
Figure 4.50: CRG a) before, b) after deconvolution.

Deconvolution was applied with 40 ms operator length. F-K filter was applied after deconvolution for high frequency noise attenuation. Bandpass filter 0-2-180-200 Hz was applied as well.

Figure 4.50 demonstrates that wavelet shaping removed the strong influence of the near offset noise. Reflections indicated by arrows are "sharper" after shaping.

4.8.5 Multiple Attenuation

Weighted Least Square Radon was applied with 150 ms maximum moveout for signal, and 4,000 m of reference offset. Figure 4.51 (a) shows the Radon domain with most events between 0 m and 1,000 m offset. Figure 4.51 (b) shows semblance before Radon transform, where multiples appear with low velocity at the image. The first event is the water-bottom direct event with about 1,500 m/s and should appear at 641 ms but it seems that the amount of energy in multiples is vanishing its energy. At 1072 ms almost in the middle of the image (about 2,300 m/s) there is a strong event which is a primary reflection from the carbonate rock bottom. Below this event others appear all the way down, mostly with lower velocity. They are internal multiples that are removed together with the water-bottom multiples after Parabolic Weighted Least Square Radon Transform in the Figure 4.51 (c). Energy from multiples is showed in (d).

To compare CCP before, after and the muted multiple Figure 4.52 outputs the multiples from the workflow. In Figure 4.52 representative CCP is showed before applying Radon transform in (a), with some events below the zone of interest (0.641 s - 1072 s) which are removed and showed in (b) and the multiple removed is in (c).
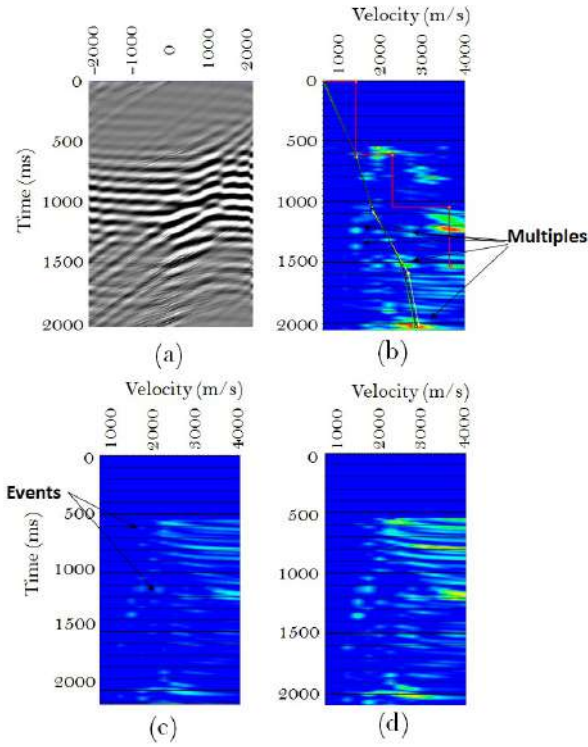
Figure 4.51: Radon Parabolic Transform and velocity analysis. In (a) Radon domain, (b) CMP before multiple attenuation, (c) after and (d) energy of multiples.
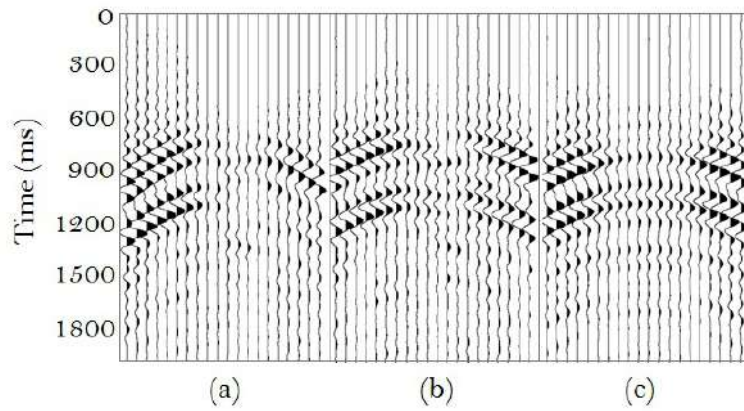
Figure 4.52: CCP (a) before, (b) after Radon transform, and (c) muted multiples.

Multiples at deeper time were well attenuated. Since the process of Radon Transform is not perfectly inverted, some left energy remaining from the process is commonly found. Other parameters for Radon Transform were tested, but either too much energy from the data were vanished or almost no multiples were attenuated.

4.8.6 Migration

Inline channel is usually processed and migrated before stacking the data, to put energy in the right place. According to Harrison (1992)[98] C-wave curves on a zero-offset PS section are approximately hyperbolic to first order and this means that the migration can be done similarly to conventional monomode P-wave zero-offset migration.

Data was migrated from -650 m to 650 m offset. Figure 4.53 shows PS sections in time in (a) and in depth in (b) after Kirchhoff Prestack Time Migration.
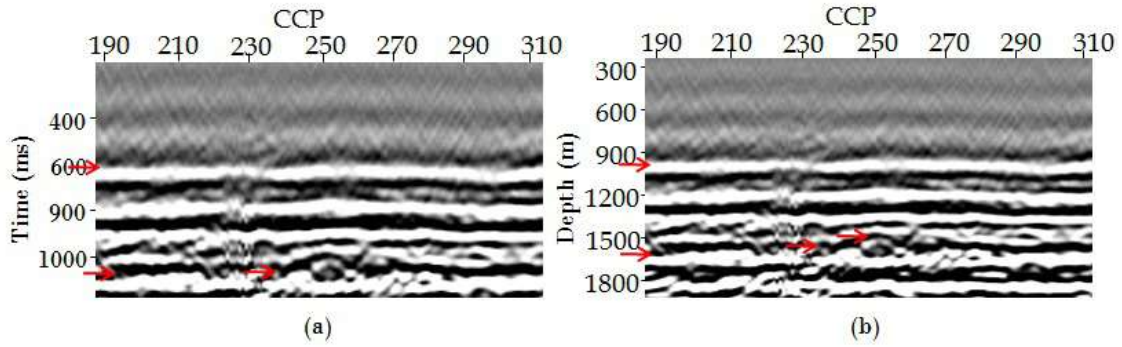
Figure 4.53: PS section in time (a) and in depth (b).

In Figure 4.53 the anomaly is clearly presented in PS-wave sections (a) and (b), the anomaly is correctly placed in both sections in time and depth. Water-bottom horizon appears at 6.41 ms, the reflection from the carbonate bottom is close to 1,072 ms showed by arrows at the time section (a). At depth section, one can clearly see horizons at 1,000 m and 1,585 m depth (b).

4.9 Correlation of P-wave and C-wave Depth Image

It is generally difficult to correlate a monomode P-wave section in time with the correspondent C-wave section due to uncertainties in wave amplitudes and velocity model. The same difficulty also exists in depth section correlation analysis, but some observations are done as follows.

Even though the dome is more clearly presented in P-wave sections Figure 4.40 (a) and (b), the anomaly is present at the right position in both sections in time and depth. For both time sections, water-bottom horizon appears at 6.41 ms, the reflection from the carbonate bottom is at 931 ms for P-wave Figure 4.40 (a) and

1,072 ms for C-wave Figure 4.53 (a) (showed by arrows). The anomaly is showed at 915 ms at P-wave section (a) and at 1,010 ms for C-wave section (b). At depth sections, one can clearly see horizons at 1,000 m and 1,585 m depth for both P-wave (c) and C-wave Figure 4.53 (b). The dome is close to 1,410 ms in both.

4.10   Horizontal Crossline Channel

The horizontal crossline component raw stack section is showed in Figure 4.54 does not show the anomaly very well.
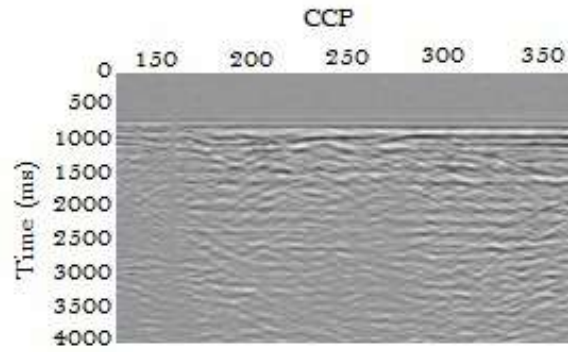
Figure 4.54: Stack of the raw data for the crossline channel.

The leaking energy found in Figure 4.54 is not expected for isotropic medium. According to (E. LIU *et al.*, 2000[99]) small energy at the crossline channel is normally regarded as a direct indication of azimuthal anisotropy. It motivates this research to go further for anisotropy investigation in the water-bottom data. The next chapter with carry on the preparation of the anisotropy investigation workflow for converted P- to S-waves with water-bottom data.

4.11   Hydrophone Channel

After all the experiment preparation the experiment run for several days. The spherical sensor unfortunately have failed for intermediary shots. Due to the limited time that the author had to stay in Houston for the research, it prevented us from processing it or performing further investigations using this channel.

4.12 Final Analysis of PS-wave Data

Carbonate rocks are likely to be anisotropic due to the their usual heterogeneity and also to the existence of fractures caused by tectonics or stress following deposition. Considering that, it it is possible that the rock in the model presents evidences of anisotropy. In fact the leaking energy found in the crossline channel was not expected to appear if that was an isotropic medium and small energy at the crossline channel is normally regarded as a direct indication of azimuthal anisotropy.

Figure 4.55 shows the geometry for the water-bottom experiment with wide azimuth for one single receiver gather in (a). 161 shots were performed for one position of the receiver with configurations: Δx = 25 m and Δy = 170 m scaled 1:10,000. The time delay Δt between C-wave arrivals varying with azimuth from 0° to 170° . Some parameters for the experiment are presented in Table 4.9.

Table 4.9: Stations, offsets, and angles for the geometry. θ_i is the angle between the offset and the y axis. Azimuth is the angle with North.

Station	Offset (m)	θ_i (°)	Azimuth (°)
1	-989.71	-80.11	9.89
20	528.11	-71.22	18.78
80	1,014.35	80.35	170.35

In Figure 4.55 (b) delay time between two C-wave arrivals varying with azimuthal angle shows a type of symmetry nearby 95°. The symmetry indicates possible azimuthal anisotropy in the carbonate that is investigated in next section.

As indicators of azimuthal anisotropy were found in the PS-wave data from the water-bottom experiment, the computational code developed in Chapter 5 is suitable to be employed for further investigations over the carbonate.

4.13 Conclusions

The water-bottom experiment was successfully performed. The OBN experiment was undertaken using ultrasonic physical modeling. A 2D seismic line was performed, and data was acquired and processed for 161 shots and repeated 80 times with 4C sensors.

Though both data, vertical and inline channels, had a complex velocity semblance to pick, the final sections clearly present the main events and the anomaly
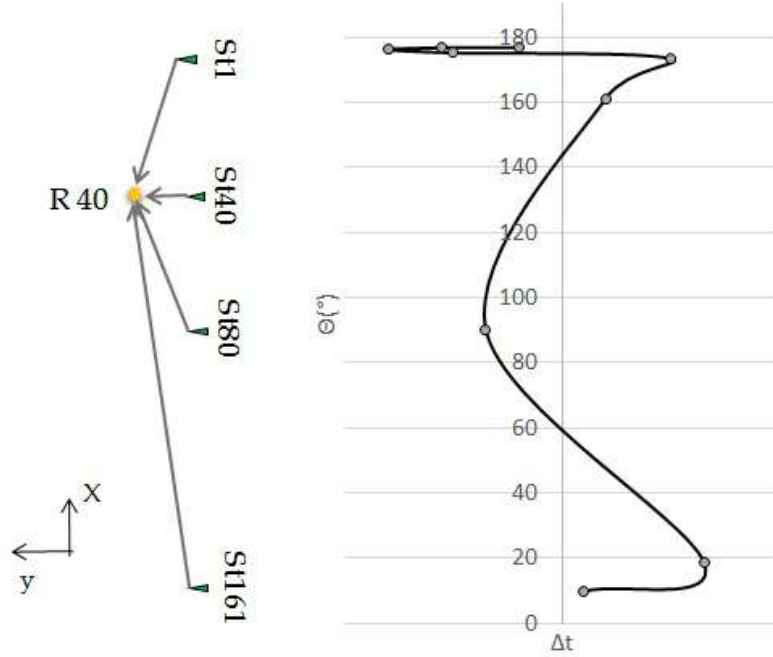
Figure 4.55: Geometry for anisotropy preliminary investigation (a) and resultant Δt variation with the azimuthal angle for converted-wave in the water-bottom experiment (b).

placed over the right time and depth. The final section after the processing was migrated with Phase Shift Poststack Time Migration for P-wave and Kirchhoff Prestack Time Migration for C-wave.

Time sections have shown water-bottom horizon placed at 6.41 ms, the reflection from the carbonate bottom is at 931 ms for P-wave and 1,072 ms for C-wave. The anomaly is showed at 915 ms at P-wave section and at 1,010 ms for C-wave section. At depth sections, horizons are presented at 1,000 m and 1,585 m depth for both, P-wave and C-wave data. The anomaly is close to 1,410 m in both depth sections. Data central frequency, in real world scale, is 147 Hz for P-wave and 133 Hz for C-wave. Spyking deconvolution showed very good results in shapening events at the P-wave section more than for C-wave section.

Internal and water-bottom multiples were found in both data and attenuated by using Radon parabolic Transform. Strongest energy water bottom multiples computed at the event identification in the computational modeling section showed up very close to the computed time (1,924 ms, 3,206 ms and 4,489 ms). They were not a big issue due to their late arrival in time, which is not the case for internal multiples.

In this chapter, the multiple attenuation Section showed semblance before Radon Transform with the energy of water bottom and internal multiples, after

Radon Transform when multiples were mostly attenuated and semblance with energy from the removed multiples. That analysis confirmed that most of the multiples were attenuated in the data.

P-wave maximum fold is 80 while C-wave maximum fold is 26. Although P-wave achieves major maximum fold than C-wave, its spacial sampling is lower (12.5 m for P-wave and 8.33 m for C-wave). C-wave spacial resolution exceeds P-wave for shallow data. If there were deeper analysis we could expect a crossover point of equal P-wave and C-wave resolution where P-wave resolution becomes bigger than C-wave resolution with depth (DEFFENBAUGH M. *et al.*, 2000[100]; MARK A. MEIER and PAUL J. LEE, 2009[97]).

The reflection and transmission coefficients study worked to verify which model would provide us with suitable amplitude reflection coefficients from the model bottom for P-wave and C-wave. This way, we were able to know how the coefficients vary with the angle of incidence, which give the correlation with offset.

The carbonate limestone shows shear modulus changes, from dry to brine saturation of up to 9%. Several laboratory studies have also reported shear-modulus changes between 5% and 20% from dry to water or brine saturation in carbonates corroborating with results found in this research.

The rock properties measurements were helpful for providing reliable results for the density, velocities and other features for the physical model and for the synthetics. It was also used to compute the median connected porosity of 21% pore space and to show that at high frequencies, ultrasonic lab measurements were affected by mechanisms operating at different frequency range and they were not entirely representative of velocities at seismic frequencies. Also, similar results to ours were found in the literature.

The converted-wave synthetic showed features that we should expect to see in the real data and were helpful to predict some of the signals, and the reflection and transmission coefficients study was important to make the choice and to be sure we would use a model with good signal contrast for the interest of reflections for the seismograms. Furthermore, the horizontal component revealed the anomaly structure in the final section showing that the methodology was successful.

Carbonate rocks are usually heterogeneous by nature, and the amount of heterogeneity found in the data is always a function of the Geophysical instrument used in the survey. As discussed in the Literature Review, carbonate rocks are also likely to be anisotropic due to fractures caused by tectonics or stress following deposition.

In this work, the leaking energy found in the crossline channel in Section 4.10 is not expected to appear at isotropic medium. Small energy at the crossline channel is normally regarded as a direct indication of azimuthal anisotropy. Converted-waves from the OBN ultrasonic experiment showed to have enough quality to image the dome structure and they are considered to be strong indicators of fractures properties that lead to fluid flow in petroleum reservoirs. Further investigations over the carbonate presented in this chapter are carried on in Chapter 5 by applying the algorithm developed in this work.

Chapter 5

The Computational Code and Workflow for Anisotropy Analysis of Vertically Fractured Media

5.1 Summary

Rotation of shear-wave horizontal components data is one of the key analysis procedure in the investigation of anisotropy caused by vertical fractures. Such analysis includes the description of azimuths of sets of fractures and the degree of anisotropy in the subsurface. The aims of this study are to present a computational code to perform anisotropy analysis of the shear wave, to validate it, and to apply the methodology for full azimuth multicomponent data. Full azimuth data from isotropic and anisotropic media sampled with $\Delta\theta = 10°$ are employed to validate the algorithm. The workflow is applied to the synthetic data where we were able to identify whether the data is azimuthal anisotropic or isotropic. S-waves are used to rotate source and receivers supplying information from sets of fractures as their azimuth with survey and the degree of anisotropy. The workflow has shown to work properly for the analysis, and the results are coherent with the model, showing the code's potential. During the validation, S-waves presented birefringence for survey not aligned with the main axes of symmetry in the medium. Converted-waves showed standard features such as the absence of energy at zero offset, polarity asymmetry around the source, and changes in polarity and phase after P-waves critical angle. Faster S-wave and C-wave from the anisotropic layer point to the direction of the sets of fractures in the hodogram. S-wave shows 10% of anisotropy while C-wave 6%, which are close values. On the code application for physical experimental

data, S-wave showed degree of anisotropy of 0.6% and confirmed the symmetry axes suggested by the converted-wave from the water-bottom experiment (4).

5.2 Introduction

Fractures are the most abundant visible structural feature in the Earth's crust and according to Narr et al. (2006)[46], *"all reservoirs should be considered as fractured unless proven otherwise"*. According to Liu and Martinez (2012)[3], stress field present in the rock plays a major role in the development of fractures. Earlier time and stress condition can cause fractures in the rock. In any of these cases, unequal horizontal stresses or fractures caused by them are common causes of azimuthal anisotropy.

In this chapter, a computational code for azimuthal anisotropy analysis is presented. The software performs a type of Alford Rotation that can be used for mis-tie correction in 2D lines. Full azimuth data generated in Chapter 3 are used to validate the code in the ability to indicate non azimuthal anisotropy and the computation of angle for rotation. Full azimuth physical modeling data are analyzed as application of this methodology.

The unpredictable data quality and mis-tie caused by azimuthal anisotropy cause serious difficulties in generating interpretable sections and using multicomponent data in lithology discrimination and fracture characterization (ALFORD, 1986)[13]. Alford suggested proposed rotation operators to transform 2C S-wave data into two principal sections containing the fast and slow modes. It is based on matrix rotation of sensors. After his work, several others were developed to deal with similar problems, such as source misalignment with receivers, analysis of the anisotropy in converted PS-waves, etc. (GAISER, 1999[12]; GAISER, 1997[69]; THOMSEN, 2001[68]).

5.3 Methodology

The anisotropy analysis source code ***analize***, which is a product of this work, contemplates the data preparation as well as input data visualization, Rose Wind and hodogram analysis, amplitude variation with rotation angle, geophone rotation, time difference between fast and slow shear-waves (S_f and S_s), amount of anisotropy and direction of fast shear-wave. The user has the choice of applying time shift for mis-tie correction and then the data is ready for processing.

The computational code will be validated using the anisotropic seismic data generated via computational modeling and the isotropic generated via the Reflectivity Method in Chapter 3. After validation, the code will be employed to look for anisotropy analysis of full-azimuth ultrasonic physical model data from the carbonate used in the Chapter 4. The presented methodology is applicable for estimating attributes of shear seismic data which presents azimuthal anisotropy.

5.3.1 The Algorithm

The algorithm is called ***analize*** which is a combination of the type of anisotropy caused by vertical fractures ***az***imuthal, the word ***an***isotropy itself and the name of the author ***Eli***ene. It is a self-contained sequence of actions to be performed over the seismic data to detect and analyse azimuthal anisotropy. Alford (1986)[13] has an excellent article where he presents the Alford Rotation method, and Thomsen (2001)[68] has developed his robust Alford type rotation called Vector Recomposition. In the Appendix A the reader will find the most important equations of their theory that was used for this work.

The software was coded in Python 3.6, which is a high-level, general-purpose programming language that can be applied to many different classes of problems. The language comes with a standard library that covers diverse areas of study. By programing in Python the computational code was made simpler and elegant in comparison with other non object-oriented languages. Graphic user interface (GUI) is currently under work.

Although ***analize*** provides several analysis steps through the visualization of graphs and computation of angles, amplitudes and energy, the two main products of the analysis are: the direction of sets of fractures and the degree of anisotropy caused by them. On the beginning of the program run, the geophysicist can preprocess the data via a number of steps, in order to select the traces and events of interest. The basic steps are summarized in Figure 5.1 and detailed as follows.

1. *Input.* The code can read data from any of the following formats: ASCII, excel or CSV. Isotropic or anisotropic data can be input.

2. *Data preparation.* The user can select one four-trace set ij (11, 12, 21 and 22) at the same azimuth or full azimuth four-trace ij. However, each four-trace set will be computed at the time. Figure 5.2 shows the optional output after reading a full-azimuth 2C data.

3. *Data visualization.* In this step, seismograms can be outputted in any of the
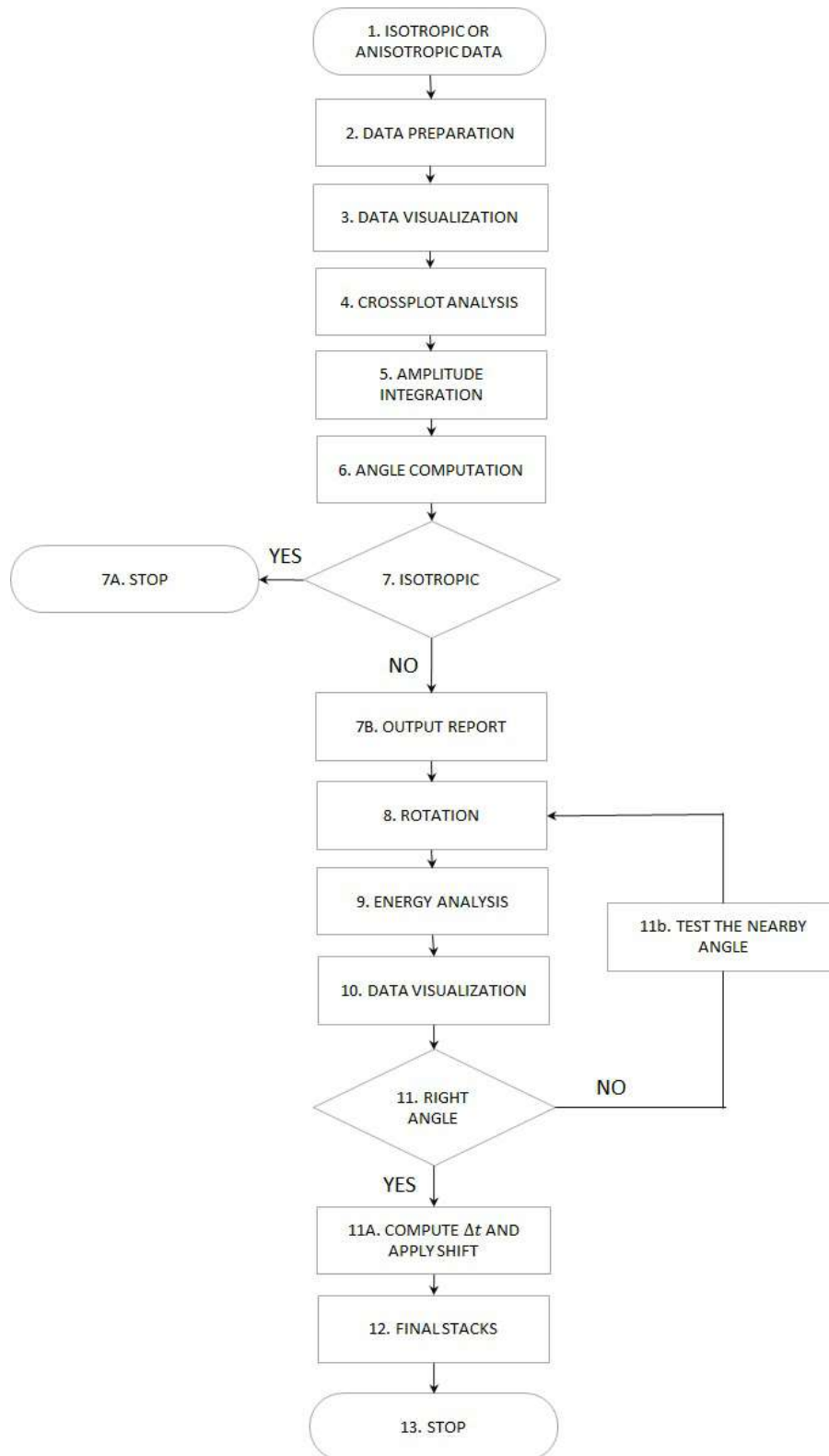
Figure 5.1: Algorithm of *analize*.

following forms: Four-trace ij and four seismogram sections with all azimuths. Figures 5.3 and 5.4 show an example of four-trace ij plot.

4. *Crossplot analysis.* Hodograms (crossplots) are outputted to show direction of

Figure 5.2: Reading and preparing the data.
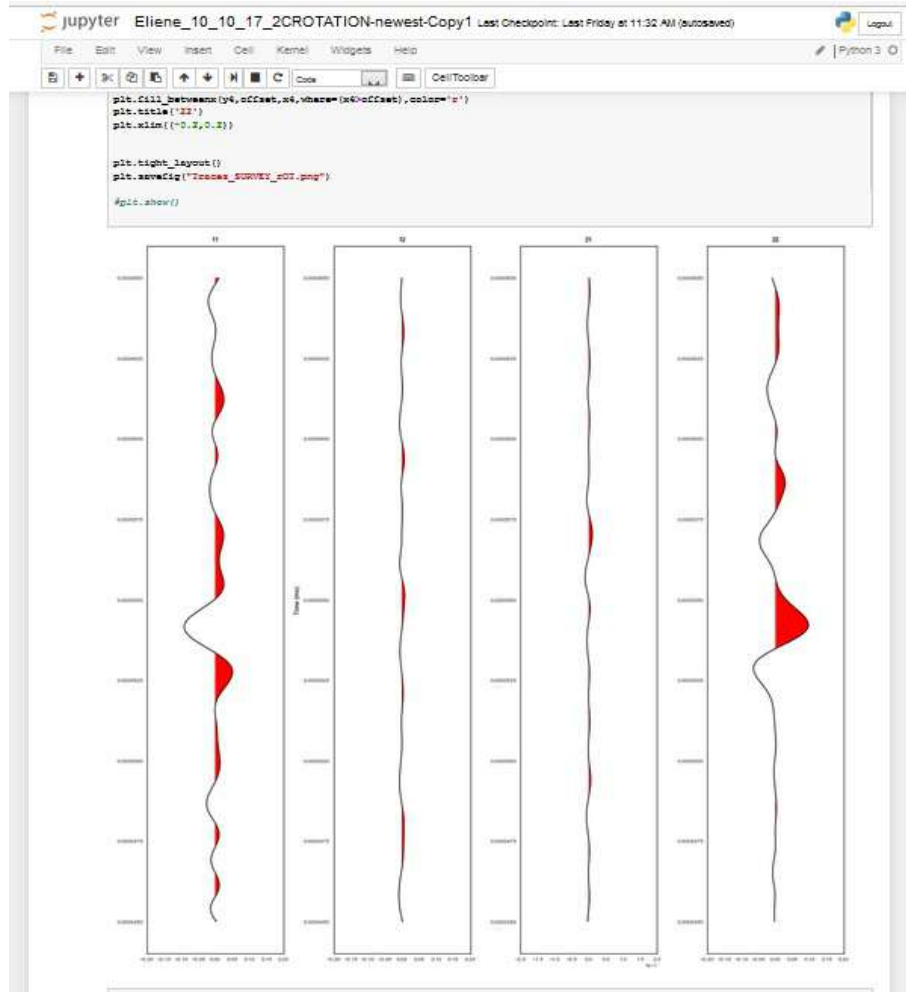
Figure 5.3: A set of four traces ij.

particle motion. The user has the choice to use linear regression to see tendency and other statistical analysis. The user has several types of hodograms available to output and analyze. Two examples are showed below.

One of the most convenient way to take a quick look at a univariate distribution is by building a pair plot. The pair plot shows crossplots. The major correlations are at diagonal (ij, where $i = j$) and other correlations lower with density, kernel density estimate (KDE). The last will plot the bivariate den-
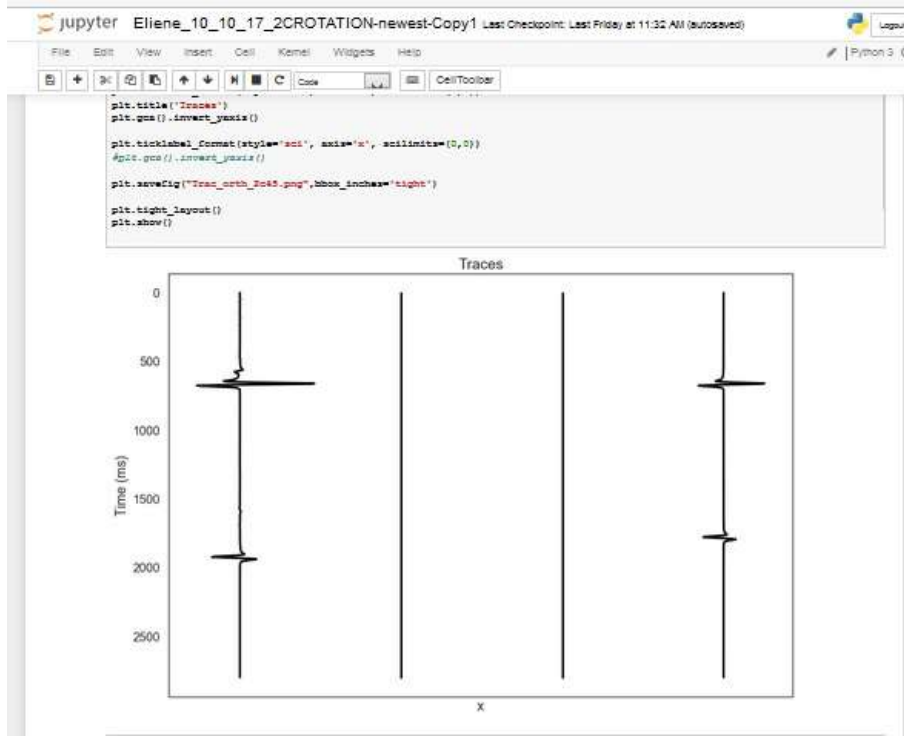
Figure 5.4: A set of four traces ij.

sity which shows how much one data is correlated to the other through the covariance matrix showed in Equations 5.1 and 5.2 (MathGo, 2006[101]).

$$f(x,y) = \frac{1}{2\pi\sigma_x\sigma_x\sqrt{1-D^2}}exp^{-1/2Q(x,y)} \tag{5.1}$$

$$\Sigma = \begin{bmatrix} \sigma_x^2 & D\sigma_x\sigma_y \\ D\sigma_x\sigma_y & \sigma_x^2 \end{bmatrix} \tag{5.2}$$

where Q is the quadratic form (MathGo, 2006). The parameters satisfy -1 < D > 1, $\sigma_x^2 > 0$ and $\sigma_x^2 > 0$. Correlation r is the statistical relationships between useful reference for how much correlated a seismic trace is with the other.

Pearson's coefficient, shown on the bottom plots are a measure of the strength and direction of the linear relationship between two variables that is defined as the (sample) covariance of the variables divided by the product of their (sample) standard deviations. It has a value between +1 and -1, where 1 is total positive linear correlation, 0 is no linear correlation, and -1 is total negative linear correlation. That is why it is useful to tell how correlated signals are.

By default, this will draw a histogram and fit a kernel density estimate. In

Figure 5.5 there is a single hodogram where components 11 and 22 are cross-splotted and a linear curve is fitted with correlation shown in the graph r = -0.14.
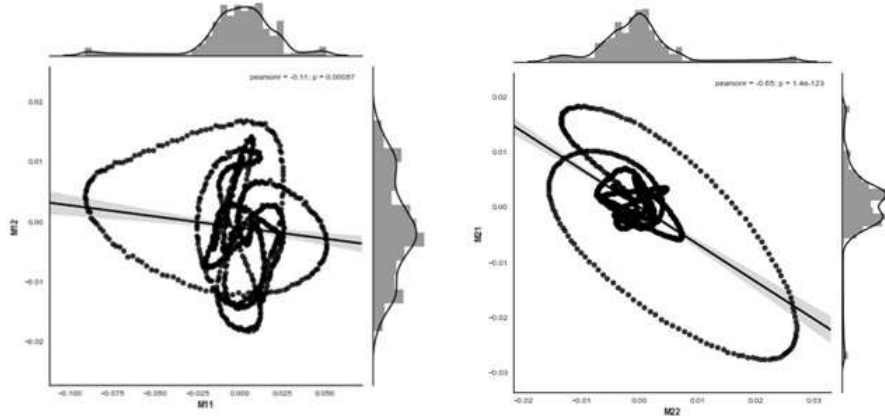
Figure 5.5: Cross plot with linear fit.

Displayed in Figure 5.5 there is a pair plot produced by **_analize_** showing features explained above.
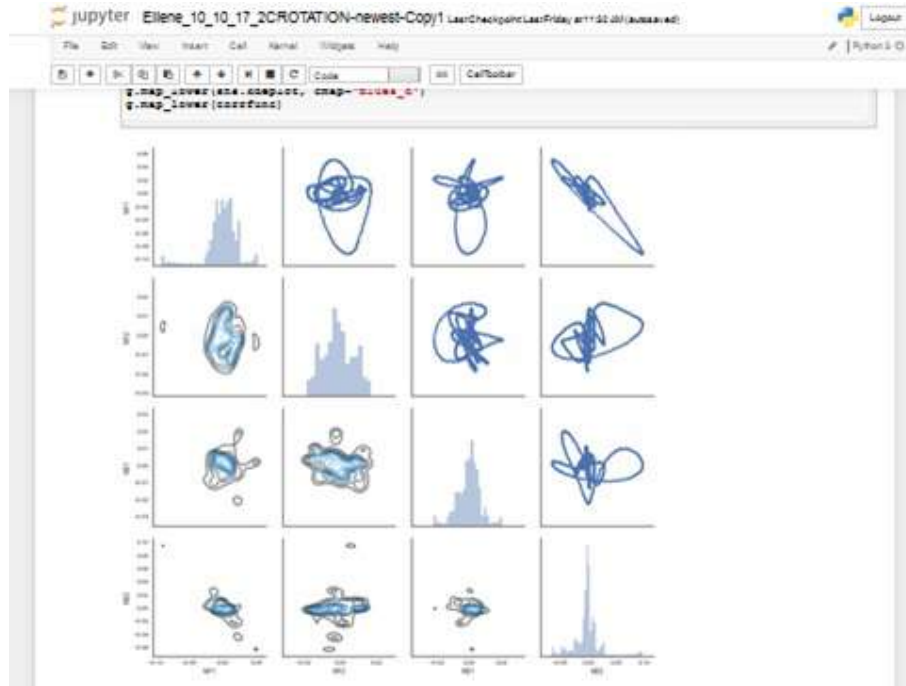
Figure 5.6: Pair plot with crossplots upper, distplots in the diagonal and KDE plots lower.

5. *Amplitude integration.* If the user prefer to work with energy rather than amplitude, the code performs an integration of amplitude over the time for energy and diagram analysis.

6. *Angle computation.* For this routine, the following information should be in-
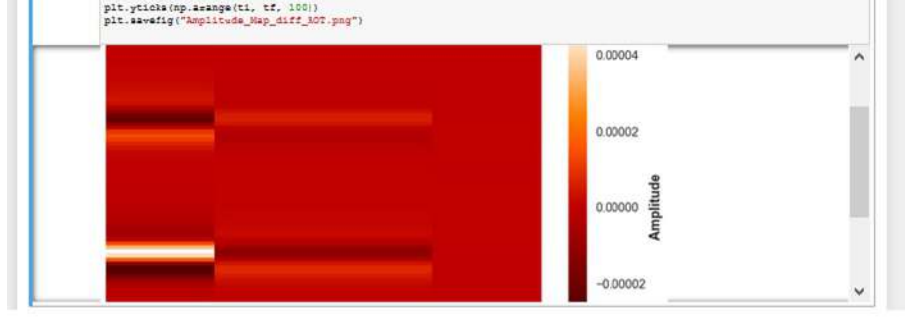
Figure 5.7: Energy map shown the traces with most enegy.

put: α and β angles between source polarizations and receiver polarizations, respectively; angle-step to perform the geophone rotation iterations over $0°$ to $359°$. The output is a graph that contains the maximum amplitude *versus* angle.

7. *Decision 1 - isotropic or azimuthally anisotropic.* By the analysis of the so far computed values the user is able to say if the data is azimuthally anisotropic or isotropic. If isotropic, follow to step *7.A* and stop. If not, follow to *7.B*.

> 7B. *Output Report.* **analize** is able to output a report with the angles that match the four following requirements: maximize the inline (ii and jj) and minimize the offline (ij, ji) amplitudes. The user can confirm that the computed angle is reliable because each of the conditions are obtained separately and they should show the same angle.

8. *Rotation.* Now the user can confidently rotate the geophone (and source if needed) to compute the new set of traces.

9. *Energy analysis.* Analysis of energy maps and rose diagrams are used for quality control.

10. *Data visualization.* New four traces are outputted after rotation in any of the following forms: four seismogram sections with all azimuths; or CMP gathers.

11. *Decision 2 - Right angle or not.* If that is the right angle the user can go ahead. If not, he might want to try a nearby angle or to use a shorter angle-step in the computation, following to step *11.B*.

> 11A. *Quantitative analysis.* The code determines the shift between S_f and S_s (Δt) and leaves the option for the user to apply it.

12. *Final Stacks.* Output final traces.

13. *Stop.* That is the end. **analize** outputs the main direction of the set of vertical

fractures (or axis of anisotropy in the medium) and the degree of anisotropy. Then, the data is ready to further processing for imaging.

In case there are many seismic series in the file, the code reads the full file and the user can choose which traces will be used for each analysis. Data is plotted and windowed according to the time window where S-wave is placed. After windowing, data is plotted again so that the user can be sure the window contains the wavelets of the reflected event. Next analysis is to output the arrival time at inline traces and the amount of energy in the chosen window.

The full azimuth angle routine computes the amplitudes of the data over 360 angles and outputs it graphically. The *maxamp* routine computes the maximum amplitude values for the inline traces and minimum amplitude values for the offline traces and outputs the angles where it happens. Any of them can be used to rotate the data.

In case there is a real data it might have some sort of noise or the layers can be heterogeneous, therefore, the angle computation might be susceptible to slight deviations because of the influence of those factors. Besides, depending upon the angular resolution of the calculation (angle step) set by the user, it might not zero the energy offline due to the inexactness of the angle sample. In any case, the approximation may be improved by testing nearby angles.

5.3.2   Validation

In this section the computational code will be validated, *i. e.* its ability to compute the angle of the fractures for rotation and to identify whether there is azimuthal anisotropy or not will be tested. Two seismic data generated via computational modeling, one isotropic and the other anisotropic with vertical fractures (Chapter 3), are used to validate ***analize***. Since the sets of fractures are well known, we will be able to evaluate the code performance.

For the anisotropic data, consider the second layer in the model with fracture azimuths as presented in Figure 5.8. This figure was already presented in Chapter 2, but it is adapted for the understanding of the hereby presented analysis.

Validating the Computation of the Angle for Rotation

To validate the ability of the code to detect anisotropy and compute the right angle for rotation, this section will apply the workflow-algorithm to the Mesaverde
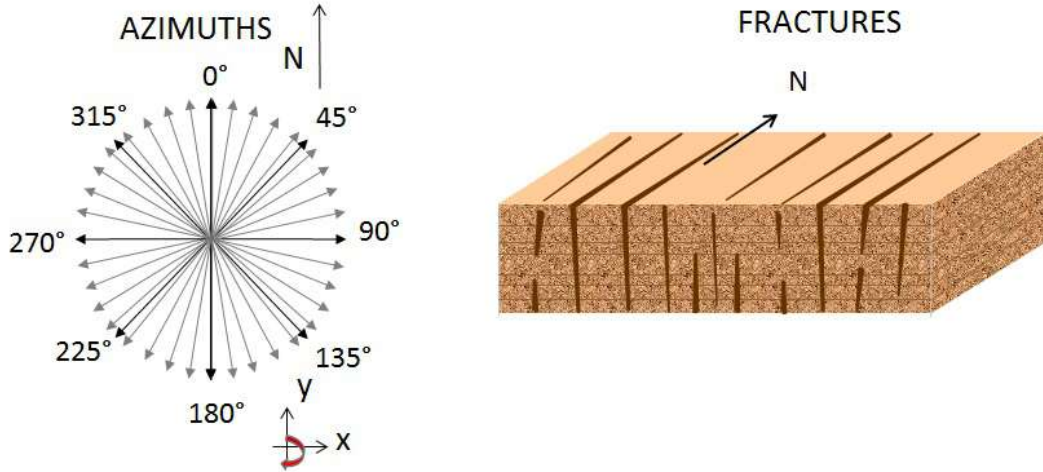
Figure 5.8: The vertically fractured layer and fracture alignment with North 0°. Axes x and y are directions of geophones and they rotate clockwise.

data that is anisotropic due to its vertical fractures (see Figure 5.8 and Table 3.4). In case the overburden is anisotropic there is S_H mode and S-wave splitting (see Figure 2.5 and results in Figures 3.24 and 3.28) (ALFORD, 1986[13]; THOMSEN, 1986[5]; LIU & MARTINEZ, 2012[3]).

Therefore the code should compute angles that show the main axes of symmetry in the medium. Also, rose diagram plots should point the maximum energy directions and there should be changes in amplitude when data is rotated via computed angles. The final seismograms should show inline with higher energy and offline with lower to zero energy, so that other processing steps can be done with the inline data (Bale, 2009)[4]. In addition, the two inline sections should show different S-wave arrival times. That difference in time indicates that there is a faster direction for the propagation of S-wave, and that anisotropy attributes can be computed from the data.

Preliminary Analysis

According to Alford (1986)[13]:

> "In an azimuthally anisotropic elastic medium, given a direction of propagation, there are two distinct velocities at which a S-wave can propagate, with two distinct orthogonal polarizations. If the incident polarization conforms to one of the preferred directions, e.g., either parallel or perpendicular to the unique axis, energy simply propagates at the appropriate velocity. If the polarization of the incident wave does not correspond to one of the preferred natural directions, motion of the incident wave is vectorialy resolved along the natural axes and the situation becomes more complicated" (p. 477).

Displayed in Figure 5.9 is a matrix of 4 stacked sections outputted by *analize*, which result from processing the inline and crossline components for inline (S_V) and crossline (S_H) horizontal sources. Each trace is at 180 m offset in the survey. Notice that in Figure 5.9, (a) is 11, (b) is 12, (c) is 21 and (d) is 22 directions presented in Chapter 3. On the graphic, y axis is time in seconds and x axis is a trace at each 10° azimuth with fractures (see Figure 5.8).
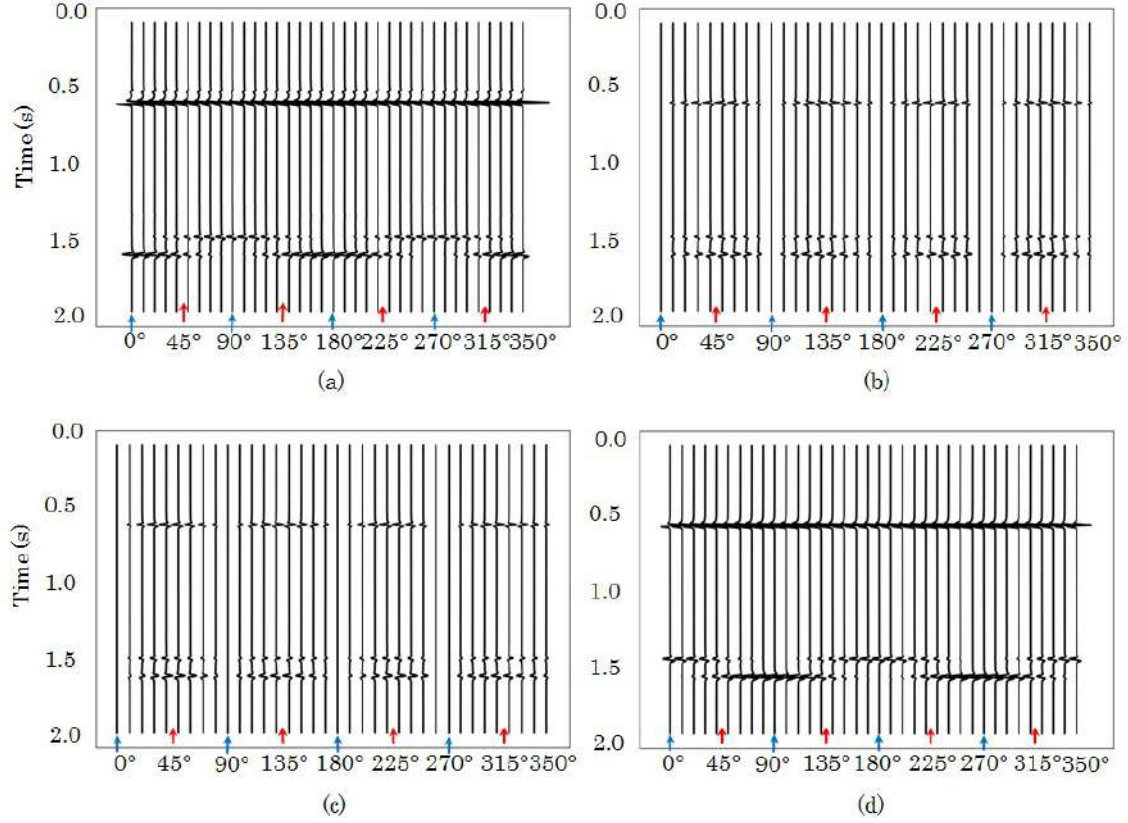
Figure 5.9: Full-azimuth 2C data. The inline are shown in (a) 11 and (d) 22. The offline are shown in (b) 12 and (c) 21. Blue arrows point to each 90° parallel or perpendicular to fractures and red arrows point to each 45° with fractures.

First event around 0.6 s at each synthetic is the SS reflection above the anisotropic interface. Second event around 1.4 s is the SS reflection from the bottom of the anisotropic interface. The energy from the second event has traveled through the anisotropic medium suffering changes due to the anisotropy. The reader might want to compare it with event in Figure 2.7.

In the Figure 5.9, blue arrows point to directions aligned with fractures or perpendicular to them. Red arrows point to the intermediate angles between each pair of those directions (parallel and perpendicular). Source polarization x and receiver x are presented in Figure 5.9 (a). First event is continuous and the second event presents azimuthal variations. At $\theta = 0°$ and 180° the S-wave arrives later than at $\theta = 90°$ and 270°. Transition zones with fast and slow waves are noticeable

120

at each $\theta = 45°$ with fractures.

Source polarization x and receiver y are shown in Figure 5.9 (b). First event already shows azimuthal variations as zero amplitude for $\theta = 0°$, $90°$, $180°$ and $270°$ and polarity inversion at each $90°$. The second event presents zero amplitude for the same angles as the first event. At intermediate angles such as $\theta = 45°$, $135°$, $225°$ and $315°$, two S-wave arrivals are registered delayed in time, one with positive amplitude and the other with negative amplitude. Polarity inversions are registered for them.

Source polarization y and receiver x are shown in Figure 5.9 (c). This synthetic has the same features as the ones found in Figure 5.9 (b). Finally, source polarization y receiver y is shown in Figure 5.9 (d). This synthetic shares similar features with Figure 5.9 (a), but at angles where pure S_f appears for (a) there is no S_f, but pure S_s and *vice-versa*. From the synthetics a mismatch is clearly seen on the second event.

Azimuthal variations at the first event in the offline synthetics suggest S-wave splitting to happen just by the wave touch at the top of the anisotropic layer, confirming the observed at hodograms in Figure 3.28. The second event at the offline synthetic seismograms presented polarity reversals about the symmetry planes. As it has been said before, that is the key element for recognizing a horizontally transverse isotropic system: $90°$ polarity reversal across fracture strikes. The second event at Figures 5.9 (a) and (d) have no polarity inversion with azimuth as Figures 5.9 (b) and (C) do.

At $\theta = 45°$, $135°$, $225°$ and $315°$, energy from any S-wave source is polarized in both directions (parallel and perpendicular to fractures) presenting the features seen at the offline synthetics. The absence of data at azimuths parallel and perpendicular to fractures for synthetics offline (Figures 5.9 (c) and (d)) happens because the wave is polarized in both directions (parallel and perpendicular to fractures) and source and receivers are aligned with those directions ($\frac{n}{2}\pi$ with n integer). Then, there is no energy left offline for such angles.

The dynamic mis-tie between the inline sections is clearly visible. Correlation between events on the two sections is obvious. However, the events on the right section are progressively delayed and they need to be corrected to improve data quality for further steps in the seismic processing. Such procedure is specially interesting to know the main direction of fractures in the medium and the degree of anisotropy in the layer under study.

Correction of the Energy in the Acquisition Data

Figure 5.10 is produced by picking a quartet of traces at a constant azimuth (45° in this case), representing each one of the components (11, 12, 21 and 22) from Figure 5.9. Synthetics show S-wave splitting.
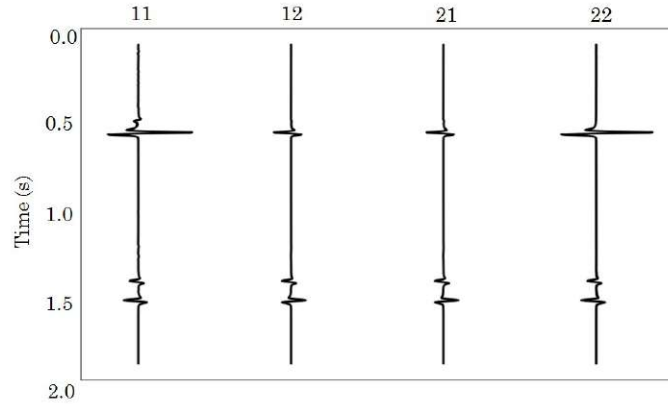
Figure 5.10: Traces 11, 12, 21 and 22. Survey is 45° with fractures.

According to Figure 5.10, the event from the second interface, which have traveled through the fractures at layer 2, arrives first at the panel 22 (SS2^f) and later on panel 11 (SS2^s). One can clearly see energy at offline receivers (12 and 21) which are converted SS waves. At t = 0.66 s (or around it) there is the S-wave reflection from the first interface. Close to t = 1.4 - 1.5 s there is the S-wave from the second interface, which has traveled through the fractured layer.

analize uses an Alford rotation type method to compute the angle that correct the data from the mis-tie. Inputs are angles between source and receiver, the number of angles that you want to rotate the geophone to test, and the windowed four pairs of traces at the same azimuth in the survey.

Notice that all angles are computed, in the way that combinations of maximum great and lower amplitudes are shown, but they are all the maximum amplitudes at each trace rotated by a specific angle. For each four-trace ij at a certain azimuth θ the algorithm will give the answer according to the azimuth with fractures. In other words, the rotation should be performed according to the azimuth of that direction with fractures.

Since the scale of the displayed data might hamper very low amplitudes in the seismogram, this algorithm computes a map of energy and outputs it in the form of a color map for the user to better analyze the energy. Figure 5.11 shows the output graph that computes the angles of geophone rotation versus amplitude (source is previously rotated if needed to line up with receivers).

After computing the graph shown in Figure 5.11, the code also outputs the angles that best meet the requirements. Those requirements are maximum amplitude
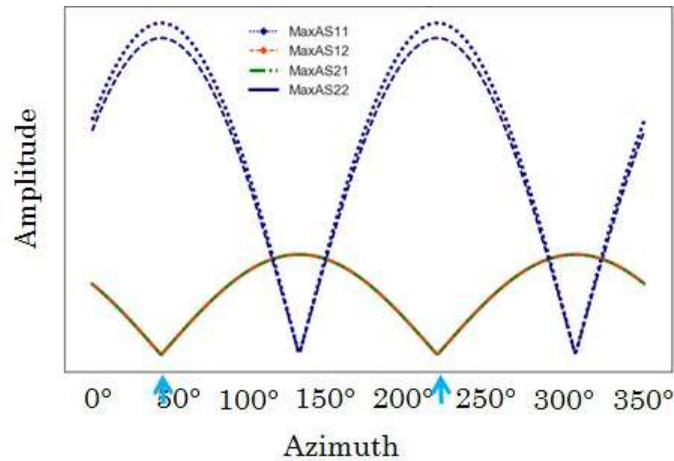
Figure 5.11: Angles of geophone rotation varying with the maximum absolute amplitude. Angle sampling = 10°. Cyan arrows point to the angles that maximize inline energy.

inline (11 and 22) and minimum amplitude offline (12 and 21). These conditions are fulfilled independently in theta. The report is showed in Figure 5.12 on the left and the requirements on the right. Notice that all the four requirements are mutually satisfied pointing to the same angle, approximately 45°.
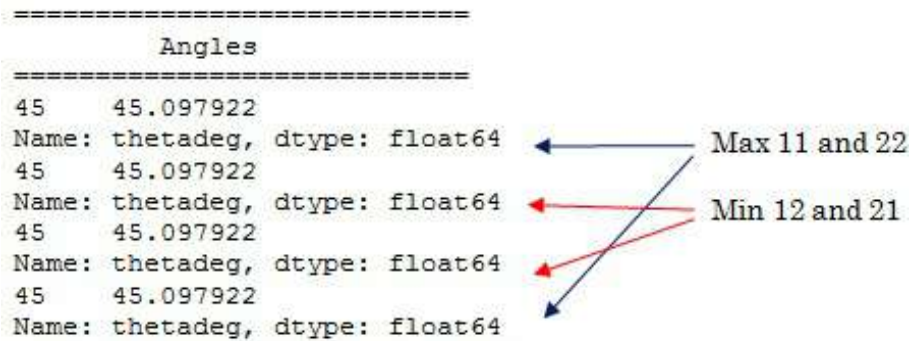
Figure 5.12: Report (on the left) lists the angles that satisfies the requirements (on the right).

Figures 5.13 and 5.14 work for quality control after geophone rotation. Figure 5.13 is the energy map over the windowed trace (1.30 - 1.70 s) after rotation showing that the offline (centered) are zero energy and the inline (both lateral) had their energy maximized. In the case of real data, the offline energy should be minimized, but some noise will be seen.

In Figure 5.14 rose diagrams show energy in all directions taken from each pair ij. On the top left there is 11, on the top right there is 12, on the bottom left there is 21 and on the bottom right there is 22. Those rose diagrams show high energy at the inline according to the source orientation. Energy offline is lower and increases at
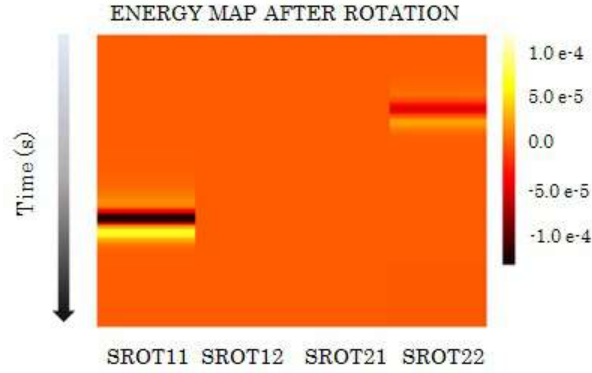
Figure 5.13: Energy map after rotation. Axis y is time and axis x are traces ij and their energy.

45° on every quadrant. They are useful for anisotropy analysis and quality control.
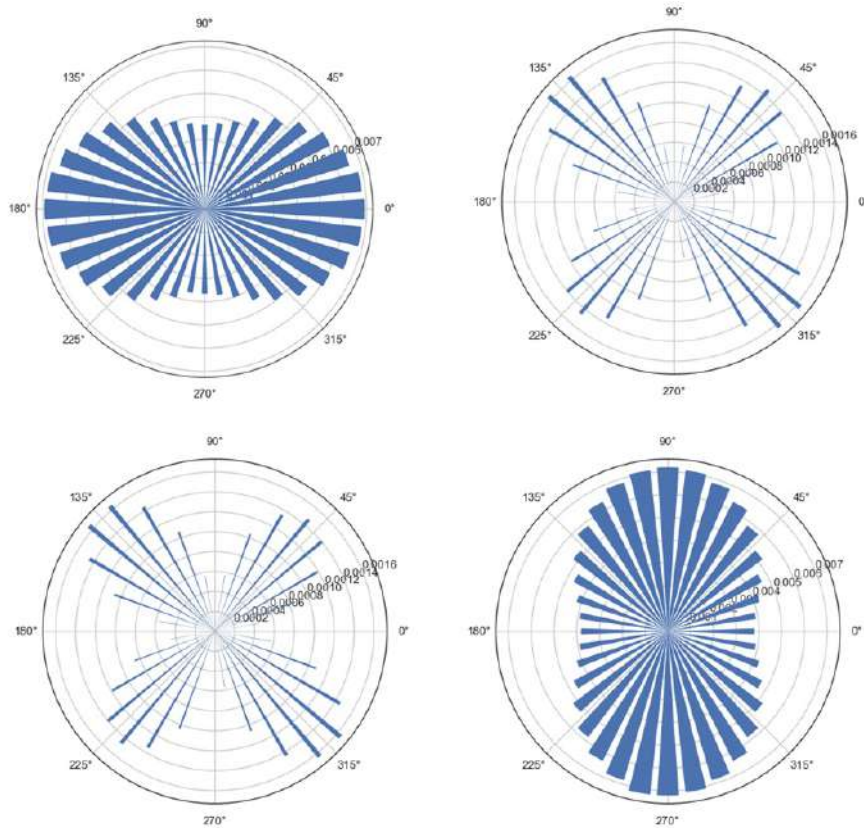
Figure 5.14: Rose diagram after rotation show the energy with azimuth.

Figure 5.15 shows amplitude variation with angle for 11 on the top and 22 on the bottom. Notice the inverse correlation between them. Besides, main axes of symmetry in the anisotropic layer are clearly presented in the analysis, confirming the prior computations.

Figure 5.16 shows the data after rotation. The two S-waves are now with their energy concentrated inline and the shift is clearly visible there. A time shift can be

Figure 5.15: Angle of polarization versus amplitude show azimuthal variations. On the top, 11, and on the bottom 22 data.

applied to the data for next steps in processing for imaging, so that each S-wave will be at the same level in time.
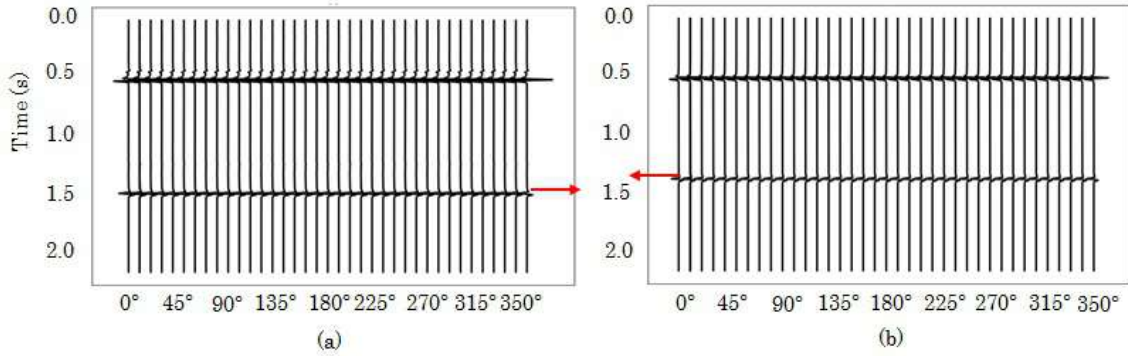
Figure 5.16: Comparison of synthesized sections conforming to natural system of coordinates. Data is optimally rotated for each trace. Time window contemplates the two events: the one from the top of the anisotropic layer and the one from its bottom.

Two examples of other survey angles (with fractures), 30° and 100°, are seen in Figure 5.17. There, the output computed set of amplitudes for angles are showed for $\theta = 30°$ on the top and for $\theta = 100°$ on the bottom. Cyan arrows point to 30° and 210° on the top graph and they point to 100° and 280° on the bottom graph. Those are the main axes of anisotropy in the medium seen from the position of the survey azimuth, confirming the reliability of the algorithm's answer.

Presented in Figure 5.18 there are the two sets of pair plots for the analysis presented in Figure 5.12. In (a) the pair plot is from data at 30° azimuth with

125
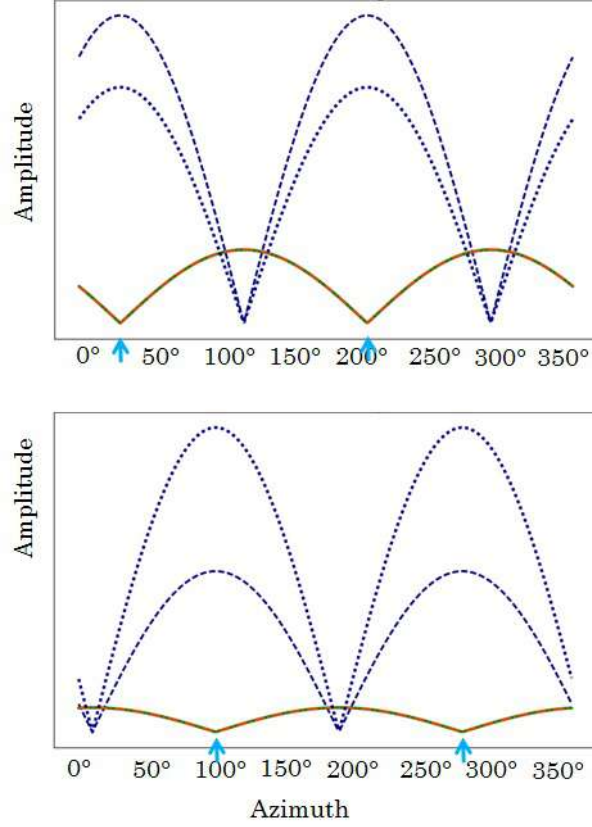
Figure 5.17: Output maximum absolute amplitude for 30° with fractures (on the top) and for 100° (on the bottom). Angle sampling = 10°.

fractures and in (b) it is 100° azimuth.

In case of azimuthal anisotropy with neglectable level of heterogeneity rotation at the right angle should bring the energy at offline traces closer to zero and energy at inline traces should increase. ***analize*** showed to be powerful in computing the angle that corrects the traces in the sections. ***analize*** also produced quality control and adequately apply the shift by correlation between the S-waves. The valuable information was obtained and the data is ready for next step procedures.

Validating the Ability to Obtain Δt between t_{S_f} and t_{S_s}

Consider the survey rotated clockwise 45° from the fracture alignment. Figure 5.19 shows the events at seismograms 11 and 22 over plotted at the windowed with their arrival times are indicated by arrows. Since there is a faster speed direction that is not aligned with the survey, there will happen conversions from S_V to S_H and the other way around. S-waves split into two at the second interface with orthogonal polarizations as expected.

As one could see in the anisotropic modeling presented in Chapter 3 and also
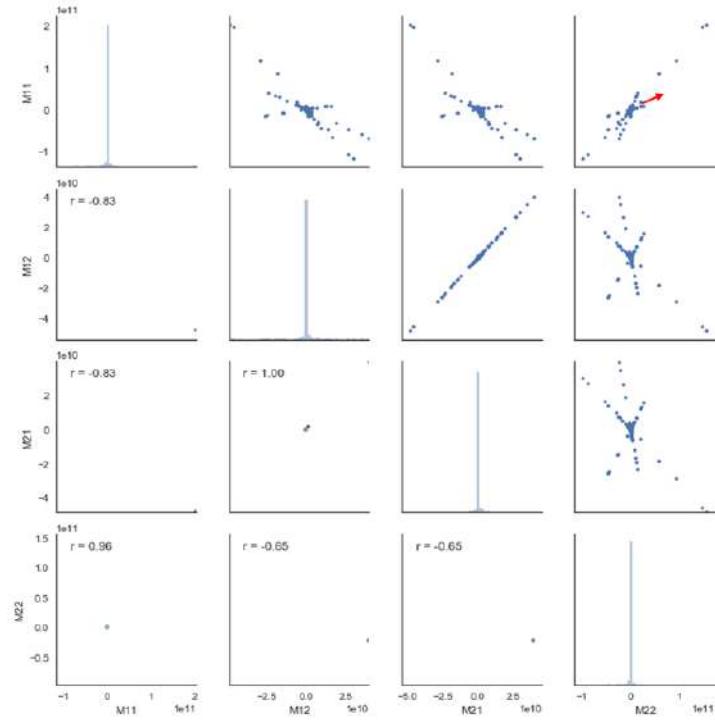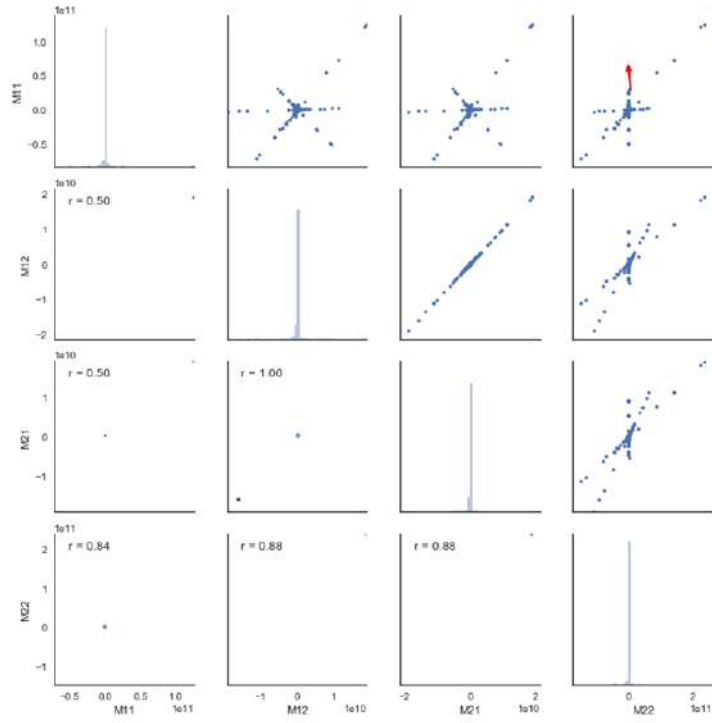
Figure 5.18: Two sets of pairplots are showed. In (a) the pair plot is from data at 30° and in (b) 100° with fractures. Each set of pairplot shows crossplots upper, major correlation at diagonal (ij, where i = j) and other KDE correlations lower.

in the last section, S-wave from the second interface arrives at two different times with different amounts of energy depending on the azimuth, and both can be seen at
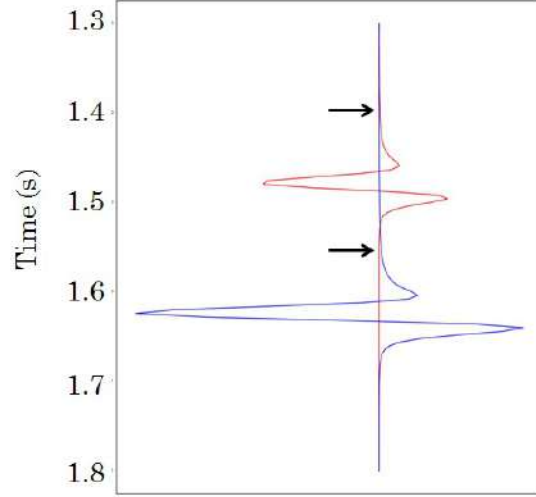
Figure 5.19: Comparison between traces 11 and 22 windowed for reflection from the second interface at 0° shown in blue $t_{S^s} = 1.53$ s and in red $t_{Sf} = 1.38$ s.

any angle different from $n\pi/2$ (for n integer)(see Figures 3.21 and 3.23). SS2 clearly presents the S-wave spitting and the delay in time seems to decrease with offset in the seismogram.

The arrival time of S_f is $t_{S^s} = 1.38$ s and $t_{Sf} = 1.53$ s for S_s. Since $\Delta_t = 0.15$ s, the density of anisotropy in the second layer is computed by $\gamma^{(s)} = (V^s - V^f)/V^s$ resulting in $\gamma^{(s)} \approx 0.10$, or 10% of anisotropy (TSVANKIN & GRECHKA, 2011[61]).

Consider PS^f the fast C-wave and PS^s the slower. Their amplitude variation with azimuth is shown in Figure 5.20. Figure 5.22 shows survey rotated 45° with fractures where trace 32 in orange (second event points to left) over trace 31 in blue (second event points to right).

Displayed in Figure 5.21 there are 31 (PS_x) and 32 (PS_y) for all azimuths with $\Delta\theta = 10°$. The PS_x is showed in (a) where first event is continuous and the C-wave event has lower amplitude and presents azimuthal variations. At $\theta = 0°$ and 180° the S-wave arrives later than at $\theta = 90°$ and 270°. Transition zones with fast and slow waves are noticeable at each $\theta = 45°$ with fractures. Reader should refer to Figure 5.9 (a) and (c) and notice similarities.

In Figure 5.21 (b) PS_y the first event already shows azimuthal variations as zero amplitude for $\theta = 0°$, 90°, 180° and 270° and polarity inversion at each 90°. The second event presents zero amplitude for the same angles as the first event. At intermediate angles such as $\theta = 45°$, 135°, 225° and 315°, two S-wave arrivals are registered delayed in time, one with positive amplitude and the other with negative amplitude. Polarity inversions are registered for them. Reader should refer to Figure 5.9 (b) and (d) and notice similarities.
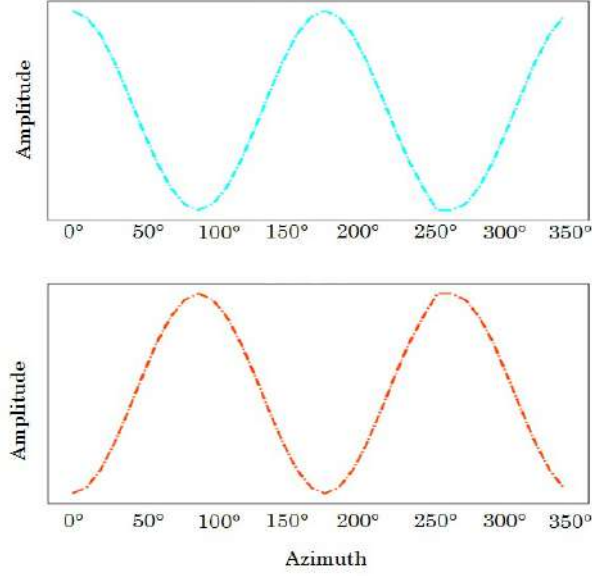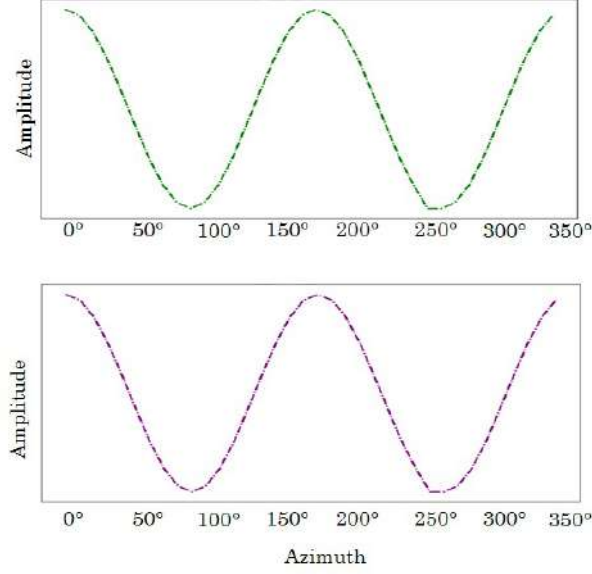
Figure 5.20: Angle of polarization versus amplitude show azimuthal variations. On the top, 31, and on the bottom 32 data.
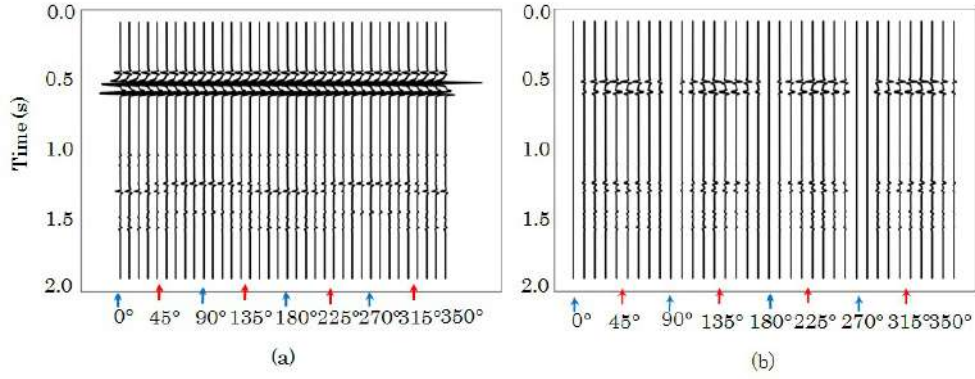
Figure 5.21: Full-azimuth C-wave P- to S-wave data. In (a) 31 shows P to S_x and in (b) 32 shoes P to S_y. Blue arrows point to each 90° parallel or perpendicular to fractures and red arrows point to each 45° with fractures.

The arrival time shown in Figure 5.22 for PS^f is $tPS^f = 1.08$ s and for PS^s is $tPS^s = 1.15$ s, then the delay in time between fast and slow C-wave is $\Delta_t = 0.07$ s. Then, $\gamma^{(ps)} = 0.06$ resulting in 6.0% of anisotropy.

Since C-wave has split and traveled just half the way in the anisotropic medium as a S-wave, increasing Δt during half the way, it should really have lower value of anisotropy. C-wave proved to be powerful in giving a reliable estimate of the degree of anisotropy in the rock since it presented 6% of anisotropy, which is 60% of the S-wave anisotropy.

Since the computation of the degree of anisotropy can be done via the C_{ij} coefficients also and the author has computed C_{ij} for modeling, confidence of the degree of anisotropy found in this analysis can be tested. According to Tsvankin
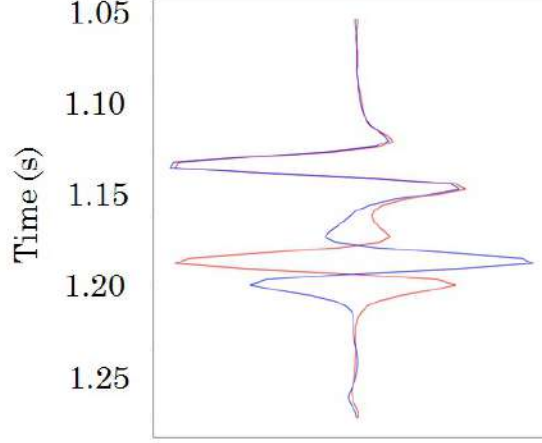
Figure 5.22: Comparison between traces 31 (orange line points to left) and 32 (blue line points to right) windowed for reflection from the second interface at $45°$ show in blue $t_{PSf} = 1.10$ s and in red $t_{PS^s} = 1.16$ s.

and Grechka (2011)[61] the relationship between $\gamma^{(s)}$ and C_{ij} is given in Equation 5.3. Then, computing $\gamma^{(s)}$ again and calling it by the name with a marker of Cij, the result is $\gamma^{(s)}_{Cij} = 6.5$ %. Comparing $\gamma^{(s)}_{Cij}$ with $\gamma^{(s)}$ the difference is considerably small.

$$\gamma^{(s)}_{Cij} = \frac{C_{44} - C_{55}}{2C_{55}} \qquad (5.3)$$

The equation to compute the degree of anisotropy for S-wave considers the time delay between S-fast and S-slow. It is expected that C-wave does not show the same amount of anisotropy as S-wave. Since C-wave is P- to S-wave by nature, the wave becomes S-wave for half of the way. Then, about 50% of the delay in time is registered. Also, the computation takes into consideration the arrival time to the S-wave slower to divide the Δt, inserting the effect of P-wave velocity in the computation. The arrival time of a C-wave is lower than the arrival time of a S-wave. Then, the division by a minor number makes the amount of anisotropy slightly greater than 50% of the S-wave anisotropy.

How about the situation in which the user analyzes an isotropic media? The code is ready for the challenge of showing axes that proves that the data is isotropic, as it will be showed in next subsection.

Validating the Ability to detect Isotropy

To validate the ability of the code to detect whether there are vertical fractures or not, this section will apply the workflow to the isotropic data and compute the

possible angle of rotation to compare it to the anisotropic data.

Isotropic Data Analysis

If source and receiver are lined up ($\alpha = 0$ and $\beta = 90°$), an isotropic full azimuth seismic survey 2Cx2C has the same appearance that the four seismogram shown in Figure 5.23 (traces at the same offset very close to the source). This Figure corresponds to a medium that shares the same properties than the one presented above, but has no vertical fractures nor any other type of anisotropy. The first event is the S-wave reflection from the first interface and the second event os the S-wave reflection from the second interface. As there is source S_V and S_H, there is signal over the main seismograms, over the inline.
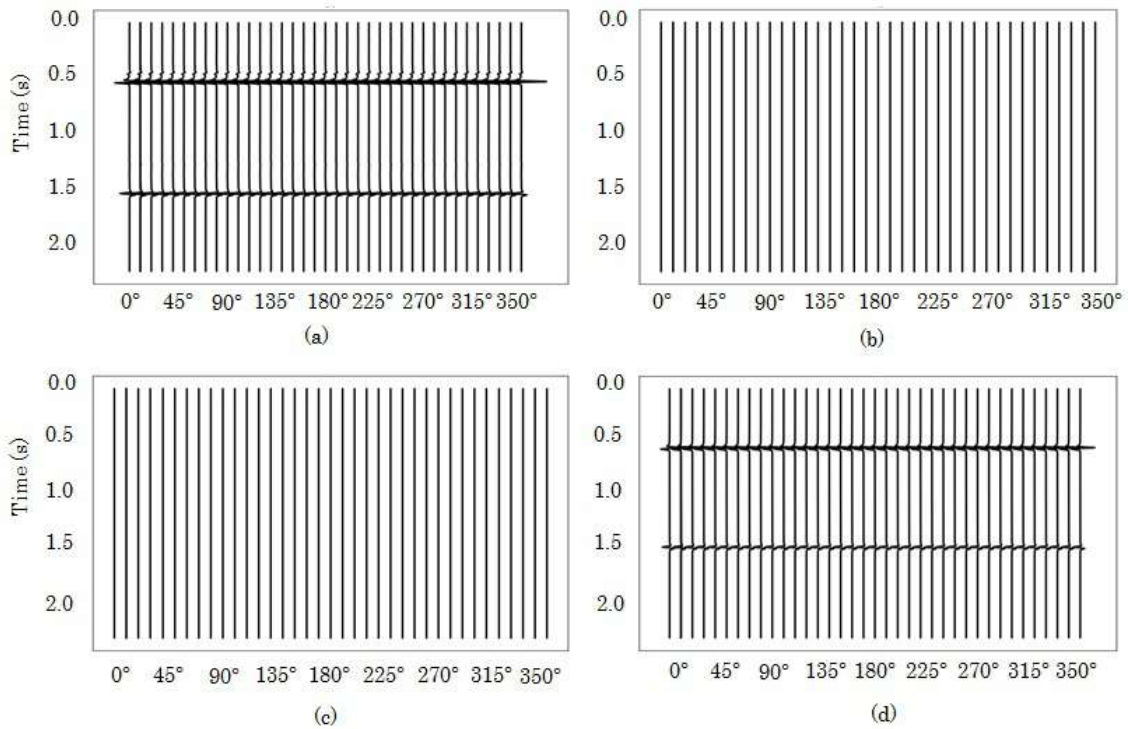
Figure 5.23: Full-azimuth data over isotropic layers. Angle sampling $= 10°$. The inline are shown in (a) 11 and (d) 22. The offline are shown in (b) 12 and (c) 21.

Features seen in the isotropic seismograms are pretty close to the ones seen after geophone rotation. As there are no differences in the stress field and there are no heterogeneity, the S-wave velocity is the same for any direction in the azimuth. There is no splitting and no energy offline, as said before (see Figure 2.5). The user can look at the seismograms and already know that the medium is isotropic.

In any case, if there is no azimuthal anisotropy, the code still computes amplitude variation with angles and outputs a graph with maximum amplitude constant with angle. If the medium is isotropic, the outputs will point to $\theta = 0°$. If it is

accomplished, the coding coherency of the algorithm with reality and its robustness will be proven for azimuthal anisotropy detection.

Displayed in Figure 5.24 there is the azimuth θ on axis x and the maximum amplitude of each pair ij on axis y. Notice that the amplitude for offline synthetics are null for any azimuth (orange and green lines). Angles that maximize the amplitude inline are exactly the angles aligned with $\theta = \frac{n}{2}\pi$ with n integer.
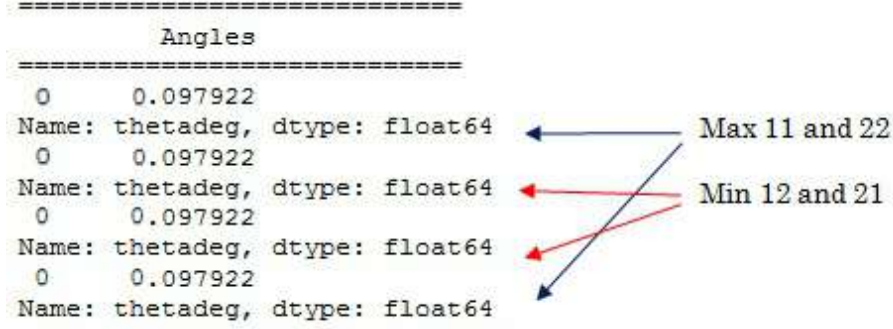
Figure 5.24: Report shows the angles of rotation to align the survey with natural coordinate system in the medium attending to four requirements.

For any four-trace data the result will be similar (one trace like each of the panels), emphasizing that there is no anisotropy. **analize** have shown to be very useful in helping to detect isotropy or vertical fractures. The next step is to apply the software to analyze a physical modeled data, since it holds features closer to real data.

5.4   Applications

In Chapter 4, PS-wave data at the OBN experiment showed indicators of azimuthal anisotropy. According to Vetri et al. (2003)[43], carbonates are frequently fractured. Schulte and Edelman (1988)[15] state that considering azimuthal anisotropy is a good approach for dealing with multicomponent S-wave data. Therefore, employing **analize** as a tool for investigating anisotropy in the carbonate is highly recommended.

A sample of the carbonate tested in Chapter 4 was used to perform a wide azimuth survey with angles from 0 to 180°. The dimensions of the carbonatic sample are $L_x = 153.40mm$, $L_{y,average} = 55mm$ (from 48 to 62 mm) and $L_z = 58.40mm$. S- transducers used in the experiment have 500 kHz of central frequency as well as diameter of 1.0 inch (25.4 mm).

The experimental wide azimuth data are presented in Figure 5.25 with their azimuth in the x axis. Data presents variations in arrival time as well as split of S-wave, demanding detailed investigation of the rock.
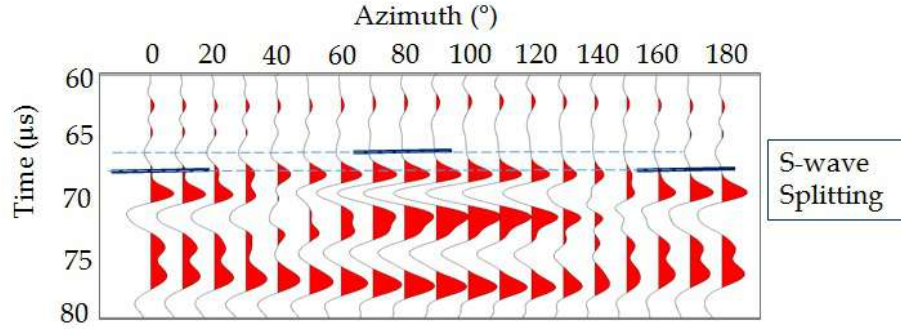
Figure 5.25: S-wave split.

Notice polarity changes at 50° - 60° and 140° - 150° and compare to seismograms in Figure 5.9. Those directions indicate the symmetry axes. In addition, Figure 5.26 shows the hodograms for some of the stations of the wide-azimuth OBN data from Chapter 4 showing that particle motion points to the same directions (50° - 60° and 140° - 150°).
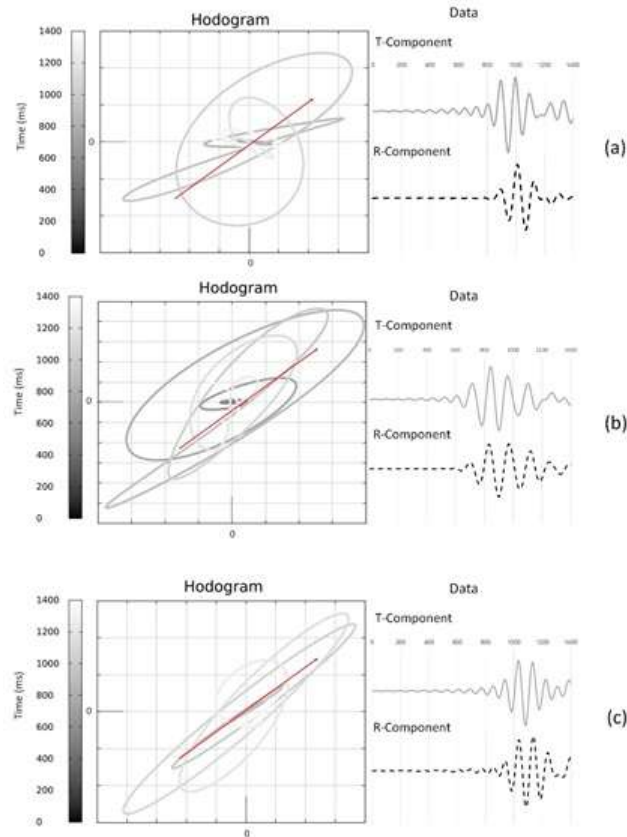
Figure 5.26: Hodograms for three different stations in the wide azimuth data show particle motion. In (a) station 1, in (b) station 20 and in (c) station 80.

In addition to the wide-azimuth surveys presented above, a full-azimuth 2Cx2C experiment was performed over the carbonate to investigate for azimuthal anisotropy hypothesis, as it was suggested in Figure 4.55. The geometry for the full-azimuth 2C x 2C experiment is presented in Figure 5.27 in details. Radial distance between source and receivers is 40.56 mm (centers) and the transducers have diameters of 12.7 mm. The source frequency is 500 kHz and receiver frequency is 1 MHz. Sample rate is 0.02 microsecond (sampling frequency 50 MHz), length of trace is 20 000 samples (400 microsecond), and the thickness of the carbonate layer, with coat of couplant, is 57.4 ± 0.1 mm. A 2C survey was performed with no change in source polarization.
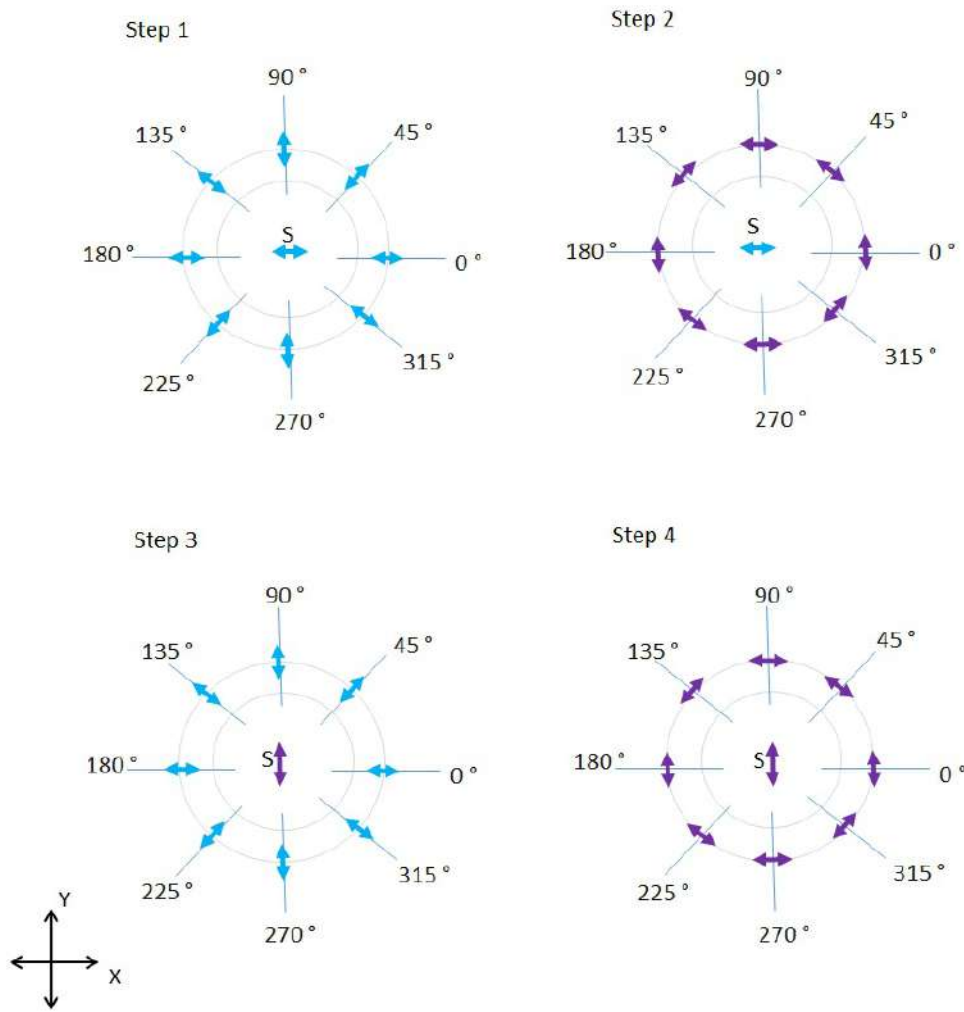
Figure 5.27: Geometry for the full azimuth ultrasonic experiment in details.

On step 1 presented in the Figure 5.27, radial sensors are placed for a horizontal source in the middle. On step 2, transverse sensors are placed around the source. In these first two steps, source is aligned to the x axis. Steps 3 and 4 follow an analogous order, but with the source polarized to y direction.

Displayed in Figure 5.28 there are the absolute energy on the left and the relative energy on the right. In addition, panels (a) and (b) correspond to step 1, panels (c) and (d) to step 2 and so on. They result from the survey shown in Figure 5.27. On y axis there is the amplitude, and on the x axis is the time in milliseconds. Angle sampling is 45°. Greater amplitudes are at different azimuths which are studied as follows.

Figure 5.29 presents rose wind plots from full-azimuthal 2Cx2C experiments. Major energy points to azimuths close, but not exactly, to the survey's coordinate system. Full azimuthal energy recorded from source x polarization is showed in (b) normal and (c) radial receivers. Energy from source y polarization is showed in (d) and (e). RN (b) and (d) point to $\theta = 90°$ and $180°$, approximately, while RR (c) and (e) points to $320°$ - $140°$. This reminds us from symmetries in Figure 5.25, which are in agreement with Figure 5.28 (c) and (e).

The patterns found in this analysis have suggested some sort of symmetry in the data. The patterns seen in Figure 5.29 suggest that axes of anisotropy are transverse, where two sets of vertical fractures cross each other. On the other hand, the visualization of the traces in Figure 5.30 shows evidences of high heterogeneity in the rock, which can cause uncertainties in the analysis.

Concerning to heterogeneity, the wavelet asymmetry might be a result of scattering of shear wave field and near-field heterogeneity together with anisotropy in the rock (CHRISTOPHER *et al.* 2014[102]; ANGERER *et al.*, 2002[103]).

Due to physical imposibilities during experiment, for source polarized in x direction, traces at 180 were not measured. Besides, for source polarized y direction, traces at 270 were not measured too. The missing traces were interpolated from their neighbors.

Pairplots at the azimuth 90° position are shown in the Figure 5.31. Observe that the hodogram in the pairplot 11 versus 22 on the top right the particle motion points to a direction aligned with approximately 135° and 315°. This confirms the azimuths shown in the above analysis.

Since we are working with a real carbonate layer, we know that it was submitted to a diagenetic process and different stress conditions might have happened with the geological time. We can conclude then that the medium is certainly anisotropic, but for some reason it shows a different symmetry from the expected for azimuthal anisotropy, which was, remember, the initial hypothesis.

On Figure 5.29 left side, consider stations at 0° and 90° azimuths (same as
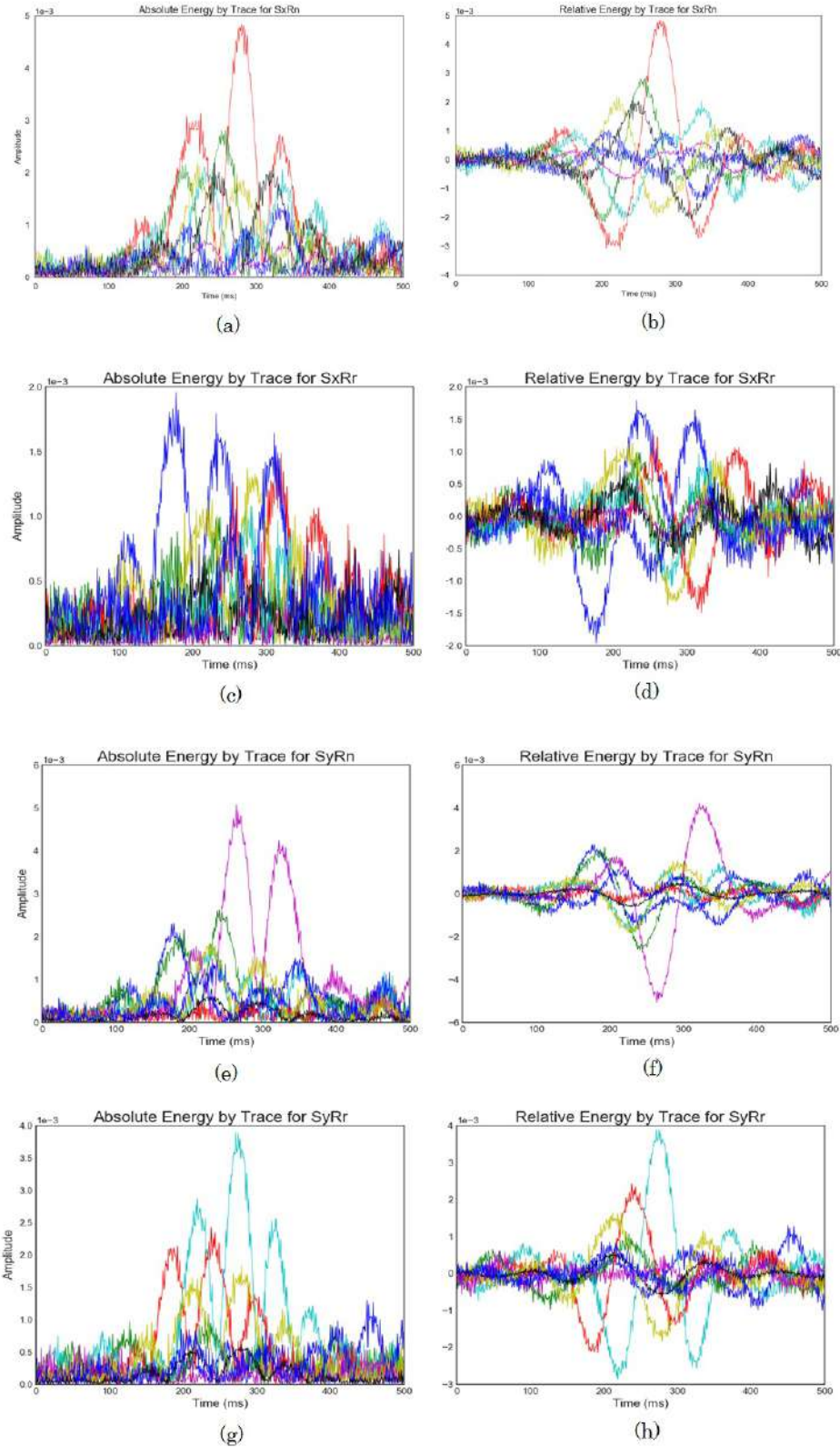
Figure 5.28: Absolute (left) and relative (right) amplitude for pairs source-receiver.

stations 1st and 40th in Figure 4.55) for the following analysis.

If one focuses on the top seismogram at Figure 5.32 he/she will see that shear-
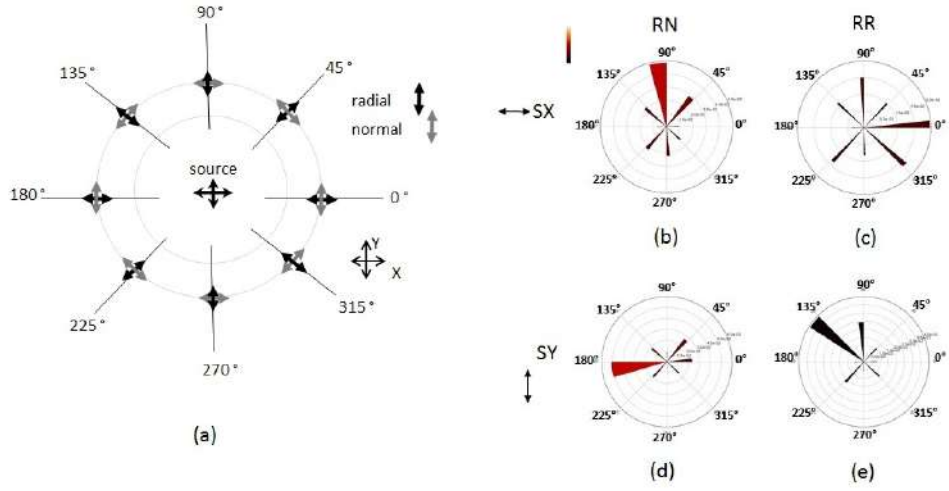
Figure 5.29: Rose wind plots from full-azimuthal 2Cx2C experiment.
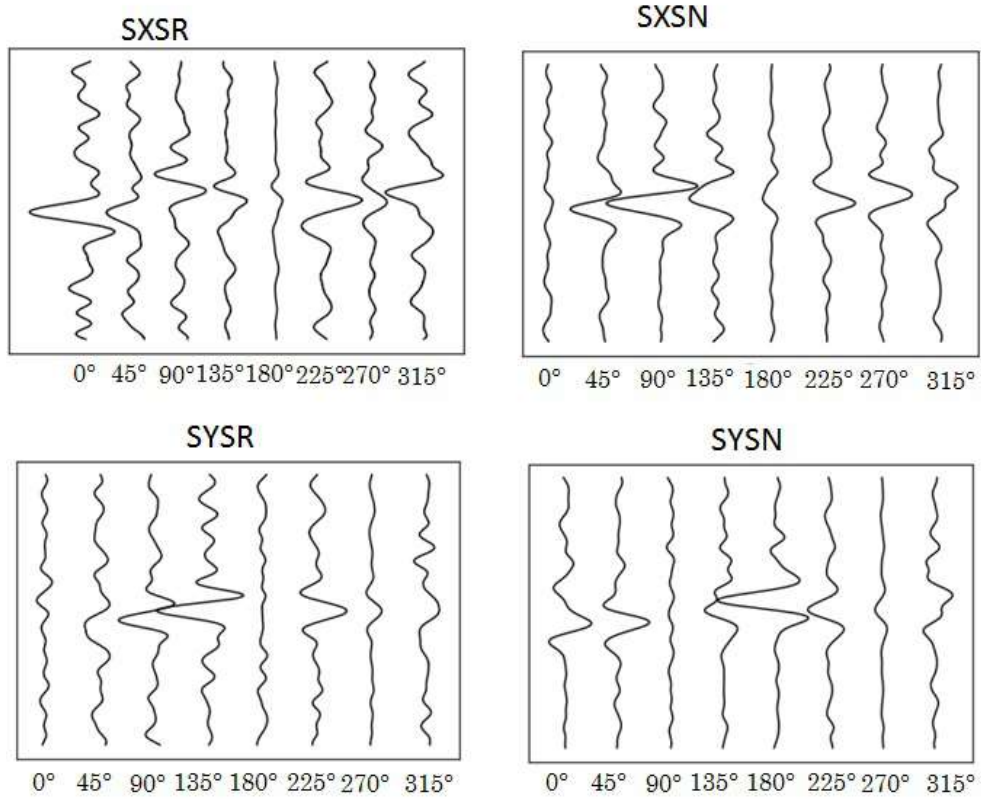
Figure 5.30: Traces from the full-azimuth experiment.

wave energy arrives first at 22 direction for the 0° position and at 11 para the 90° position. Arrival times are about the same for both positions in the geometry. By getting the arrival time in the 0° position we have $t_f = 53.035$ μs for the fast mode and $t_S = 53.357$ μs for the slow mode. Then, $\Delta t = 0.322$ μs.

The amount of anisotropy, if computed by Equation 5.3, is yields $\gamma^{(s)} = 0.006$, or 0.6% of anisotropy. However, this value is very low and might not reflect the real
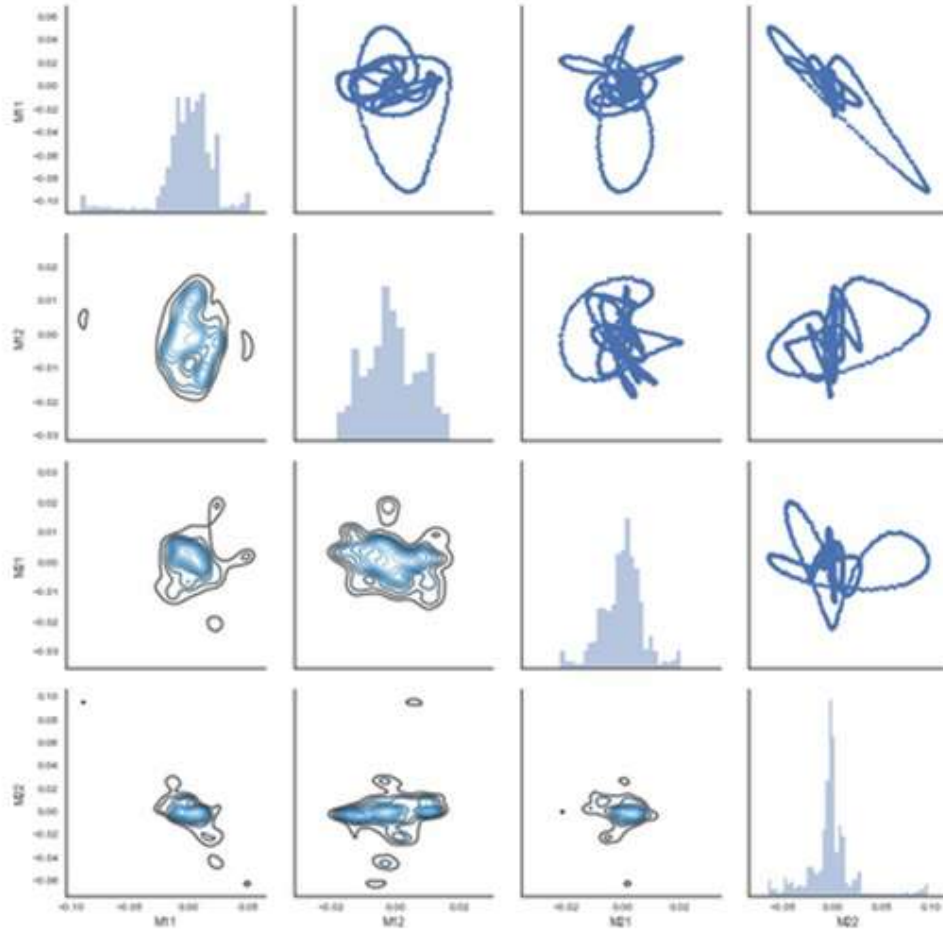
Figure 5.31: Pairplot shows correlations between 11, 22, 12 and 21.

complex stress field in the carbonate. Another possibility that would explain the above results is that the medium has some type of orthogonal symmetry. Therefore, no conclusions about the degree of anisotropy can be drawn based on the assumption of azimuthal anisotropy.

5.5   Conclusions

In this chapter it was proposed the development of an algorithm for azimuthal anisotropy detection, to apply a type of Alford rotation, and anisotropy analysis of seismic surveys. Concerning to the results obtained from the validation cases, the physical phenomena that the code proposed to show are coherent with the modeled data. Therefore, the computational code showed good performance according to the literature. The author wishes to continue working on a graphic user interface of *analize*.
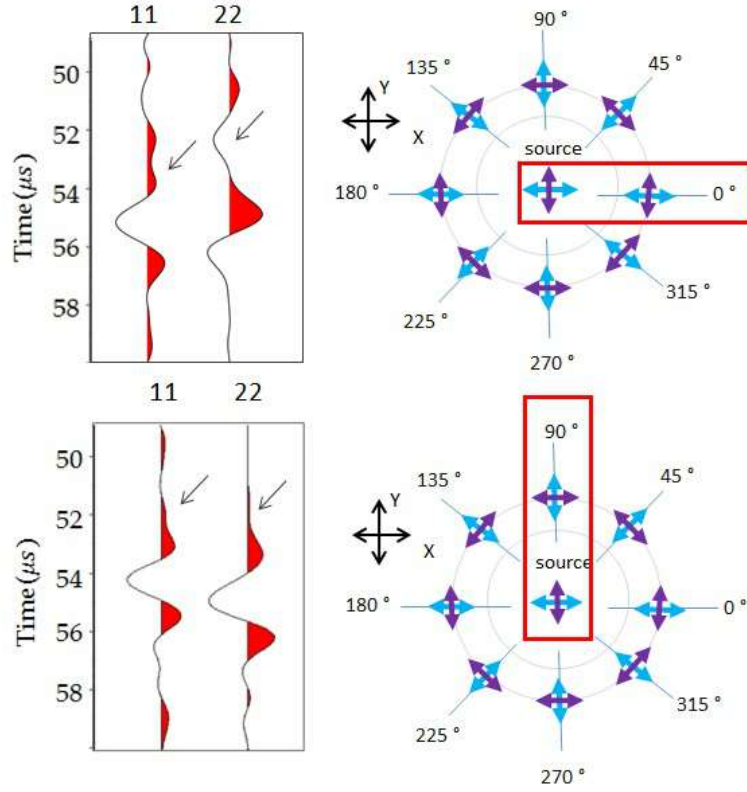
Figure 5.32: 11 and 22 traces at 0° and 90° positions show delay in time.

Hodogram analysis show the particle motion and indicates main direction of energy. Faster S-wave particle motion points to the direction of the sets of fractures. Converted-wave show similar behavior, faster converted-wave points to the direction of fractures.

The amount of anisotropy found by S-wave is $\gamma^{(s)} = 10\%$ of anisotropy, and by C-wave is $\gamma^{(s)} = 6\%$. The value of the amount of anisotropy found by S-wave is 60% greater than for C-wave. That was expected since the equation to compute the degree of anisotropy for S-wave considers the time delay between each other. It is expected that C-wave doesn't show the same amount of anisotropy as S-wave.

Since C-wave is P- to S-wave by nature, the wave become S-wave for the half of the way. Then, about 50% of the delay in time is registered. Also, the computation takes into consideration the arrival time to the S-wave slower to divide the delta t, inserting the effect of P-wave velocity in the computation. The arrival time of a C-wave is lower that the arrival time of a S-wave. Then, the division by a minor number makes the amount of anisotropy greater than 50% of the S-wave anisotropy. The amount of anisotropy computed via C_{ij} coefficients is 0.5% greater that the value coputed for PS-wave which is a very close value.

The modeling for C-wave proved to be powerful in characterizing directions

of sets of fractures in the overburden and also in giving a reliable estimate of anisotropy for the modeled rock. Investigations concerning to the direction of sets of fractures and amount of anisotropy are of great relevance since fractures may become pathways for hydrocarbons or even barriers in reservoir preventing from connections which are great features for production in a reservoir.

Although other methods should be used to confirm the direction of fractures in the overburden, such as borehole data, pure mode seismic S-wave and converted P- to S-wave are able to indicate such direction for each layer in the subsurface.

Wide-azimuth data from the ultrasonic water-bottom experiment showed anisotropy indicators for converted-wave which were then confirmed by the investigation of S-wave splitting with 2C x 2C data, which points to $\approx 50°$ and $140°$ with x. Other analysis also pointed to those directions, but no conclusions could be drawn about specific anisotropy axes since the high degree of heterogeneity might cause uncertainties, such as in the angle for rotation. When computed by the usual equation for SS waves, the amount of anisotropy was 0.06% in the carbonate. If there is azimuthal anisotropy or other type symmetry in the carbonate layer it might be a result of horizontal stresses in the overburden, cracks or porosity like aligned vugs from diagenesis process.

Chapter 6

Final Conclusions

In this work the author proposed the modeling and analysis of seismic data of an anisotropic medium where the anisotropy is caused by vertical fractures. Also studies of the OBN survey were proposed and anisotropy analysis were performed over a carbonate layer. In this chapter all the conclusions are summarized. The author is a physicist who started her Doctoral studies four years before the publication of this thesis. Everything made by the author in this thesis was her first time in life.

To perform the computational modeling and dealing with multicomponent features from anisotropy in seismic, it was required that the author had studied the theory of anisotropy in general, S-wave splitting and fractures. To come to know what such anisotropy causes in the data and then look for that in the synthetics. Also, to build the computational code for anisotropy analysis and alford rotation was a challenge that helped her to become more mature in Geophisics. That was when she felt she had became a Geophysicist.

Chapter 3 proposed a computational modeling of a combination of layers of well known real rock types from literature. The resulting fictitious model was composed of a vertically fractured layer, which anisotropic coefficients were computed through the pseudo-orthorhombic medium approach from the combination of the methodologies of Mah & Schmitt (2003)[6] and Schoenberg & Helbig (1997)[50] and real layers found in the work of Leon Thomsen (1986)[5]. The Reflectivity Method implemented in the program *anisinpausp* was used to model multicomponent data for the model.

It was shown by the synthetic isotropic and anisotropic data that the algorithm is adequate for providing features of P, both S and PS waves. Polarity asymmetry around the source and changes in polarity and phase after the P-wave critical angle

were observed in both models for S-waves.

In addition, S- and C-waves showed birefringence when the survey geophones were not aligned to the medium's main axes of symmetry. At 0° and 90° with fractures there was no conversion from S_V- to S_H. On the other hand, S_f- to S_s- wave energy appeared in the survey as the angle increased with the direction of the vertical sets of fractures (from 0° to 90°). Converted P- to S-waves showed similar features to S-waves.

Hodogram analysis showed particle motion and indicated a main direction of energy. Faster S-wave particle motion pointed to the alignment of the sets of fractures. A similar behavior was showed by C-wave.

In Chapter 5 it was proposed the development of an algorithm for detection of anisotropy caused by vertical fractures. The algorithm provides anisotropy analysis and apply a type of Alford rotation for seismograms. Concerning the results obtained from the validation cases, the physical phenomena that the code proposed to point and analyze are coherent. It has computed exactly the angles that there were in the modeled data. ***analize*** has also detected whether there are sets of vertical fractures or not and performed the rotation of the geophones providing the time shift and the amount of anisotropy.

It was found through the S-wave analysis with the code that $\gamma^{(s)} = 10\%$ is the amount of anisotropy, and through the C-wave analysis $\gamma^{(ps)} = 6\%$. Since C-wave have split and traveled just a half of the way in the anisotropic medium as a S-wave, increasing Δt during a half of the way, it should really have lower value of anisotropy. Actually 60% of the S-wave value seems to be pretty adequate value. The $\gamma^{(ps)}$ differs from $\gamma^{(s)}_{Cij}$ just by 0.5%, resulting in a good estimate for te anisotropy in the layer. Therefore, the computational code showed to be a powerful tool for the anisotropy analysis of vertically fractured media. The author wishes to continue working on the graphical interface of ***analize***.

During the time spent in Houston, she have participated in Geophysical fields which have helped her to know what is it in practice. She have designed the water-bottom experiment using all hr knowledge in seismic acquisition for that. Major dificulties found during the physical modeling were mostly about scaling. When receivers are scaled to real world (1:10,000) they became in the order of 200 meters large. That causes the data closer to receivers to be noise.

Also, she have designed the water-bottom acquisition to emmulate the OBN survey. During the seismic processing she came to know what she was missing or could be made better during the survey. Unfortunately that was too late to redo

the survey, she was in the end of her period in the University of Houston.

Although students use to process data during subjects in class in the Ph.D. course, as I did in Rio de Janeiro with synthetics and in Houston with real data, it is useful to have many experiences in seismic processing to become an Geophysicist expert in it. Then, major dificulties concerning the seismic processing was the lack of experience in seismic processing and the non easy availability of free softwares for multicomponent seismic data, including ocean bottom data. However, the author had the oportunity to learn many special features from water-bottom data and the processing.

On Chapter 4 an ultrasonic physical modeling of Ocean Bottom Nodes was presented. A 2D seismic line was performed, and data was acquired and processed for 161 shots and repeated 80 times with 4C sensors. The model was scaled 1:10,000 in time, space and frequency and a carbonate layer with an ellipsoidal anomaly was imaged in.

A study of reflection and transmission coefficients was performed prior to the experiment in order to verify which model would provide the most suitable amplitude reflection coefficients from the model bottom for P-wave and C-wave. Rock measurements were hence performed in the carbonate limestone layer for assessing density, velocities and other properties for the physical model and for the synthetics.

The computed median connected porosity was 21 % pore space, which sowed that at high frequencies, ultrasonic lab measurements were affected by mechanisms operating at different frequency range and they were not entirely representative of velocities at seismic frequencies. Similar results were found in the literature. The carbonate limestone showed shear modulus changes, from dry to brine saturation, of up to 9%, in accordance with several other laboratory studies.

Though both data, vertical and inline channels, had a complex velocity semblance to pick, the final sections clearly present the main events and the anomaly placed over the right time and depth. Internal and water-bottom multiples were found in both data and attenuated by using Radon parabolic Transform. The final section after the processing was migrated with Phase Shift Post-stack Time Migration for P-wave and Kirchhoff Prestack Time Migration for C-wave.

Although P-wave achieved major maximum fold than C-wave, its spacial sampling was lower, which means C-wave spacial resolution exceeds P-wave for shallow data. Converted-waves from the OBN ultrasonic experiment showed to have enough quality to image the dome structure and they are strong indicators of fractures properties that lead to fluid flow in petroleum reservoirs.

Carbonate rocks are likely to be anisotropic due to the their usual heterogeneity and also to the existence of fractures caused by tectonics or stress following deposition. In the face of this, it should be expected from the rock model to present evidences of anisotropy. In fact the leaking energy found in the crossline channel was not expected to appear in an isotropic medium. In addition, small energy at the crossline channel is normally regarded as a direct indication of azimuthal anisotropy. Further investigations on the carbonate anisotropy were carried on Chapter 5.

Though the amount of multiple reverberations in the seismic data have affected the data quality for the anisotropy investigation, wide azimuth PS-wave survey have presented variation of Δt between fast and slow shear with azimuth. Those are features of vertically fractured anisotropy. Therefore, PS-waves have detected anisotropy with main axes of symmetry pointing to $\approx 50°$ and $140°$. Those indicators were later investigated with full-azimuth data (2C x 2C) in the end of the Chapter 5 and calculations have shown 0.6% of azimuthal anisotropy in the carbonate layer. However, this amount of anisotropy is too low, and should not reflect the real anisotropy of the medium. High heterogeneity or different type of symmetry is likely to be the case, though.

In the final analysis, S-wave and PS converted-wave proved to be effective for overburden fracture direction characterization. It also gave a reliable estimate of anisotropy for the rock. Investigations concerning to the direction of sets of fractures and amount of anisotropy are of great relevance since fractures may become pathways for hydrocarbons or even barriers in reservoir preventing from connections which are great features for production in a reservoir.

Though the analysis presented in this work is focused in vertically fractured media, the methodology is applicable to media in which the anisotropy is caused by an imbalance between horizontal stresses. Although other methods such as borehole data should be used to confirm the direction of fractures, pure mode seismic S-wave and converted P- to S-wave are quite able to do the job. Methodologies like the presented in this work have promising future application for the geological pre-salt regions due to Earth stress, fault structure, and geometrical variations caused by changes in stresses in deep overburden and salt structures.

The author expects that her work can contribute in the direction of helping to pave the way for the widening of the use of azimuthal anisotropy analysis in current Brazilian geophysical practice. Alternative tools and algorithms like the ones presented in this work for studying anisotropy present a very attractive approach to geophysical problems. Other analysis besides the ones presented here could be proposed. Examples of other analysis of orthorhombic anisotropy would be the effect

of that anisotropy over the Thomsen's parameters, P-wave azimuthal analysis, etc. Besides that, the application of this methodology to real data would be a great continuity of this work.

Referências Bibliográficas

[1] "Ocean bottom seismic". http://www.peakseismic.com/content/ocean-bottom-seismic.asp:2017-01-10, 2017.

[2] CHOQUETTE, P. W., PRAY, L. C. "Geologic nomenclature and classification of porosity in sedimentary carbonates." *Bulletin of American Association of Petroleum Geologists*, v. 54, n. 2, pp. 207–250, 1970.

[3] LIU, E., A., M. *Seismic Fracture Characterization: Concepts and Pratical Applications.* The Netherlands, Education Tour Series, EAGE, 2012.

[4] BALE, R., GRATACOS, B., MATTOCKS, B., et al. "Shear wave splitting applications for fracture analysis and improved imaging: some onshore examples." *First Break*, v. 27, pp. 73–83, 2009.

[5] THOMSEN, L. "Weak elastic anisotropy." *Geophysics*, v. 51, pp. 1954–1966, 1986.

[6] MAH, M., SCHMITT, D. R. "Determination of the complete elastic stiffnesses from ultrasonic phase velocity measurements." *Journal of Geophysical Research*, v. 108, n. 1, pp. 1–11, 2016.

[7] GUIMARÃES, M. A., SIMPLICIO, F. "Evolução tecnológica na aquisição sísmica marítima." *International Congress of the Brazilian Geophysical Society*, v. 8, pp. 14, 2003.

[8] GUIMARÃES, M. A. *Aquisicao, processamento e interpretacao de dados geofisicos.* Tese de D.Sc., University of Houston, Houston, Tx., 1998.

[9] BERG, E., VUILLERMOZ, C., EKMANN, G., et al. "Origin and Advances of the Planted 4c Seismic Node Technology." *Society of Exploration Geophysicists*, v. 80, pp. 3728–3733, 2010.

[10] OVERKIL, G. O., NAES, F. "Seismic Node 4C-3D Acquisition System." *Geohorizons*, v. 1, pp. 30–33, 2005.

[11] STEWART, R. R. "Converted-wave seismic exploration: applications." *Geophysics*, v. 68, n. 1, pp. 40–57, 2003.

[12] GAISER, J. E. "Applications for vector coordinate systems of 3D converted-wave data." *The Leading Edge*, v. 18, pp. 1290–1300, 1999.

[13] ALFORD, R. M. "Shear Data in the Presence of Azimuthal Anisotropy: Dilley, Texas", *Society of Exploration Geophysicists, Expanded Abstracts*, v. 56, pp. 476–479, 1986.

[14] GAISER, J. E., VAN DOK, R. R. "Processing And Analysis Of 3-D Ps-Wave Data For Fracture Detection: Green River Basin, Wyoming Case Study." *WesternGeco, Denver, CO*, v. 60, pp. 1–3, 2002.

[15] SCHULTE, S. V., EDELMAN, G. M. "Azimuthal anisotropy proven to be a useful approach for multicomponent shear wave data processing." *Society of Exploration Geophysicists*, v. 58, pp. 1156–1158, 1988.

[16] WINTERSTEIN, D. F. "Velocity anisotropy terminology for geophysicists", *Geophysics*, v. 55, pp. 1070–1088, 1989.

[17] "Petrobras posts new record for pre-salt oil output." `http://agenciabrasil.ebc.com.br/en/economia/noticia/2017-07/petrobras-posts-new-record-pre-salt-oil-output:2017-08-01`, 2017.

[18] NT, S.-R. "Pré-sal Sal: de quanto estamos falando? Uma Análise macroeconômica da produção potencial dos campos do Pré-sal brasileiro." *Subsecretaria de Estudos Econômicos*, v. 2, n. 2, 2010.

[19] "Leilões do pré-sal em outubro atraem 17 grandes petroleiras." `http://www1.folha.uol.com.br/mercado/2017/09/1918436-leiloes-do-pre-sal-em-outubro-atraem-17-grandes-petroleiras.shtml:2017-08-01`, 2017.

[20] ESTRELLA, G. "Pre-salt production development in Brazil." *World PETROLEUM Congress*, v. 20, n. 2, pp. 96–99, 2009.

[21] FRONTIER, T. N. "The New Frontier: Exploring for Oil with Gravity and Magnetics", *Earth Explorer*, v. Fall, 2008., pp. 2, 2008.

[22] SILVA, E. B. S., STEWART, R. R., DYAUR, N., et al. "Ocean Bottom Nodes Ultrasonic Physical Experiment." *Third EAGE/SBGf Workshop 2016*, v. 3, 2016.

[23] THOMSEN, L. *Understanding seismic anisotropy in exploration and exploitation.* Oklahoma, Society of Exploration Geophysicists, 2002.

[24] GUPTA, I. N. "Dilatancy and premonitory variations of P, S travel times." *Soc. Am.*, v. 63, pp. 1157–1161, 1973.

[25] GUPTA, P. R. "Surface waves in micropolar elastic media." *Bull. Acad. Pol. Sci. Ser. Sci. Technol.*, v. 22, pp. 137–146, 1974.

[26] CRAMPIN, S., KING, D. W. "Evidence for anisotropy in the upper mantle beneath Eurasia from generalized higher mode surface waves." *Geophysics*, v. 49, pp. 59–85, 1977.

[27] CRAMPIN, S. "Effective anisotropic elastic constants for wave propagation through cracked solids", *Geophys. J. R. astr. Soc.*, v. 76, pp. 135–145, 1984.

[28] CRAMPIN, S. *A review of wave motion in anisotropic and cracked elastic media.* Austin, Texas, Springer, 1981.

[29] CRAMPIN, S. "Evaluation of anisotropy by shear-wave splitting." *Geophysics*, v. 50, pp. 142–152, 1985.

[30] LYNN, THOMSEN. "Shear-wave exploration along the principal axis." *Society of Exploration Geophysicists, Expanded Abstracts*, v. 56, pp. 474–476, 1986.

[31] WILLIS. "Azimuthal anisotropy: The occurence and effect on shear wave data quality", *Society of Exploration Geophysicists, Expanded Abstracts*, v. 56, pp. 479–481, 1986.

[32] MARTIN, M. A., DAVIS, T. L. "Shear wave birefringence: a new tool for evaluating fractured reservoirs." *The Leading Edge*, v. 6, pp. 534–543, 1987.

[33] TSVANKIN, I., GAISER, J. E., GRECHKA, V., et al. "Seismic anisotropy in exploration and reservoir characterization: An overview." *Geophysics*, v. 75, n. 5, pp. 75A15–75A29, 2010.

[34] VERSFELT, J. W. "South Atlantic Margin rift basin asymmetry and implications for pre-salt exploration." *Society of Petroleum Engineers - International Petroleum Technology Conference*, v. 4, pp. 14, 2009.

[35] PETTER, H. W. "Seismic anisotropy in exploration and reservoir characterization: An overview." *Offshore*, v. 70, n. 7, 2010.

[36] BEARSLEY, C. J., FIDUK, J. C., BIZE, E., et al. "Brazil's pre-salt play." *Brazil's pre-salt play*, v. 22, n. 3, pp. 28–37, 2010.

[37] RIGSBY, T. B. "Method for ocean bottom surveys", *U.S. Patent 5682357 A*, 1997.

[38] MORTON, A., WOJE, G., ROLLET, A., et al. "Evaluation and impact of sparse-grid, wide-azimuth 4C-3D node data from the North Sea." *Society of Exploration Geophysicists, Expanded Abstracts*, v. 73, pp. 826–829, 2003.

[39] JAMES, N. P., KENDALL, A. *Introduction to Carbonate and Evaporite facies Models. 409p.* Canada, Roger G. Walker and Noel P. James, 1992.

[40] RIDING, G., AWRAMICK, S. M. *Microbial Sediments. 331p.* Berlin, Springen, 2000.

[41] LINDT, I. L. "Stylolits in chalk from Leg130, Ontong Java Plateau, In. Berger WH, Kroenke JW, Mayer LA." *Ocean Drilling Program, Scientific Results.*, v. 130, pp. 445–451, 1993.

[42] LUCIA, F. J. *Carbonate Reservoir Characterization.* Austin, Texas, Springer, 2007.

[43] VETRI, L., LOINGER, E., GAISER, J., et al. "3D/4C Emilio: Azimuth processing and anisotropy analysis in a fractured carbonate reservoir." *The Leading Edge*, v. 22, pp. 675–679, 2003.

[44] ENGELDER, T., UZCATEGUI, R. S. "Joint sets that enhance production from Middle and Upp Devonian gas shales of the Appalachian Basin." *APPG Bulletin*, v. 93, n. 857–889, 2009.

[45] ENGELDER, T. "With Marcellus, it's all above the fractures." *APPG Bulletin*, v. 93, pp. 857–889, 2011.

[46] NARR, W., SCHECHTER, W. S., THOMPSON, L. "An amplitude-based multiazimuth approach to mapping fractures using P-wave 3D seismic data." *SPE Publication*, v. 69, pp. 474–476, 2006.

[47] LIN, M., CHEN, S., DING, W., et al. "Effect of Fracture Geometry on Well Production in Hydraulic-Fractured Tight Oil Reservoirs." *Society of Petroleum Engineers - International Petroleum Technology Conference*, v. 54, n. 3, 2015.

[48] PAŠIĆ, B., GAURINA-MEDIMUREC, N., D., M. "Wellbore instability: causes and consequences." *Rudarsko-geološko-naftni zbornik*, v. 19, pp. 87–98, 2007.

[49] NELSON, R. *Geological Analysis of Naturally Reservoirs. 2nd Edition.* Houston, Gulf Publishing House, 2000.

[50] SCHOENBERG, M., HELBIG, K. "Orthorhombic media: Modeling elastic wave behavior in a vertically fractured earth." *Geophysics*, v. 62, n. 6, pp. 1954–1974, 1997.

[51] SCHOENBERG, M., DOUMA, J. "Elastic wave propagation in media with parallel fractures and aligned cracks." *Geophysics*, v. 36, pp. 571–589, 1988.

[52] ZHANG, X., SANDERSON, D. "Effects of stress on the two-dimensional permeability tensor of natural fracture networks." *Geophysics*, v. 125, n. 24, pp. 125–912, 1996.

[53] BAHADORI, A. *Fluid Phase Behavior for Conventional and Unconventional Oil and Gas Reservoirs*, v. 1. USA, Elsevier, 2016.

[54] RATNER, M., TIEMANN, M. "An overview of unconventional oil and natural gas: Resources and Federal Actions." *Congressional Research Service, USA.*, v. 22, April 2015, pp. 30, 2014.

[55] HEFFER, K., FOX, R., MCGILL, C., et al. "Novel techniques show links between reservoir flow directionality, Earth stress, fault structure, and geometrical changes in mature water floods." *Society of Petroleum Engineers Journal*, v. 2, pp. 91–98, 1995.

[56] HEFFERR. "Earth stress orientation on reservoir flow - numerical modeling used to reproduce field data." *Geological Society*, v. 84, pp. 81–88, 1993.

[57] BATES, C. R., LYNN, H. B., SIMON, M. "The Study of a Naturally Fractured Gas Reservoir Using Seismic Techniques." *AAPG Bulletin*, v. 83, n. 9, pp. 1392–1407, 1999.

[58] YILMAZ, O. Z. *Seismic Data Analysis. V 1 and 2.* Tulsa, Society of Exploration Geophysicists, 2001.

[59] STEWART, R. R., GAISER, J. E., BROWN, R. J., et al. "Converted-wave seismic exploration: Methods." *Geophysics*, v. 67, n. 5, pp. 1348–1363, 2002.

[60] STEWART, R. R., GAISER, J. E., BROWN, R. J., et al. "Converted-wave seismic exploration: a tutorial." *Converted-wave seismic exploration: a tutorialCREWES Research Report*, v. 11, 1999.

[61] TSVANKIN, I., GRECHKA, V. *Seismology of azimuthally anisotropic media and seismic fracture characterization.* Oklahoma, Society of Exploration Geophysicists, 2011.

[62] GAISER, J. E.; VAN DOK, R. R. "Processing And Analysis Of 3-D Ps-Wave Data For Fracture Detection: Green River Basin, Wyoming Case Study." *WesternGeco, Denver, CO*, v. 60, pp. 10, 2016.

[63] GUEVARA, S. E., STEWART, R. R. "Source-geophone azimuth from 3-C seismic polarization." *CREWES Research Report*, v. 12, pp. 10, 2000.

[64] INKS, T. L., ENGELDER, T., JENNER, E., et al. "Marcellus fracture characterization using P-wave azimuthal velocity attributes: Comparison with production and outcrop data", *Interpretation*, v. 3, n. 3, pp. SU1–SU15, 2014.

[65] DUEY, R. "Nodes are finally making their mark." *E&P, ed. Hart Energy*, 2007.

[66] CORRIGAN, D. "The Algorithm for Seismoc Wave Modeling via the Reflectivity Method." *The Leading Edge*, v. 25, pp. 1337, 2006.

[67] TSVANKIN, I. "Reflection moveout and parameter estimation for horizontal transverse isotropy." *Geophysics*, v. 62, pp. 614–629, 1997.

[68] THOMSEN, L. "Vector recomposition of seismic 3-D converted-wave data." *U.S. Patent US6292754 B1*, p. 10, 2001.

[69] GAISER, J. E.; VAN DOK, R. R. "3-D converted shear wave rotation with layer stripping." *U.S. Patent 5 610 875*, 1997.

[70] FUCHS, MÜLLER. "Reflection moveout and parameter estimation for horizontal transverse isotropy." *Geophysics*, v. 62, pp. 614–629, 1985.

[71] KENNETT, B. L. N. *Seismic Wave Propagation in Stratified Media.* Australia, University Printing Services, ANU, 1975.

[72] ALISON, J. R., BUSH, M. D., CAIN, G., et al. "anisynpausp: anisotropic synthetic generation." *OGS Research and Development*, 2015.

[73] BACKUS, G. E. "Long-wave elastic anisotropy produced by horizontal layering." v. 67, pp. 4427–4440, 1962.

[74] CARRION, P., COSTA, J., PINHEIRO, F., et al. "Cross-borehole tomography in anisotropic media." *Geophysics*, v. 57, n. 9, pp. 1194–1198, 1992.

[75] FUCHS, K.; MÜLLER, G. "Computation of synthetic seismograms with the reflectivity method and comparison with observations." *Geophys. J. R. Astron. Soc.*, v. 23, pp. 417–433, 1971.

[76] BIOT, M. A. "Theory of Propagation of Elastic Waves in a Fluid-Saturated Porous Solid. I. Low-Frequency Range." *Journal of the Acoustical Society of America*, v. 28, n. 2, pp. 168–178, 1956.

[77] BIOT. "Theory of Propagation of Elastic Waves in a Fluid-Saturated Porous Solid. II. Higher Frequency Range." *Journal of the Acoustical Society of America*, v. 28, n. 2, pp. 179–191, 1956.

[78] FABRICIUS, I. L., GOMMESEN, L., KROGSBOLL, A., et al. "Chalk porosity and sonic velocity versus burial depth: Influence of fluid pressure, hydrocarbons, and mineralogy." *AAPG Bulletin*, v. 92, pp. 201–203, 1985.

[79] JOHNSON, D. L. "Recent developments in the acoustic properties of porous media." *Frontiers in Physical Acoustics XCIII*, pp. 255–290, 1986.

[80] GASSMANN, F. "Elastic waves through a packing of spheres." *Geophysics*, v. 16, pp. 673, 1951.

[81] ASSEFA, S., MCCANN, C., SOTHCOTT, J. "Velocities of compressional and shear waves in limestones." *Geophysical Prospecting*, v. 51, pp. 11–13, 2003.

[82] BAECHELE, G. T., WEGER, R. J., EBERLI, G. P., et al. "Changes of shear moduli in carbonate rocks: Implications for Gassmann applicability." *The Leading Edge*, v. 24, pp. 507–510, 2005.

[83] SHARMA, R. M., PRASAD, G. C., KATIYAR, et al. "On the applicability of Gassmann model in carbonates." *Society of Petroleum Geophysicists Conference*, v. 6, pp. 1289–1296, 2006.

[84] ADAM, L., BATZLE, M., BREVIK, I. "Gassmann's fluid substitution and shear modulus variability in carbonates at laboratory seismic and ultrasonic frequencies." *Geophysics*, v. 71, pp. 173–183, 2006.

[85] AKI, K., RICHARDS, P. *Quantitative Seismology.* USA, Freeman and Sons, 1980.

[86] BORTFELD, R. "Approximations to the reflection and transmission coefficients of plane longitudinal and transverse waves." *Geophys. Prosp.*, v. 9, pp. 485–502, 1961.

[87] CHUNG, CORRIGAN, D. "x." *x.*, v. x, pp. x, 1985.

[88] TESSMER, G., BEHLE, A. "Common reflection point data stacking technique for converted waves." *Geophys. Prosp.*, v. 36, pp. 671–688, 1988.

[89] GAISER, J. E. *Application and interpretation of converted-waves*, v. 85. New Orleans, Society of Exploration Geophysicists: Continuing Education Course, 2015.

[90] BERKHOUT, VERSCHUUR. "Removal of internal multiples with the common focus-point CFP approach: Part 1– Explanation of the theory." *Geophysics*, v. 70, n. 3, pp. V45–V60, 2005.

[91] MASON, M. V. *Multicomponent seismic imaging of sand reservoirs: Middle Magdalena Valley, Colombia.* Tese de M.Sc., University of Houston, Houston, Tx., 2013.

[92] GUIMARÃES, M. G., CRAWFORD, P., SUKUP, D., et al. "Controle de qualidade e processamento de dados sismicos obn multi-componentes." *Sociedade Brasileira de Geofísica*, p. 9, 2017.

[93] NEIDELL, N. "Modern Methods of Seismic Data Processing." *Geoquest International*, 1980.

[94] SHERIFF, R., E. *Encyclopedic Dictionary of Exploration Geophysics.* Tulsa, OK, USA, Society of Exploration Geophysicists, 1984.

[95] STEIN, S., WYSESSION, M. *An introduction to seismology, earthquakes, and Earth structure.* USA, Blackwell Publishing, 2003.

[96] BANCROFT, J. C., MARGRAVE, G., GEIGER, H. "A kinematic comparisons of conventional processing, DMO-PSI, and equivalent offset migration (EOM)." *Society of Exploration Geophysicists, Expanded Abstracts*, v. 67, pp. 1575–1578, 1997.

[97] MEIER, M. A., LEE, P. J. "Converted-wave resolution." *Geophysics*, v. 74, n. 2, pp. 10, 2009.

[98] HARRISON, M. *Processing of P-SV surface-seismic data: Anisotropy analysis, dip moveout, and migration.* Tese de D.Sc., The University of Calgary, Houston, Tx., 1992.

[99] LIU, E., HUDSON, J. A., CRAMPIN, S., et al. "Seismic properties of a general fracture." *Mechanics of Joined and Faulted Rock*, v. 64, pp. 659, 2000.

[100] DEFFENBAUGH, M., SHATILO, A., SCHNEIDER, B., et al. "Resolution of converted waves in attenuating media." *Society of Exploration Geophysicists, Expanded Abstracts*, v. 70, pp. 8, 2000.

[101] "Bivariate normal density". `http://math.tntech.edu/ISR/Introduction_to_Probability/Joint_Distributions/thispage/newnode6.html`, `GeneratedbyMATHGO:2006-01-10`, 2006.

[102] CHRISTOPHER, R., SHERMAN, S., GAISER, J., et al. "The effects of near-source heterogeneity on shear-wave evolution", *Geophysics*, v. 79, pp. T233–T241, 2014.

[103] ANGERER, E., CRAMPIN, S., LI, X. Y., et al. "Processing, modelling, and predicting timelapse effects of overpressured fluid-injection in a fractured reservoir." *Geophysical Journal International*, v. 49, pp. 267–280, 2002.

Appendix A

Alford Type Rotation: an Overview

Alford (1986) has an excellent article where he states the Alford Rotation showed below. 1-D elastic wave propagation along z axis, perpendicular to the unique axis of an azimuthally anisotropic medim can be written as:

$$\underbrace{\begin{bmatrix} e_{11} & 0 \\ 0 & e_{22} \end{bmatrix}}_{E} \underbrace{\begin{bmatrix} u_{11} & 0 \\ 0 & u_{22} \end{bmatrix}}_{U} = \underbrace{\begin{bmatrix} \delta(z)g(t) & 0 \\ 0 & \delta(z)g(t) \end{bmatrix}}_{S} \underbrace{\begin{bmatrix} 1 & 0 \\ 0 & 1 \end{bmatrix}}_{I} \tag{A.1}$$

Where Dirac function (δ) specifies spacial locations of sources, and time variations of the source is indicated by g(t). The source direction matrix defines a set of two orthogonal sources aligned along the natural coordinate axes for the azimuthally anisotropic medium.

To simplify, Equation A.1 is written as Equation A.2

$$EU = SI \tag{A.2}$$

where E contains the equation of motion, U contains fundamental solutions, S contains source time and space variations and I is the identity.

During the exploration program a company takes several 2D lines largely spaced for getting previous information from the subsurface. Great quality surveys are usually 3D geometry, several 2D lines shortly spaced over the most probable targets found previously. Source polarizations in 3D surveys are commonly lined up with either the natural coordinate system nor the acquisition system (receivers). In case

sources are oriented in the acquisition system, they are expressed in the coordinates of natural system as shown in Equation A.3

$$R(\theta) = \begin{bmatrix} \cos(\theta) & \sin(\theta) \\ -\sin(\theta) & \cos(\theta) \end{bmatrix} \tag{A.3}$$

The solution for the two sources is obtained by right multiplying Equation A.3 or **??** by R(θ), resulting in Equation A.4.

$$EUR(\theta) = SIR(\theta) \tag{A.4}$$

The expression for solution in terms of acquisition coordinates corresponding to the clockwise rotation of the natural coordinates through an angle of θ is Equation A.5

$$ER(\theta)R^T(\theta)UR(\theta) = SR(\theta) \tag{A.5}$$

where a representation for field data expressed in the simple natural solutions is showed in Equation A.6, and its expanded format on Equation A.7

$$V(\theta) = R^T(\theta)UR(\theta) \tag{A.6}$$

$$V = \begin{bmatrix} \cos^2(\theta)u_{11} + \sin^2(\theta)u_{22} & 0.5(u_{11} - u_{22})\sin^2(2\theta) \\ 0.5(u_{11} - u_{22})\sin^2(2\theta) & \sin^2(\theta)u_{11} + \cos^2(\theta)u_{22} \end{bmatrix} \tag{A.7}$$

Field data is

$$U = R(\theta)V(\theta)R^T(\theta) \tag{A.8}$$

Simpler solution for natural system in terms of solutions in the acquisition system:

$$U = \begin{bmatrix} (\cos^2(\theta)\nu_{11} + \sin^2(\theta)\nu_{22} + 0.5\sin(2\theta)(\nu_{21} + \nu_{12})) & (\cos^2(\theta)\nu_{12} - \sin^2(\theta)\nu_{21} + 0.5\sin(2\theta)(\nu_{22} - \nu_{11})) \\ (\cos^2(\theta)\nu_{21} - \sin^2(\theta)\nu_{12} + 0.5\sin(2\theta)(\nu_{22} - \nu_{11})) & (\cos^2(\theta)\nu_{22} + \sin^2(\theta)\nu_{11} - 0.5\sin(2\theta)(\nu_{21} - \nu_{12})) \end{bmatrix} \tag{A.9}$$

Equations A.8 and A.9 transform field data into the simpler natural solution given by θ.

Then the acquisition coordinate system (and sources, if they were not lined up with acquisition system) is rotated onto the natural symmetry axes in the medium. Energy concentrates at inline channels and offline channels should be zeroed considering the cases where the anisotropy is azimuthal type and there are no other effects such as heterogeneity in the medium for the frequency-wavelength content in the survey. As a result, difference in arrival time, velocities and amount of anisotropy in S-wave data is computed (THOMSEN, 2001[68]; ALFORD, 1986[13]).

Appendix B

Rock Properties Graphs

Rock properties have shown compressional velocities decreasing with water saturation, though density increases more than 10 % as we can see in Figure B.1 on the top. That might be explained by several factors as the interactions between solid and fluid-air in the ultrasonic frequency range. Nevertheless, there are other factors acting over the velocities, as we can see in Figure B.1 the middle graph,μ decreasing 7.43 %with saturation and the bottom graph, K increasing 2.88 %.

The increasing of density in the denominator combined with the decreasing in μ in the dividend is greater than the increasing in K in the dividend. That produces the decreasing in P-wave velocity. Similar analysis can be made for S-wave velocity decreasing, where the increasing in density combines with the decreasing in μ to produce the effect.
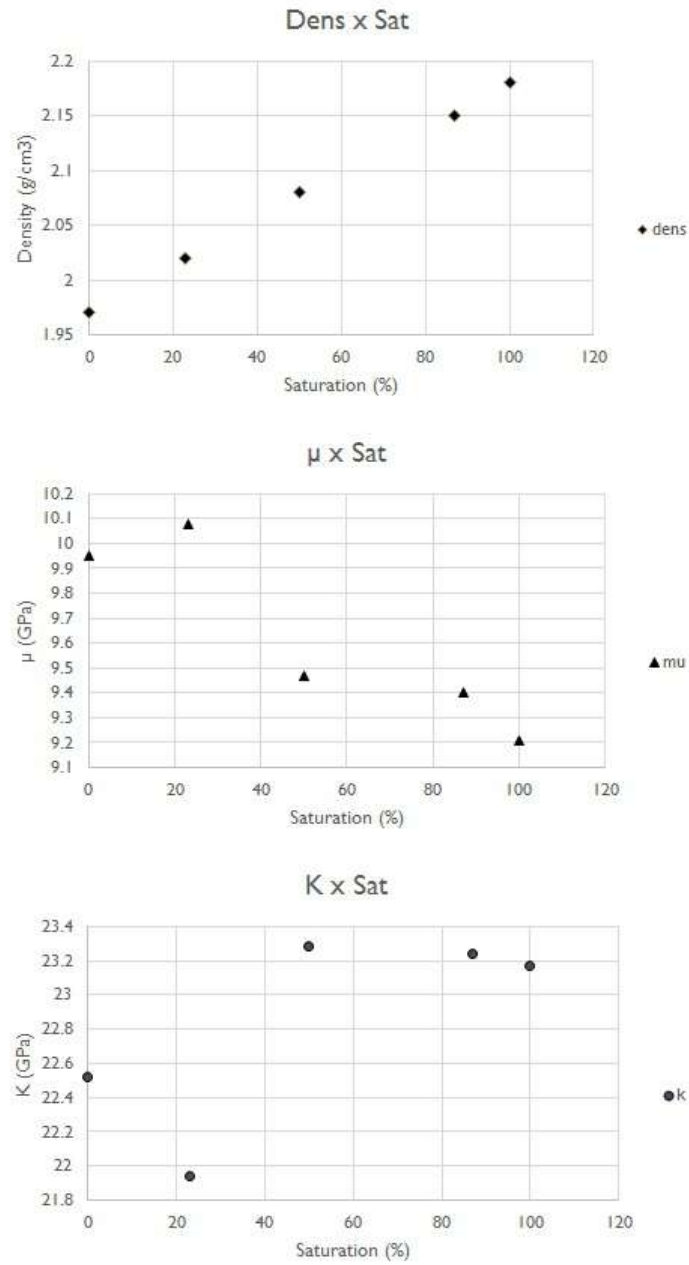
Figure B.1: Rock properties versus saturation. On the top: density; on the middle: shear modulus; and on the bottom: bulk modulus.